Adsorbate-induced stiffening, quantum thermopower and photoresponse in two-dimensional materials

by Simon A. Svatek, MPhil, BSc

Supervised by Nicolas Agraït de la Puente

Doctoral thesis submitted to Universidad Autónoma de Madrid

Madrid, September 2017

Rigidez debida a adsorbatos, potencia termoeléctrica cuántica y fotorrespuesta en materiales dos-dimensionales

Memoria presentada por Simon A. Svatek
para obtar al grado de Doctor en Ciencias Físicas por la
Universidad Autónoma de Madrid

Dirigida por Nicolas Agraït de la Puente

Departamento de Física de la Materia Condensada
Madrid, Septiembre 2017

Thesis committee

1) Herre van der Zant, Delft University of Technology

2) Peter Beton, University of Nottingham

3) Andres Castellanos-Gomez, Consejo Superior de Investigationes Científicas (CSIC)

4) Julio Gómez Herrero, Universidad Autónoma de Madrid

5) Marisol Martin-Gonzalez , Consejo Superior de Investigationes Científicas (CSIC)

This work has been supported by the European Commission through EC FP7 ITN "MOLESCO" Project No. 606728.

Acknowledgements

First and foremost, I would like to thank my supervisor Nicolás Agraït for the opportunity to be part of his research group and MOLESCO. I have learned a lot under his supervision and appreciate that he had an open ear for inquiries of all sorts at all times.

I would also thank my former supervisor Peter Beton, who formally advised me from 2011 to 2014, for his wise counsel and direction.

Another great impact on the contents of this thesis has been made by Elisa Antolín and by Andrés Castellanos through their scientific advice and mentoring and I hereby express my gratitude.

This thesis would not have been written without funding by the European Commission through the Marie Curie Initial Training Network MOLESCO. The European Commission represents the people of Europe, who have somehow given me the opportunity to work full-time on a research project to become part of "a pool of young researchers capable of achieving breakthroughs aimed at realising the immense potential of molecular electronics" (from the MOLESCO grant proposal). I am grateful for this and promise that I keep doing my best to fulfil this expectation.

Contents

1 Introduction and thesis overview

The feature size in semiconductor electronics has reduced over the last decades, thereby decreasing production costs and power consumption. If one dimension of a material is reduced the foreseeable limit is represented by a two-dimensional (2D) material, that is a crystal made of a single layer of atoms. The research field of 2D materials has emerged since the isolation of a graphene, a single layer of carbon atoms, from bulk graphite in 2004. Meanwhile, single layers of a variety of materials have been studied, thereby expanding the catalogue of 2D materials, which now includes the quasi-metal graphene, semiconductors (e.g. MoS_2, InSe), and insulators (e.g. BN). The possibility to incorporate these materials into functional devices offer a new platform for the study of condensed matter phenomena and for the development of novel technologies. The content of this thesis is concerned with the characterisation of these materials in conditions relevant for applications, i. e. in the presence of adsorbates and solvents, a temperature gradient, and under illumination.

In chapter 2 an overview of 2D materials is given. This includes a summary of their properties and a discussion of the possibility to combine these materials into stacked structures. This chapter also includes a description of the physical phenomena which are relevant to the experiments, namely molecular self-assembly on surfaces, the theoretical model for photovoltaic semiconductor devices, and the thermoelectric effect.

Chapter 3 provides an overview of the experimental techniques. This includes a description of the basic principles of scanning probe microscopy and the experimental setups. In particular, a conductive atomic force microscope has been developed which allows the application of a thermal gradient between the sample and the tip. It allows high-accuracy measurements of voltages with errors in the μV range. Further, a short summary of the microfabrication techniques to form 2D material devices is given.

In chapter 4, a morphological study of graphene in the presence of adsorbates and solvents is presented. Self-assembled monolayers of alkanes, tetratetracontane, were formed on graphene and imaged by scanning tunnelling microscopy in a liquid, tetradecane, whereby the graphene was supported by either a stiff or a soft substrate. The soft support was prepared by transferring graphene onto mica which involves

the immersion of the sample into water. The hydrophilicity of mica causes water to be trapped at the graphene/mica interface causing the graphene to be responsive to molecular adsorption. We observe that the adsorption of alkanes induces curvature and anisotropic stiffness in the graphene with a symmetry axis along the alkanes. These effects are not observed when the graphene is supported by a stiff support, i.e. BN, in which case the molecular adsorption is reminiscent to the adsorption on graphite. The findings show that molecular adsorption can influence the mechanical properties of graphene and, thus, is relevant to applications in electronic materials, membrane technologies, and micromechanical systems.

In chapter 5 the thermoelectrical properties of MoS_2 in the cross-plane direction are explored. The thickness of thin layers of MoS_2 is between ~1 nm for a monolayer and ~4 nm for six-layer MoS_2. Hence, the observed thermoelectric effect is the quantum-equivalent of the classical property of a material to generate a voltage from a thermal gradient. It is quantified by the quantum thermopower which has, before this work, only been directly measured in single molecule junctions, which have values up to 40 μV/K and atomic contacts with values up to 5 μV/K. In this study quantum thermopower values of up to 330 μV/K in few-layer crystals have been found. The findings suggest that 2D materials are promising for thermoelectrical applications and probing the cross-plane direction could provide a novel platform for the study of quantum thermoelectric effects.

2D materials can be assembled into vertical stacks in a predefined, chosen sequence. The properties of such heterostructures differ from the properties of their isolated constituents. Each new sequence represents therefore a novel artificial material. The small effort to form such materials and the unusual properties and new phenomena which arise in such structures have sparked a great amount of scientific interest. In this research field, there are many open questions, one of which has arisen from the finding that the Shockley diode model, which describes the charge carrier dynamics of a classical p-n junction, does not hold for p-n junctions made of monolayers. Few-layer material is important for applications and the question arises whether the Shockley diode model holds in an intermediate thickness-regime between monolayer and bulk. In chapter 6 the carrier dynamics in few-layer p-n junctions made of few-layer MoS_2 with a total thickness of ~10 nm is investigated, showing good agreement with the Shockley diode model. Furthermore, the low thickness enables to influence the charge carrier density in the material by an electrostatic field which can be generated by applying a voltage to a gate-electrode. It is found that the characteristic diode parameters show a strong gate-dependence,

which is discussed comprehensively. The findings demonstrate potential for MoS_2 based solar cells and lays groundwork for gate-tunability of efficiency and photovoltaic response in ultrathin p-n junctions.

Another type of 2D material heterostructure, in which a 2D material is sandwiched between graphene electrodes, is discussed in chapter 7. The motivation to form such sandwich-devices is to increase the charge carrier extraction efficiency by exploiting the low resistance of graphene in comparison with 2D semiconductors. The development of a fabrication strategy to form graphene/InSe/graphene vertical stacks from centimetre-scale graphene and exfoliated InSe flakes, providing a route to large area scalability, is discussed in chapter 6. The optoelectronic properties of these stacks have been measured and we find that, due to a large extraction efficiency of photogenerated charge carriers, we have fabricated one of the most photosensitive 2D material photodetectors reported to date.

1.B Resumen

This chapter is a translation of chapter 1 into Spanish, a requirement for PhD theses by UAM.

El tamaño característico de los dispositivos electrónicos semiconductores ha disminuido drásticamente en las últimas décadas, y con su tamaño se han reducido también su coste de producción y la potencia que consumen. Si la reducción de tamaño se da en una dimensión, el límite último que podemos prever para estos dispositivos lo constituye el uso de un material dos-dimensional (2D), esto es, un cristal compuesto por una monocapa atómica. La investigación de los materiales 2D surgió en 2004 cuando se consiguió extraer de un cristal de grafito una monocapa de átomos de carbono, lo que se conoce como grafeno. Desde entonces se han estudiado monocapas de una variedad de materiales, que incluyen diferentes semiconductores, como el MoS2 o el InSe, aislantes, como el BN, y el mismo grafeno, que se comporta como un cuasi-metal. La posibilidad de incorporar estos materiales en dispositivos funcionales ofrece una nueva plataforma para el estudio de fenómenos de la física de la materia condensada y para el desarrollo de nuevas tecnologías. Esta tesis doctoral trata la caracterización de este tipo de materiales en ciertas condiciones relevantes para su aplicación, esto es, en presencia de adsorbentes y disolventes, cuando se someten a gradientes de temperatura y bajo iluminación.

El Capítulo 2 trata los antecedentes de este trabajo. En él se presentan los materiales 2D junto con un resumen de sus propiedades y una discusión sobre la posibilidad de combinar estos materiales en estructuras apiladas. También se describen algunos fenómenos físicos que son relevantes para los experimentos que presentamos más adelante: el auto-ensamblado de moléculas sobre una superficie, el modelo teórico de un dispositivo semiconductor fotovoltaico, y el efecto termoeléctrico.

En el Capítulo 3 se detallan las técnicas experimentales empleadas en esta tesis. En primer lugar se presentan los principios de funcionamiento de la microscopía de fuerza atómica y la microscopía de efecto túnel. En particular para este trabajo se ha desarrollado un microscopio de fuerza atómica conductivo que admite la aplicación de un gradiente térmico entre la muestra y la punta. Este equipo permite obtener medidas de tensión de gran exactitud con errores en la escala de microvoltios. Además en este capítulo se describen las técnicas de microfabricación utilizadas para producir dispositivos constituidos de materiales 2D.

En el Capítulo 4 se presenta un estudio morfológico del grafeno en presencia de adsorbatos y disolventes. Para realizar este estudio se han producido monocapas autoensambladas de alcanos (tetra-tetra-contano) sobre grafeno y se han caracterizado por microscopía de efecto túnel en ambiente líquido (tetra-decano). El grafeno se encuentra a su vez sobre un sustrato, generando una superficie soporte para las moléculas que puede ser rígida o blanda. Para producir estas superficies soporte se ha transferido el grafeno a un sustrato de BN o de mica siguiendo un proceso que requiere la inmersión de la muestra en agua. En el caso del BN se forma una superficie rígida y la adsorción molecular se produce con una morfología similar a la de la adsorción sobre grafito. Sin embargo la hidrofilia de la mica hace que quede agua atrapada en la interfaz grafito/mica durante la transferencia, por lo que el grafeno se muestra blando y sensible a la adsorción molecular. Observamos que la adsorción de los alcanos en este caso induce curvatura y rigidez anisotrópicas en el grafeno con un eje de simetría en la dirección longitudinal de los alcanos. Estos resultados demuestran que la adsorción molecular puede modificar las propiedades mecánicas del grafeno cuando éste tiene un soporte blando y por lo tanto tiene aplicación en el desarrollo de materiales electrónicos, tecnologías de membranas y sistemas micromecánicos.

En el Capítulo 5 se exploran las propiedades termoeléctricas del MoS_2 en la dirección transversal a su estructura laminar. Se han utilizado cristales delgados de MoS_2 con espesores entre ~ 1 nm (una monocapa) y ~ 4 nm (seis capas). Dado que la carga eléctrica tiene que recorrer una distancia nanométrica cuando atraviesa el cristal transversalmente, observamos un efecto termoeléctrico cuántico, que es el equivalente cuántico de la propiedad clásica por la cual en un material se genera un voltaje a partir de un gradiente térmico. Este efecto se cuantifica a través de la termopotencia cuántica, la cual antes de este trabajo solo se había podido medir directamente en uniones unimoleculares, que presentan valores de hasta 40 $\mu V/K$, y cadenas atómicas, con valores de hasta 10 $\mu V/K$. En este estudio se han obtenido valores de hasta 330 $\mu V/K$ en cristales de MoS_2 de unas pocas capas atómicas. Este resultado sugiere que se pueden encontrar termopotencias cuánticas elevadas en éste y otros materiales 2D y que testar la dirección transversal introduce una plataforma nueva y prometedora para el estudio de efectos termoeléctricos cuánticos.

Los materiales 2D pueden ser ensamblados en apilamientos verticales en un orden definido. Las propiedades de estas heterouniones difieren de las que tienen los constituyentes cuando se encuentran aislados. Por lo tanto, cada nueva secuencia representa un nuevo material artificial. La relativa facilidad con que se pueden formar estas heterouniones y las propiedades inusuales y nuevos fenómenos que aparecen en ellas han provocado un gran interés científico en años recientes. En este campo emergente hay numerosas cuestiones no resueltas. Una de ellas ha surgido al descubrir que el modelo teórico de Shockley, que permite describir el comportamiento del diodo clásico, no es aplicable a uniones p-n hechas de monocapas atómicas. Los cristales multicapa, que contienen unas pocas capas atómicas, son importantes para la fabricación de dispositivos, y por lo tanto, surge la cuestión de si el modelo de Shockley es aplicable en el régimen intermedio de espesor de los cristales multicapa. En el Capítulo 6 se investiga la dinámica de portadores en uniones p-n de multicapas de MoS2 con un espesor total de $\sim$ 10 nm, mostrando una concordancia excelente con el modelo de Shockley. Además, el reducido espesor del dispositivo permite modificar la densidad de carga en el material a través de un campo electrostático que puede ser generado aplicando un voltaje sobre un electrodo puerta. Se observa que los parámetros característicos del diodo muestran una fuerte dependencia con la tensión de puerta, la cual se discute extensivamente en el texto. Los resultados indican que los cristales 2D de MoS2 tienen potencial para la fabricación de células solares y plantean la posibilidad de ajustar la eficiencia y la respuesta fotovoltaica a través la tensión de puerta en uniones p-n ultrafinas.

En el Capítulo 7 se aborda otro tipo de heterouniones de materiales 2D formadas por un semiconductor 2D colocado entre dos electrodos de grafeno. La motivación para realizar estos “sandwiches” es incrementar la eficiencia de extracción de carga del semiconductor, ya que la resistencia eléctrica del grafeno es mucho menor que la de los semiconductores 2D. En este capítulo se describe el desarrollo de una estrategia de fabricación de apilamientos verticales grafeno/InSe/grafeno a partir de grafeno fabricado por deposición química de vapor y láminas exfoliadas de InSe, proporcionando una ruta hacia la escalabilidad a grandes áreas de dispositivo. Se han medido las propiedades optoelectrónicas de estas estructuras y hemos encontrado que, debido a la alta eficiencia de extracción de los portadores de carga fotogenerados, hemos fabricado uno de los fotodetectores realizados con materiales 2D más sensibles hasta la fecha.

2 Background

2.1 Two-dimensional materials

Layered materials are materials with strong, covalent intralayer bonds and weak, van der Waals, interlayer bonds. Thin crystals down to atomic thickness can be extracted from bulk material or grown artificially and are often referred to as two-dimensional (2D) materials. Their physical properties are in many cases unique and fundamentally different from the bulk counterparts. In this section a selection of 2D materials is described. This selection has been made in case of graphene, for its high conductivity; MoS_2, for being the most thoroughly studied 2D material with a non-zero bandgap; BN, for being physically similar to graphene but having a wide bandgap; and InSe, for its bandgap in the low infrared range and environmental stability, all of which is described in more detail below.

2.1.1 Graphene

In 2004 researchers at the University of Manchester isolated graphene, a monolayer of carbon atoms arranged in a hexagonal lattice [1]. Graphene has remarkable mechanical and electrical properties [2,3], specifically, exceptionally high electrical and thermal conductivity. Many of the properties arise from the bonding of carbon atoms within the latice.

The ground state of a single carbon atom is $1s^2 2s^2 2p^2$. If a bond to another atom is formed, electrons can be redistributed by rearranging the electrons amongst 2s and 2p orbitals in a process called hybridisation. One of the possible hybridisations consists of a linear combination of one s-orbital and one p-orbital, which results in a linear arrangement of the bonds. The sp-hybridised orbitals form linear chains (such as alkynes, e.g. C_2H_2). Another possible hybridisation consists of an s-orbital and three p-orbitals, resulting in sp^3-orbitals with tetrahedral symmetry. The bonds within these orbitals give rise to three-dimensional structures such as diamond. In graphene electrons are in a sp^2 hybridised state. Covalent σ-bonds are formed by the valence electrons that hold the carbon atoms in a honeycomb structure. The hybridised orbitals form an angle of 120° to each other and lie in the x-y plane. The length of each

σ-bond is 0.142 nm. The bonding energy of 4.3 eV gives graphene its mechanical strength. The remaining dangling $2p_z$ orbital of each atom can form π-orbitals with nearest neighbours which gives rise to the high electronic conductivity.

The geometrical arrangement of the atoms results in a linear dispersion relation for charge carriers in graphene close to the Fermi energy [4] which is characteristic of massless relativistic particles. This leads to a conical shape of the energy - wave vector dependence in the vicinity of the Fermi-level, a significant difference compared to semiconductors which have a quadratic dispersion. This gives rise to possibility to reach high charge carrier mobilities of up to of 200,000 cm^2/Vs [5] at room temperature, which exceeds the carrier mobilities of silicon and GaAs. The combination of high conductivity at room temperature [1,6], ready availability, optical transparency and high mechanical stability makes graphene a widely used electrode material for research studies.

The objective of the work in this thesis was to integrate graphene with molecular systems and layered semiconductors to create novel prototype structures. develop new electronic devices. We have followed two strategies in order to work towards this objective. Firstly, we have conducted a study of the adsorption and interactions of molecules, namely alkanes, on graphene, see chapter 4. Secondly, we have developed a fabrication procedure to process graphene contacts onto layered semiconductors to form hybrid graphene/InSe devices, see chapter 7.

2.1.2 Molybdenum disulfide

The absence of a band gap makes graphene unsuitable for some applications and sparks interest in other 2D materials. Transition metal dichalcogenides (TMDCs) are layered semiconducting materials, for example WS_2, $MoSe_2$, WSe_2, and $MoTe_2$. The most studied TMDC is MoS_2, which has been investigated in the fields of lubrication, photovoltaics, and batteries (for a review see [7]). A layer of MoS_2 is composed of stacked S-Mo-S atom triples in a hexagonal structure, as shown in Figure 1. There is another, octahedral, structure which is of less importance for this thesis. Multilayer crystals and bulk material consist of layers separated by 0.65 nm [8].

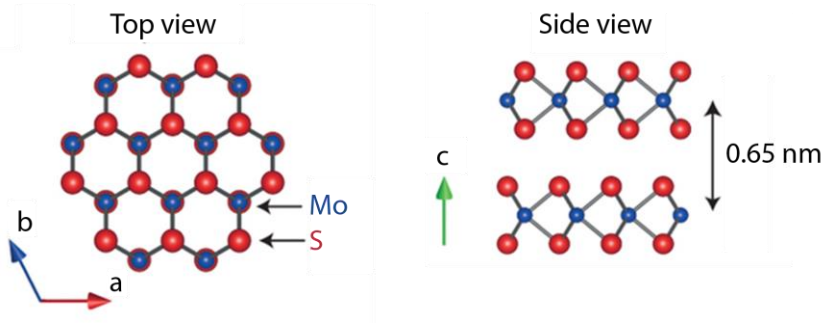

Figure 1: Ball-and-stick model of the bulk crystal structure of MoS_2 in top and side view. Adapted from reference [9].

A source of great excitement is the thickness dependence of a range of properties, for example, the band gap increases from 1.29 eV in the bulk form to 1.83 eV in a monolayer and changes from being indirect to direct [10]. Such thickness-dependent band structure variations are particularly interesting for optoelectronic devices. The first optoelectronic device based on monolayer MoS_2 showed a photosensitivity of ~1 mA/W, and short switching times, ~50 ms [11]. Shortly after, the thickness-dependence of the band gap has been confirmed in photo-transistors [12]. The optical band gap has been found to be ~1.82, ~1.65, and ~1.35 eV for mono-, two-, and three-layers respectively.

2.1.3 Hexagonal boron nitride

Hexagonal boron nitride is another member of the 2D materials catalogue. The physical structure is very similar to graphene. In a monolayer, B and N atoms are placed alternatingly in a honeycomb lattice with a lattice constant of 0.252 nm. BN is electrically insulating, has a band gap of ~5 eV, is chemically inert, stable in air, and atomically smooth [13]. It has been found that graphene-based devices exhibit highest performance when the graphene is placed onto or covered by BN. When graphene is encapsulated by BN layers, electron mobilities comparable to devices in which graphene is suspended and measured in ultra-high vacuum can be achieved [14]. This and the potential to build graphene/BN hybrid devices in which BN acts as a tunnelling barrier sparks much of the scientific interest in BN.

2.1.4 Indium Selenide

Another 2D material, relevant for chapter 7, is γ-indium selenide (InSe). Four hexagonally arranged monoatomic layers (lattice constant: 0.400 nm) are covalently bonded in the sequence Se-In-In-Se, forming one layer of InSe, see Figure 2. These InSe-layers are stacked in an ABC configuration and bonded with van der Waals forces. The unit cell contains three of these InSe-layers. The lattice constant along the vertical axis is c = 2.496 nm, see Figure 2. InSe is a direct band gap semiconductor with an energy gap of 1.26 eV [15] as opposed to other bulk layered crystals such as BN or MoS_2, which exhibit indirect band gaps in their bulk form. InSe exhibits a higher environmental stability than few-layer black phosphorous and a higher room-temperature mobility, i.e. above 1000 cm^2/Vs when encapsulated in BN layers, than few-layer dichalcogenides [16], and is therefore promising as a constituent of nanoelectronic devices.

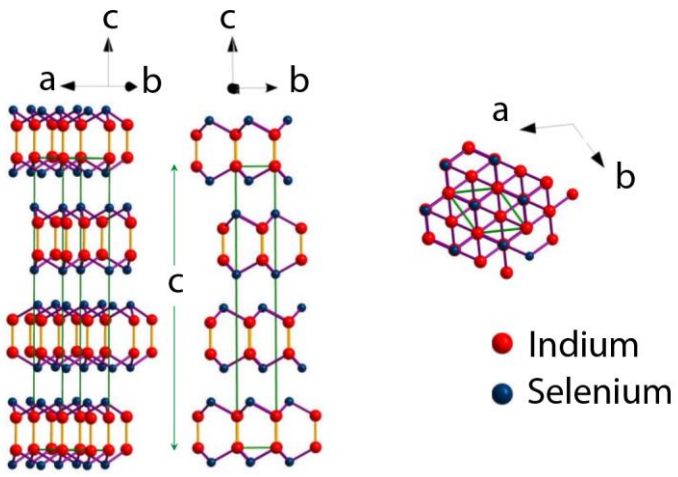

Figure 2: Crystal structure of γ-InSe. The primitive unit cell has a lattice parameter $c = 2.496$ nm and contains three layers each consisting of four closely-packed, covalently bonded, monoatomic sheets in the sequence Se-In-In-Se. Within each plane, atoms form hexagons with a lattice parameter of 0.400 nm.

2.1.5 Exfoliation, growth and transfer

Micromechanical exfoliation is a widely-used technique to isolate graphene and other 2D materials. Monolayers and few-layer-flakes are peeled from bulk material when adhesive tape is brought into contact with the bulk crystal and removed. The flakes can be transferred with the adhesive tape to a variety of substrates. Oxidised Si is often chosen as the substrate due to the high quality and low cost and because gating can be realised by applying a voltage to the Si substrate, resulting in a variation of the charge density in deposited flakes. Following mechanical exfoliation, suitable flakes with a given thickness, for example monolayers, can be identified amongst a variety of flakes with different shapes and thicknesses. Atomically clean layers can be obtained but the size of the crystals is limited to tens of micrometers. Hence, only unique prototype devices can be fabricated and a technique to synthesise large area material is necessary to incorporate 2D materials in industrial applications.

Instead of exfoliating flakes directly onto a target substrate, graphene and other 2D materials can be exfoliated onto viscoelastic stamps. The flakes on the stamp can be inspected optically and a particular flake may be chosen. Subsequently the flake can be transferred onto a surface by pressing the viscoelastic stamp against the substrate and releasing it slowly or in the presence of heat [17]. In comparison to direct exfoliation onto a substrate, this technique facilitates the alignment of the flake to a structure on a pre-patterned surface or other flakes, offering a route to combine several flakes in vertical stacks.

As an alternative to mechanical exfoliation from graphite, graphene can also be synthesised by either chemical reduction of graphene oxide which can be synthesised by treating bulk graphite with strong oxidisers [18], yielding material with a high density of structural defects; or the desorption of Si from SiC, leaving multilayered graphene [19]; or chemical vapour deposition (CVD) techniques [20,21]. To obtain graphene by CVD a hydrocarbon in the gas phase is passed at high temperatures (~900 °C) over the surface of Ir [22], Ru [23], Ni [24], or Cu. The most established synthesis process is annealing copper foils up to 1000 °C in the presence of methane, causing graphene to grow across the entire surface. Typically over 95% of the surface is covered with single-layer graphene which is an advantage over growth on other metals [21]. The orientation of grains with respect to each other determines the quality of the graphene sheet. Misaligned grains merge to form defective grain boundaries that degrade the mechanical and electrical properties [25,26]. The substrate may be pre-treated to cause ordered graphene growth in which the grains

are aligned. It has been found that unidirectional aligned graphene grains merge to a uniform graphene sheet (on hydrogen-terminated germanium) without producing defective grain boundaries [27]. For the work described in chapter 4 we used graphene grown by Neil R. Wilson and Alexander J. Marsden (University of Warwick) using the CVD-method and Cu substrates.

In many cases, CVD graphene must be transferred to an arbitrary substrate without significant mechanical damage or chemical alteration. The most widely used method is a polymer-supported transfer, in which the graphene is covered with a polymer film, most commonly PMMA (polymethyl methacrylate), before the metal is etched with iron chloride or ammonium persulfate. The polymer film provides physical robustness and prevents the graphene from tearing. The polymer/graphene can then be transferred onto a target substrate and the polymer may be removed eventually. This technique has been applied by many groups and constantly refined. For example additional water or HCl baths [28] are used to clean residues from the etching solution or copper. It has been found that the graphene can be patterned before the transfer [29]. An additional layer of PMMA before removal prevents the formation of cracks [30]. Thermal treatment in vacuum [31], Ar/H_2 [32], or N_2/H_2 [33] at 200-400 °C after the removal of PMMA has been shown to reduce chemical residues. The placing onto the target substrate can be conducted including an alignment step in order to place the graphene onto a defined position [34], which, similarly to the viscoelastic stamping, offers a route to combine graphene with other 2D materials in vertical stacks, often called van der Waals structures.

2.1.6 Van der Waals structures

2D materials can be assembled into vertical heterostructures. The creation of such artificial materials offers a way to combine the unique properties of 2D materials to form devices that present unprecedented functionality. Besides attempts to create devices with entirely novel characteristics, much research effort is directed to imitate established technology. For example, transistors, photodiodes, and sensors have been fabricated using 2D materials. Such devices have the potential to be produced cheaply and outperform existing technology.

The p-n junction is of particular interest because it is one of the most essential building blocks of semiconductor technology. To build a p-n junction materials with p- and n-type charge transport are necessary. However, 2D materials have a natural

propensity for either type charge transport due to the amphoteric doping behaviour of native point defects [35]. Therefore, p-n junctions have usually been made of dissimilar materials. In [36], C. Lee et al. have analysed charge transport in an atomically thin p-n heterostructure made of MoS_2 and WSe_2 monolayers, shown in Figure 3.

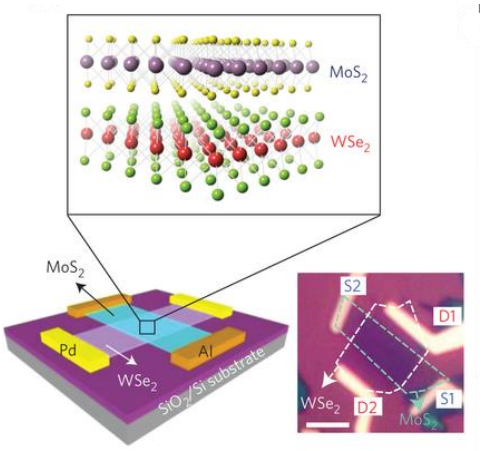

Figure 3: Bottom left: Schematic diagram of a van der Waals-stacked MoS2/WSe2 heterojunction device with lateral metal contacts. Top: enlarged crystal structure, with purple, red, yellow and green spheres representing Mo, S, W and Se atoms, respectively. Bottom right: Optical image of the fabricated device, where D1 and D2 (S1 and S2) indicate the metal contacts for WSe_2 (MoS2). Scale bar, 3 μm. Adapted from [36].

They argue that, due to space restrictions, no built-in potential associated to a depleted region builds up. They find current rectification in their p-n junctions similar to classical p-n junctions but it is found that the carrier transport across the boundary between the p-side and the n-side is not driven by diffusion processes of minority carriers as in bulk p-n junctions, but rather through tunnelling-assisted interlayer recombination of majority carriers. Therefore, the Shockley p-n junction model does not suffice atomically thin devices based on monolayers and the question arises if this model is sufficient to describe few-layer devices, which motivated the study of few-layer p-n junctions in chapter 6.

An alternative way to use the concept of selective contacts in 2D materials is to contact a crystal with an n-type material from one and a p-type material from the other side[37,38]. Free electrons and holes generated by light absorption inside the

crystal may then be selectively extracted from the contacts, generating a photovoltaic response. It is crucial for electron-hole pairs to survive sufficiently long to reach the contacts before they annihilate through recombination, which is why this concept has only been successfully realised in thin, vertical heterostructures. The charge transport in such devices is also fundamentally different from the ordinary p-n junctions which is part of the motivation for the study presented in chapter 6.

2.2 Molecular self-assembly

Molecular self-assembly is a process in which molecules spontaneously form ordered aggregates. Technological interest lies in self-assembly on surfaces as self-assembled layers can be incorporated in devices such as organic thin-film transistors, light-emitting diodes, photovoltaic cells, and memory devices. Furthermore, directed self-assembly has the potential to serve as a nano-fabrication technique for molecular electronics.

2.2.1 Self-assembly on surfaces

A great variety of molecular compounds are chemically synthesised routinely in order to exploit their properties in technological applications, in which molecules are typically adsorbed on a substrate. Adsorbed molecules can interact with each other, the surface and the environment and under certain conditions the single molecular compounds spontaneously form a supramolecular architecture that exhibits high short range order [39,40]. The mechanisms that cause this molecular assembling on a surface are under ongoing investigation with the aim to create environments that guide the assembly process and outcome. Applications of self-assembled layers are surface functionalisation and patterning with a bottom-up strategy [41–43]. For example, an established application is the surface modification of dielectrics with self-assembled thiols to change the hydrophilicity, electrostatics or to promote adsorption from solution [43]. In the field of molecular electronics self-assembled monolayers can act as the active component for charge carrier transport [44], a light emitting or sensing component [45] or a gate insulator [46]. The possibility to create meta-materials by incorporating different molecular components into self-assembled

layers widens the possible properties of functional nano-architectures beyond the properties of a single molecular species.

The formation of a supramolecular layer starts with the adsorption of molecules. The surface represents an energy landscape and an adsorbate can be trapped in local minima. Under certain conditions, most commonly when enough thermal energy is available, an adsorbate may leave a local minimum which is related to an energy cost known as the diffusion barrier. Diffusing adsorbates can move across the surface and may find another energetically favourable position. Adsorbates may approach each other and interact due to van der Waals forces, hydrogen bonding, or π-π stacking. The formation of intermolecular bonds between individual molecules is the nucleation of a supramolecular structure and may be accompanied with a reduction in energy. If the addition of further molecules to the nucleation site reduces the total energy, the molecular network grows. In this case the probability for desorption and diffusion is reduced for each bound molecule with respect to the unbound state. The over-all stability of the network is governed by the type of bonding and the influence of the surface.

The structure of the self-assembly is governed by adsorbate-substrate and adsorbate-adsorbate interactions. Examples for self-assembled monolayers which are driven by either van der Waals forces or hydrogen bonding are presented next, followed by an example of a self-assembled monolayer on which the surface has a major impact, such as it is the case in chapter 4. If the cohesion of a molecular network is governed by van der Waals interactions, the attractive electrostatic forces between molecular constituents are maximised in order to minimise the total energy. This leads to close packing and the geometry of the ordered array simply depends on the shape of the single molecule. For example, C_{60} molecules on Au(111) form hexagonal close packed arrays, see Figure 4.

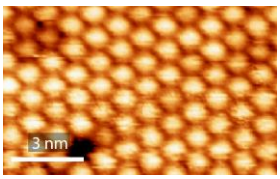

Figure 4: STM image of a self-assembled monolayer of C_{60} on Au(111). The C_{60} are hexagonally close packed.

A hydrogen bond can be formed when a hydrogen atom is covalently bond to a highly electronegative atom. The electron distribution is shifted to the electronegative atom and the hydrogen atom is left with a locally positive charge. The bond is formed when another highly electronegative atom is located in the potential minimum of the resulting dipole field. The orientation of the field defines the relative organisation of adjacent molecules and thus, the geometry of the array. An example for a hydrogen bonded array is shown in Figure 5.

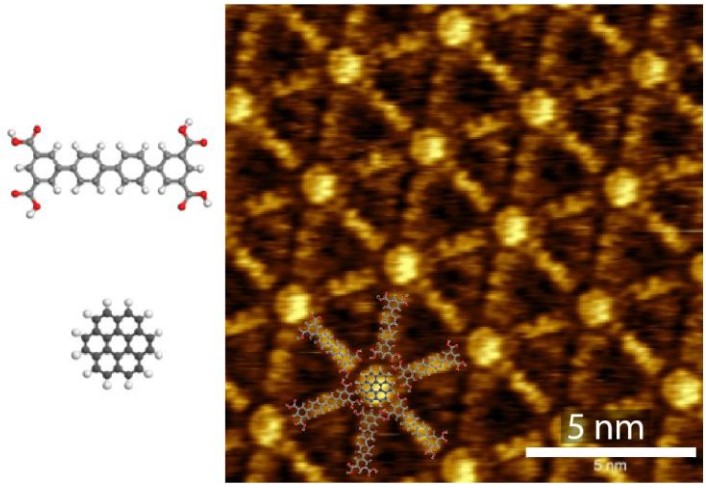

Figure 5: Schematic of QPTC (top, left) and coronene (bottom, left). STM image of a hydrogen bonded network of QPTC and coronene on graphene/copper. The schematic of the molecules is overlayed in the STM image to illustrate the geometry. Thanks to Izabella Cebula for providing the image.

The surface is the interface on which the assembly process takes place. Common substrates for the study of self-assembly are Au(111) and highly orientated pyrolytic graphite (HOPG). The strength of surface-adsorbate interactions depends on the geometry between the surface atoms and the adsorbate and thus, the symmetry of the surface atoms can guide the molecular self-assembly and may cause directional growth, see Figure 6 (i.e. 3-fold symmetry in HOPG and herringbone structure in Au(111)). Surface defects or step edges can influence the surface-adsorbate interaction locally and can be preferred adsorption sites, for example for C_{60} on Au(111). In the past, scanning probe studies revealed many details about the effects of the surface on molecular self-assembly. However, studies unravelling the possibility of the self-assembly modifying the surface are sparse, probably due to the

lack of a responsive surface. However, we found such a surface, which is discussed comprehensively in chapter 4.

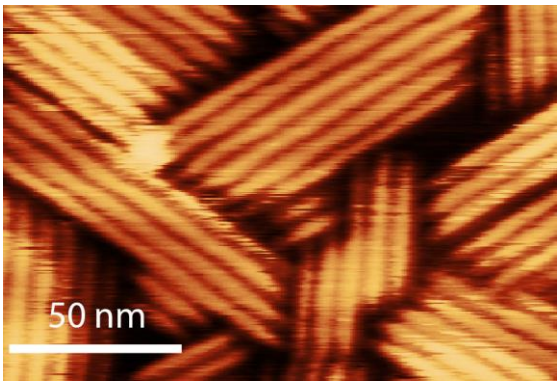

Figure 6: AFM micrograph of 10,12-Pentacosadiynoic acid on graphite. The orientation of self-assembled arrays of 10,12-Pentacosadiynoic acid is governed by the underlying HOPG surface.

Molecular self-assembly on a surface occurs upon either vapour or solution deposition. To study the fundamentals of self-assembly the impact of environmental effects ought to be minimised. Therefore, many studies are carried out in ultra-high vacuum in which vapour deposition is the relevant approach. To generate vapourised molecules in ultra-high vacuum the molecules are typically sublimed. To sublime a compound, it is placed in a vacuum chamber facing the target substrate and then heated above its sublimation temperature, usually in a Knudsen cell. The molecules are vapourised and condense on the substrate. Another common technique is deposition from solution whereby a solution of molecules in a solvent is drop-cast onto the substrate. Some molecules can overcome the molecule-solvent bonding and adsorb on the surface, which is a common approach to generate substrate-supported molecular self-assemblies. The growth of highly ordered monolayers with a size up to centimetres has been achieved with this approach, which has been used in the study in chapter 4.

2.2.2 Alkanes on graphite

In chapter 4, a study of the adsorption of alkanes on graphene is presented, which can be viewed in the context of earlier work, since the formation of self-assembled layers of alkanes on graphite has been studied intensively. The high availability, simple structure, and controllable length has made alkane chains an attractive molecule to study self-assembly on surfaces. Early studies of the adsorption of alkanes have been conducted in 1991 [47] and there is still experimental and theoretical interest to-date [48,49]. Upon solution deposition on HOPG, alkanes form a supramolecular arrangement that can be imaged with STM with intramolecular resolution, see Figure 7.

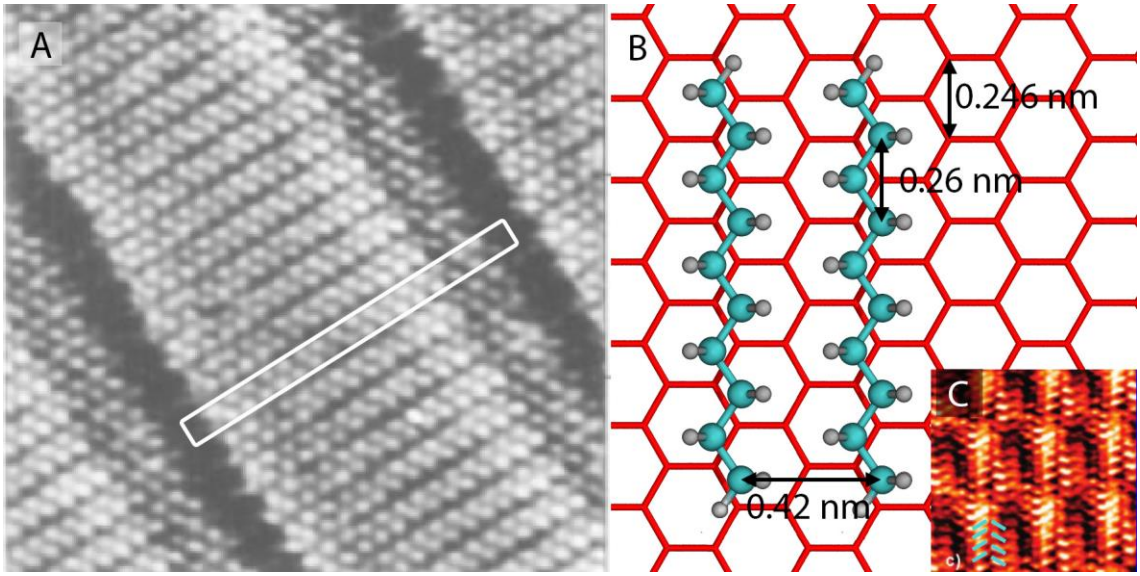

Figure 7: A) STM image of pentatriacontane ($C_{35}H_{72}$) at the liquid-graphite interface. The white box indicates the approximate location of a single molecule, size: $(7.5\ nm)^2$. 17 bright spots indicate the position of the upfacing hydrogen atoms in the alkane chain (from [50]). The molecules are orientated with the carbon backbone parallel to the graphite surface. B) Ball-stick model of decane ($C_{10}H_{22}$) on graphite. The carbon atoms in the centre of the molecule lie in their preferred adsorption site. C) Octane (C_8H_{18}) on graphite at 80 K. Short alkanes arrange in a herringbone configuration. The green markers indicate the molecular orientation (from [51]).

Long *n*-Alkanes ($n > 10$) on graphite form a self-assembled monolayer with the molecular axis parallel to the graphite surface and perpendicular to the lamella

boundaries, see Figure 7A. The separation of the lamellar rows corresponds to the molecular length and is determined by the number of carbon atoms per alkane. The bright features can be assigned to the positions of the upward-facing hydrogen atoms of each (CH_2)-group, showing the zig-zag structure of the alkane.

There is a mismatch between the graphene lattice constant and the separation of alternate carbon atoms in the alkane, see Figure 7B. Consequently, the carbon atoms along the alkane are adsorbed in different registry relative to the underlying carbon atoms in the substrate which gives rise to a moiré-like contrast variation along each molecule. The energetically preferred registry of an individual carbon atom of the alkane with respect to the underlying surface has been determined with STM studies [50] with a varying tunnelling current and is depicted in Figure 7B.

Short *n*-alkanes ($n < 10$) adsorb with two different morphologies, depending on the parity of *n* [51]. The morphology of alkanes with an even (odd) number of carbon atoms exhibits a herringbone (rectangular, such as for long alkanes) structure, see Figure 7C. There are only sparse examples of self-assembly on graphene and no prior studies of alkanes on graphene. Here, in chapter 4, the self-assembly of alkanes on graphene are discussed.

2.3 The Seebeck effect

The Seebeck effect is the direct conversion of a temperature gradient across a material ∇T into a voltage ∇V. Their relation is given by

$$\nabla V = -S\,\nabla T \tag{1}$$

whereby S is the thermopower, also called Seebeck coefficient, of the material. It is typically given in V/K and is a measure of the by a temperature gradient induced voltage. It originates from different physical phenomena depending on whether the charge transport is classical or quantised, which is discussed in the following. This discussion is relevant for the results in chapter 5, in which it is argued, that the cross-plane thermopower of MoS_2 is quantised.

2.3.1 Classical thermopower

In a classical conductor, electron transport can be described by the transport equation

$$\boldsymbol{J}_n = \mathrm{q}n\boldsymbol{E}\mu_n + qD_n\frac{dn}{d\boldsymbol{r}} \tag{2}$$

where $\boldsymbol{J}_n$ is the electron current density, q is the electron charge, $\boldsymbol{E}$ is the electric field, μ_n is the electron mobility, D_n is the diffusivity, $\boldsymbol{r}$ is the position vector, and n is the electron density. The first term in the equation accounts for drift and the second term accounts for diffusion. In the presence of a temperature gradient, an additional term is added to account for thermal diffusion. The origin of the thermal diffusion current

$$\boldsymbol{J}_{ThD}(\boldsymbol{r}) = \mathrm{q}n\boldsymbol{v_{th}}(\boldsymbol{r}) \tag{3}$$

in which $\boldsymbol{v_{th}}(\boldsymbol{r})$ is the thermal drift velocity, lies in the different thermal movement of the electrons at different temperatures. It can be calculated as follows, following Demtröder, W. [52].

The electrons scatter with the atoms of the conductor. On average, after a scattering event at the position $\boldsymbol{r} - \lambda\hat{\boldsymbol{v}}$ an electron scatters again at the position $\boldsymbol{r}$, where it has the mean velocity $\bar{v}(T)$, where λ is the mean free path, and $\hat{\boldsymbol{v}} = \boldsymbol{v}/\bar{v}$ is the direction of the velocity. It is assumed that the velocity of an electron at the

position $\boldsymbol{r}$ is determined by the temperature at the position of the last scattering event $\boldsymbol{v} = \hat{\boldsymbol{v}}\,\bar{v}(T(\boldsymbol{r} - \lambda\hat{\boldsymbol{v}}))$. Taking into account all electrons, the drift velocity is the average of the velocities between the scattering events, $\boldsymbol{v_{th}}(\boldsymbol{r}) = \langle \boldsymbol{v} \rangle$, which can be found by integrating $\boldsymbol{v}$ over all directions

$$\boldsymbol{v_{th}}(\boldsymbol{r}) = \langle \boldsymbol{v} \rangle = \frac{1}{4\pi} \int \hat{\boldsymbol{v}}\,\bar{v}(T(\boldsymbol{r} - \lambda\hat{\boldsymbol{v}}))\mathrm{d}\Omega \tag{4}$$

Since we consider scattering in a bulk sample, the temperature changes and thereby the velocity changes are small over a distance of the mean free path (several nm). We can therefore approximate $T(\boldsymbol{r} - \lambda\hat{\boldsymbol{v}}) \approx T(\boldsymbol{r}) - \lambda\hat{\boldsymbol{v}}\,\nabla T(\boldsymbol{r})$ and $\bar{v}(T(\boldsymbol{r} - \lambda\hat{\boldsymbol{v}})) \approx \bar{v}\big(T(\boldsymbol{r})\big) - \lambda\hat{\boldsymbol{v}}\,\nabla T(\boldsymbol{r})\frac{\mathrm{d}\bar{v}}{\mathrm{d}T}$. Equation (4) becomes then

$$\boldsymbol{v_{th}}(\boldsymbol{r}) = \frac{1}{4\pi} \int \lambda\hat{\boldsymbol{v}}\,\frac{\mathrm{d}\bar{v}}{\mathrm{d}T}\nabla T(\boldsymbol{r})\mathrm{d}\Omega = \frac{1}{3}\lambda\frac{d\bar{v}}{dT}\nabla T(\boldsymbol{r}) \tag{5}$$

By plugging this into equation (3), the total current density (equation (2)) becomes

$$\boldsymbol{J}_n = \mathrm{q}n\boldsymbol{E}\mu_n + qD_n\frac{dn}{d\boldsymbol{r}} + \frac{1}{3}\mathrm{q}n\lambda\frac{d\overline{\boldsymbol{v}}}{dT}\nabla T(\boldsymbol{r}) \tag{6}$$

Since there is no change in carrier density in the conductor, the regular diffusion term ($qD_n\frac{dn}{d\boldsymbol{r}}$) vanishes. The thermopower is defined in open-circuit conditions ($\boldsymbol{J}_n = 0$), and we use $\boldsymbol{E} = -\nabla\mathrm{V}$. We hence find that a temperature change along the conductor results in a voltage difference

$$0 = -\mathrm{q}n\,\nabla\mathrm{V}\,\mu_n + \mathrm{q}n\frac{1}{3}\lambda\frac{\mathrm{d}\overline{\boldsymbol{v}}}{\mathrm{d}T}\nabla T(\boldsymbol{r})$$

$$\Rightarrow\ \nabla\mathrm{V}\ = \frac{\lambda}{3\mu_n}\frac{\mathrm{d}\overline{\boldsymbol{v}}}{\mathrm{d}T}\nabla T(\boldsymbol{r}) \tag{7}$$

By comparing this result with the definition of the thermopower, equation (1), we identify

$$S = -\frac{\lambda}{3\mu_n}\frac{\mathrm{d}\overline{\boldsymbol{v}}}{\mathrm{d}T} \tag{8}$$

It can be concluded that the classical thermopower is a result of a thermally induced current. It is dependent on the mean free path of the electrons and their mobility, which in turn depends on the involved scattering mechanisms. This explains that metals, in which the mean free path is typically large, have small thermopowers (1-10 μV/K) and semiconductors have higher thermopowers with a strong dependence on the doping (0.1-10 mV/K). It also implies the qualitative result that typically, the thermopower rises with the resistance of a material. Furthermore, it becomes evident that in quantum systems, where the mean free path is much longer than the trajectory inside the conductor, a different mechanism causes the thermopower.

2.3.2 Quantum thermopower

The quantum-equivalent of the classical thermopower occurs in the presence of a temperature gradient across a conductor with dimensions on the nanometre scale. We consider a region with a length of several nanometres L with macroscopic contacts. Such a system can be illustrated as shown in Figure 8. An electron can freely travel through the contacts, which are typically metals in which electrons fill up all states below the Fermi level E_F (at T = 0 K). The potential in nanometre-scale junction region is generally unknown.

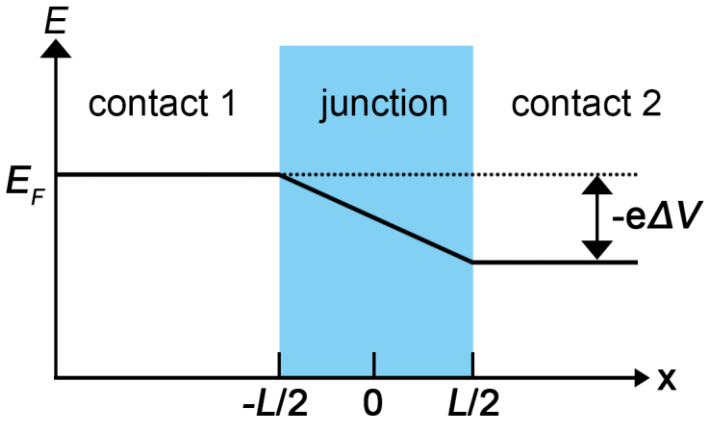

Figure 8: Illustration of a system in which a region of length *L* is sandwiched in between two metal electrodes. A bias voltage *ΔV* is applied which shifts the fermi levels of regions I and III with respect to each other.

When a voltage bias ΔV is applied between the contacts, the Fermi level in contact 2 shifts downwards with respect to contact 1. Electrons in the energy levels E_n between $E_F - \Delta U$ and E_F are then impinging from contact 1 onto the junction, with $\Delta U = -e\Delta V$. Their total magnitude in Coulomb per second is the incoming current

$$I_{in} = -2en \sum_{E_F-\Delta U}^{E_F} v_n \tag{9}$$

where n is the electron density and v_n are the velocities of the electrons in the in the energy levels E_n. A part of the electrons in this current will pass through the junction. The relation between the incoming current and the current I that passes through the junction is given by

$$I = I_{in}T \tag{10}$$

where T is defined as the transmission, which in general depends on the energy levels and potential landscape in the junction.

Here, we consider the junction region to be a quantum-sized conductor and can find an explicit expression for I, by assuming T = 0 K, as follows. The quantum mechanical description of a conductor confined in a very narrow space is known as the *particle in a box* model. By solving the Schrödinger equation

$$\left(\frac{-\hbar^2}{2\mu}\nabla^2 + U(x)\right)\Psi = E\Psi \tag{11}$$

with the boundary conditions $U(x) = 0$ for inside the barrier region and $U(x) = \infty$ outside this region, one can solve for the electron wave function Ψ and the allowed energy levels, where $\hbar = h/2\pi$ is the Planck constant divided by 2π, $U(x)$ is the potential energy, E is the total energy. The energy levels of a *particle in a box* system are

$$E_n = \frac{n^2\pi^2\hbar^2}{2mL^2} = \frac{k_n^2\hbar^2}{2m} \text{ with } k_n = \frac{n\pi}{L} \tag{12}$$

and the corresponding electron wave functions are

$$\Psi_n = \frac{1}{i\sqrt{2L}}\left(e^{ik_n x} - e^{-ik_n x}\right) \tag{13}$$

The particle density is

$$n = \frac{1}{2L} \tag{14}$$

With these equations one can find an explicit expression for equation (10) for the metal/square well potential/metal system, as follows. $\sum v_n$ is transformed into an integral using equation (12), that is $\Delta k = k_n - k_{n-1} = \pi/\mathrm{L}$:

$$\sum v_n = \frac{L}{\pi}\sum v_n \frac{\pi}{L} = \frac{L}{\pi}\sum v_n \Delta k = \frac{L}{\pi}\int v\, dk \tag{15}$$

One can identify $v = \hbar k/\mathrm{m}$ as $v = \frac{1}{\hbar}\frac{dE}{dk}$ from equation (12) and solve $\int v\, dk$:

$$\int_{E_F-\Delta V}^{E_F} v\, dk = \int_{E_F-\Delta V}^{E_F} \frac{1}{\hbar}\frac{dE}{dk}\, dk = \frac{1}{\hbar}(E_F - (E_F - \Delta U)) = \frac{1}{\hbar}\Delta U \tag{16}$$

By collecting the equations (9), (12), (13), (14), and $\Delta U = -e\Delta V$, we find the explicit expression for equation (10), which is called the Landauer formula:

$$I = \frac{2e^2}{h}\Delta V\, T \quad \text{or} \quad G = \frac{I}{\Delta V} = \frac{2e^2}{h}\, T \tag{17}$$

where G is the conductance. It relates the conductance to the transmission through a quantum-sized conductor. It implies that $\frac{2e^2}{h} \approx 77$ μS is the conductance quantum G_0, which is the conductance of a quantum-system if transport occurs through one level through which the transmission probability is 1. As mentioned above, this implies the assumption that T = 0 K.

For finite temperatures the Landauer formula has the general form

$$I = \frac{2\mathrm{e}}{h}\int_{-\infty}^{\infty} T(E)\left(f_1(E) - f_2(E)\right) dE \tag{18}$$

in which $f_1(E)$ and $f_2(E)$ are the electron distributions on either side of the junction at contact 1 and 2, given by the Fermi-Dirac distribution

$$f_{1/2} = \left(\exp \frac{\left(E - \mu_{1/2}\right)}{\mathrm{k_B} T_{1/2}} + 1 \right)^{-1} \tag{19}$$

To find the thermopower we set equation (18) to zero since the thermopower is defined in open-circuit conditions.

$$0 = \frac{2\mathrm{e}}{h} \int_{-\infty}^{\infty} T(E) \left(f_1(E) - f_2(E) \right) dE \tag{20}$$

This equation implies the qualitative result: To satisfy the charge neutrality, that is zero current, while the Fermi distributions f_1 and f_2 are dissimilar because of a difference between T_1 and T_2, the chemical potentials μ_1 and μ_2 will be displaced causing a potential difference V given by $-\mathrm{e}\nabla V = \mu_1 - \mu_2$. More formally, as in Büttiker et al. [53], we perform a Taylor expansion of $f_2(E)$ around T_1 and μ_1, $f_2(E, \mu_2, T_2) \cong f_2(E, \mu_1, T_1) + \frac{\partial f_2}{\partial \mu}(\mu_1 - \mu_2) + \frac{\partial f_2}{\partial T}(T_1 - T_2)$, write the derivatives in the form of energies, $\frac{\partial f}{\partial T} = -\frac{E-\mu}{T}\frac{\partial f}{\partial E}$ and $\frac{\partial f}{\partial \mu} = -\frac{\partial f}{\partial E}$, plug these terms into equation (20) and solve for $(\mu_1 - \mu_2)/(T_1 - T_2)$, which yields

$$\frac{\mu_1 - \mu_2}{T_1 - T_2} = \frac{1}{T(E)} \int_{-\infty}^{\infty} T(E) \frac{E - \mu}{T_1} \frac{\partial f}{\partial E} dE \tag{21}$$

We solve for the thermopower, using $-\mathrm{e}\nabla V = \mu_1 - \mu_2$ and equation (1). The integral can be solved using the Sommerfeld expansion[54]:

$$S = \frac{\nabla V}{T_1 - T_2} = \frac{\pi^2 k_B^2 T_1}{3e} \left. \frac{\partial \ln\left(T(E)\right)}{\partial E} \right|_{\mu_1} \tag{22}$$

We find that the quantum thermopower is proportional to the differential transmission at the chemical potential. It can therefore be positive or negative, depending on whether electrons above or below the chemical potential have a higher transmission probability. In contrast to the classical case the quantum thermopower is independent of scattering giving quantum thermopower great promise for applications, since the transmission can be engineered by varying the band structure

and alignment of the contacts and the energy levels in the conductor through selection of the chemical composition and structure of the materials.

Quantum thermopower has been studied in molecular junctions [55] and atomic-size contacts [56], which yield relatively low values of up to $|S| = 40$ μV/K, although theoretical calculations indicate that much higher values should be possible [57]. In chapter 5, a study is presented in which we demonstrate the first measurements of quantum thermopower in the cross-plane direction of a 2D material. We find values of up to $|S| = 330$ μV/K in thin layers of MoS_2, present the number of layer dependence of conductance and thermopower and relate our results to density function theory calculations of the transmission.

2.3.3 Thermoelectric Cooling

An application of thermoelectric materials is cooling of electronic equipment. The ongoing miniaturisation of electronic components leads in many cases to localised hot regions, for example on printed circuit boards, generating demand in localised cooling techniques which can be realised by thermoelectric elements with high heat-flux pumping capability.

To find an expression for the heat flux $\boldsymbol{q}$, consider a thermoelectric material between a cold and a hot side, such as in Figure 9. The heat flux is then given by how much heat is carried with the electron current $ST\boldsymbol{J}$ (also called Peltier heat flow), opposed by the heat conduction $k\nabla T$ [58],

$$\boldsymbol{q} = ST\boldsymbol{J} - k\frac{dT}{dx} \tag{23}$$

where $\boldsymbol{J}$ is the current density, and k is the thermal conductivity. The rate of heat generation by Joule heating is given by [58],

$$\frac{d^2T}{dx^2} = -\frac{\boldsymbol{J}^2\rho}{k} \tag{24}$$

where ρ is the electrical resistivity of the material. Note, that it has been assumed, in equation (24), that S is independent of the temperature. This assumption is reasonable in the relatively small temperature interval 300-330 K used in the study discussed in chapter 5.

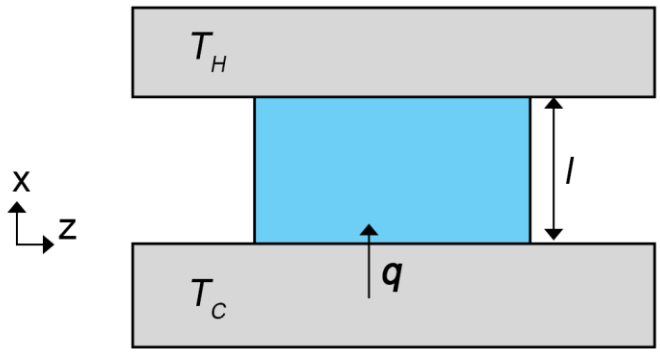

Figure 9: Schematic of thermoelectric refrigerator. Blue: thermoelement with thickness *l* between hot and cold sides.

The general solution for this differential equation is

$$T(x) = -\frac{\boldsymbol{J}^2\rho}{2k}x^2 + bx + c$$

and the unknowns, b and c, are found assuming the boundary conditions $T(0) = T_C$ and $T(l) = T_H$,

$$T(x) = -\frac{\boldsymbol{J}^2\rho}{2k}x^2 + \frac{1}{l}\left(T_H - T_C + \frac{\boldsymbol{J}^2\rho}{2k}l^2\right)x + T_C \qquad (25)$$

This can be plugged into 23 to find the heat flux,

$$\boldsymbol{q}(x) = -\frac{S\boldsymbol{J}^3\rho}{2k}x^2 + \frac{S\boldsymbol{J}}{l}\left(T_H - T_C + \frac{\boldsymbol{J}^2\rho}{2k}l^2\right)x + S\boldsymbol{J}T_C + \boldsymbol{J}^2\rho x - \frac{k}{l}\left(T_H - T_C + \frac{\boldsymbol{J}^2\rho}{2k}l^2\right)$$

The heat flux $\boldsymbol{q}(x)$ is evaluated at $x = 0$ and $x = l$, since these correspond to the boundaries to the hot and the cold side, respectively. They both reduce to the same expression

$$\boldsymbol{q}(0) = \boldsymbol{q}(l) = S\boldsymbol{J}T_C - \frac{\boldsymbol{J}^2\rho l}{2} - \frac{k}{l}(T_H - T_C) \qquad (26)$$

The heat flux through any of these boundaries can be maximised for a current density, which is found (by $\frac{\boldsymbol{dq}(0,l)}{\boldsymbol{dJ}} = 0$) to be $\boldsymbol{J} = \frac{ST_C}{\rho l}$. Consequently, the maximum high heat-flux pumping capability is

$$\boldsymbol{q}(0)_{\boldsymbol{max}} = \frac{1}{l}\left(\frac{S^2 T_C^2}{2\rho} - k(T_H - T_C)\right) \tag{27}$$

In conclusion, the maximum heat pumping capacity of a thermoelectric element is inversely proportional to the device thickness. This consideration is a motivation of the study in chapter 5, in which the maximum heat flux capacity of a 2D material with thicknesses in the nanometre-range is determined.

2.4 Shockley p-n junction model

p-n junctions serve as energy-harvesting, light-emitting, and rectifying devices. Due to their great impact, research in p-n junctions has been ongoing for decades and a deep understanding of the physical phenomena involved has been established. With the advent of 2D materials which can be processed into atomically thin p-n junctions, new questions have arisen regarding to which extent classical models can describe quantum-size p-n junctions. This section is concerned with the derivation of the Shockley diode equation, which describes the current-voltage characteristics of a classical ideal p-n junction. This derivation and its implications are crucial for the results in chapter 6, in which it is argued that current-voltage characteristics of few-layer MoS_2 p-n junctions can be described by this classical model.

2.4.1 p-n junction in equilibrium

p-n junctions are based on the concept of selective contacts. In the n-type material mainly electrons move freely through the conduction band and in the p-type material, mainly holes move through the valence band. In the n-type region the Fermi energy is closer to the conduction band and in the p-type material it is closer to the valence band. When they are brought into contact a p-n junction forms at the boundary. The charge carrier flow in a semiconductor in general and in particular in a p-n junction is described, as above, by the transport equation:

$$\begin{aligned} \boldsymbol{J}_n &= +\mathrm{q}n\boldsymbol{E}\mu_n + qD_n\frac{dn}{dx} \\ \boldsymbol{J}_p &= -\mathrm{q}p\boldsymbol{E}\mu_p - qD_p\frac{dp}{dx} \end{aligned} \tag{2}$$

where $\boldsymbol{J}_n$ is the electron current density, q is the electron charge, $\boldsymbol{E}$ is the electric field, μ_n is the electron mobility, D_n is the diffusivity, and n is the electron density. The same equation applies to holes with the indices p. The electron density n (or hole density p) equals the dopant concentration if all dopants are ionised and is, hence, often referred to as the doping. The first term in the equations accounts for drift and the second term accounts for diffusion.

Another fundamental equation is the Poisson equation $d\boldsymbol{E}/dx = \rho/\varepsilon$, which relates the charge density $\rho = \mathrm{q}n$ and the electric field. ε is the material permittivity. The continuity equation takes account for the total number of holes or electrons

$$\begin{aligned} \frac{dn}{dt} &= +\frac{1}{q}\frac{d\boldsymbol{J}_n}{dx} + G - U \\ \frac{dp}{dt} &= -\frac{1}{q}\frac{d\boldsymbol{J}_p}{dx} + G - U \end{aligned} \tag{28}$$

where G is the generation rate and U is the recombination rate. The generation rate (in 1/s) accounts for the due to light adsorption generated electron-hole pairs per time, and the recombination rate (in 1/s) accounts for the electrons and holes that annihilate each other. This means that a change in charge carrier density is accompanied by carrier generation, recombination or a change in the current density.

This set of differential equations have an analytical solution for a p-n junction when it is assumed that the electric field is spatially restricted to the space charge region which contains the boundary between the p-side and the n-side. Assuming that the space charge region is depleted of free carriers and the physical boundary between the p-side and n-side is abrupt the equations can be solved for the electric field in the space charge region, its width, and the in-built voltage. A rigorous derivation of the quantities can be found in Luque and Hegedus [59]; the qualitative results are shown in Figure 10, which shows the band structure of a p-n junction in equilibrium, that is in the dark without a bias.

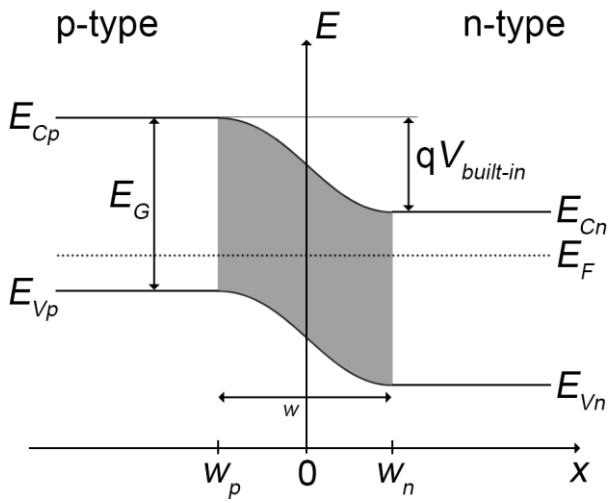

Figure 10: Band structure of an ideal p-n junction in equilibrium. The space charge region marked in grey.

The p-type semiconductor is drawn on the left side of the origin; the n-type is on the right side. At the boundary, there is a steep gradient between the electron and hole densities n and p, which causes diffusion of electrons to the p-part and holes to the n-part where they recombine with the majority carriers. This causes a depletion of free carriers in the area around the boundary, marked in grey, which is the space charge region. Dopant atoms remain in this area causing an electric field E pointing from the n- to the p-part. A drift current arises due to the electric field which counteracts the diffusion current and as a result the total current is zero. The built-in field is related to the built-in voltage by $V_{built-in} = \int_{wp}^{wn} E\mathrm{dx}$, due to which the bands bend in the space charge region, between w_p and w_n, matching the position of the Fermi energy in the neutral regions, far away from the boundary. This is the starting point for the derivation of the Shockley diode equation.

In the following the conduction and valence band edges on the p-side is called E_{Cp} and E_{Vp}. Analogously, on the n-side the band edges are called E_{Cn} and E_{Cn}. The width of the space charge region be w, reaching from w_p to w_n.

2.4.2 Carrier diffusion due to a voltage bias

To find the current through the p-n junction we consider the minority carrier concentration at the border of the space charge region on the n-side. In thermal equilibrium, the carrier concentration $p(w_n)$ follows the Fermi distribution

$$p(w_n)_{equ} = p_0 \exp\left(-\frac{E_F - E_{Cn}}{kT}\right) = p_0 \exp\left(-\frac{E_F - \left(E_{Cp} - \mathrm{q}V_{built-in}\right)}{kT}\right) \qquad (29)$$

where p_0 is the hole equilibrium carrier concentration. An external bias V_{SD} disturbs the equilibrium conditions and shifts the bands in the n- and p-part with respect to each other, and hence the in-built voltage is reduced. $p(w_n)$ becomes

$$p(w_n)_V = p_0 \exp\left(-\frac{E_F - \left(E_{Cp} - \mathrm{q}(V_{built-in} - V_{SD})\right)}{kT}\right) \qquad (30)$$

From these two equations, (29) and (30), and the definition $p(w_n)_{equ} = p_n^0$ we find the excess hole concentration $\delta p(w_n)$ due to the external bias

$$\delta p(w_n) = p(w_n)_V - p(w_n)_{equ} = p_n^0 \left(\exp\left(\frac{\mathrm{q}V_{SD}}{kT}\right) - 1\right) \qquad (31)$$

We find the dependence on the x by setting as a boundary condition an exponential decay of the carrier concentration in the space charge region

$$\delta p(x) = \delta p(w_n) \exp\left(\frac{w_n - x}{L_p}\right) \qquad (32)$$

where L_p is the hole diffusion length. Note, that this exponential decay implies the assumption that the space charge region stays depleted although carriers are injected due to the bias (low-injection approximation). This assumption is true for all p-n junctions in almost all conditions [59].

The dependence of the hole diffusion current on the excess hole concentration is given by the transport equation (equation (2)). Note that $\boldsymbol{E}$ is zero at the border of the space charge region and $\frac{dp}{dx} = \frac{d\delta p}{dx}$, because p and δp differ only by a constant.

$$J_p(w_n) = -qD_p \left.\frac{dp}{dx}\right|_{w_n} = \frac{qD_p p_n^0}{L_p}\left(\exp\left(\frac{qV_{SD}}{kT}\right) - 1\right) \quad (33)$$

An equivalent derivation can be done for the electron current density which leads to $J_n(w_p) = \frac{qD_n p_p^0}{L_n}\left(\exp\left(\frac{qV_{SD}}{kT}\right) - 1\right)$ at the other border of the space charge region on the p-side. Assuming there is no generation or recombination, the total current density in the junction is the sum of both, yielding the Shockley equation

$$J = \left(\frac{qD_p p_n^0}{L_p} + \frac{qD_n p_p^0}{L_n}\right)\left(\exp\left(\frac{qV_{SD}}{kT}\right) - 1\right) = J_0\left(\exp\left(\frac{qV_{SD}}{kT}\right) - 1\right) \quad (34)$$

where $J_0 \equiv \left(\frac{qD_p p_n^0}{L_p} + \frac{qD_n p_p^0}{L_n}\right)$, which is called the reverse saturation current density. This means that the current through a p-n junction goes exponential with the voltage, or, in other words, a p-n junction rectifies current. We can draw further conclusions from qualitative considerations. The current grows exponentially with a forward bias until the total current is affected by resistances of the circuit. For a negative bias a, comparably, small current flows in the other direction until the band bending is strong enough for E_{Vp} to exceed E_{Cn}, in which case a tunnelling current contributes to J.

2.4.3 Generation and recombination

Generation in the space charge region, which is caused when the junction is illuminated can be accounted for, by an additional term in equation (34), which, assuming constant generation, is $\Delta J_p(w_n) = -qGL_p\tau_p$ or, for electrons $\Delta J_p(w_p) = -qGL_n\tau_n$, where $L = \sqrt{D\tau}$ is the diffusion length, which is the average length between generation and recombination and τ is the carrier lifetime. The total current of an illuminated p-n junction is therefore

$$J = J_0\left(\exp\left(\frac{qV_{SD}}{kT}\right) - 1\right) - qG\left(L_p\tau_p + L_n\tau_n\right) = J_0\left(\exp\left(\frac{qV_{SD}}{kT}\right) - 1\right) - J_{SC} \quad (35)$$

$-J_{SC} = -qG\left(L_p\tau_p + L_n\tau_n\right)$ is the short-circuit current, a current that is induced by carrier generation in the space charge region and diffusion of electrons to the n-side

and holes to the p-side. This direction is opposite to the current induced by a positive V_{SD}.

In the derivation until equation (35), recombination in the space charge region has not been taken into account. In practical solar cells recombination in the space charge region can take place via localised levels in the band gap which occur due to imperfections in the semiconductor lattice. This has been proposed and discussed by Shockley, Read, and Hall and is therefore named Shockley-Read-Hall recombination. One can find an analytical expression for the current density occurring from this type of recombination if the traps lie half-way between the valence and conduction band

$$J_{SRH} = J_{01}\left(\exp\left(\frac{qV_{SD}}{2kT}\right) - 1\right) \tag{36}$$

with a given reverse saturation current density J_{01}. Taking Shockley-Read-Hall recombination into account the total current density becomes

$$J = J_0\left(\exp\left(\frac{qV_{SD}}{kT}\right) - 1\right) + J_{01}\left(\exp\left(\frac{qV_{SD}}{2kT}\right) - 1\right) - J_{SC} \tag{37}$$

Note that the expression for J_{SRH} is very similar to the equation (34), which describes the current density due to diffusing carriers which recombine band-to-band. The difference is the 2 in the denominator of the exponent, which is called the ideality factor, abbreviated as n. When additional recombination mechanisms are taken into account, each mechanism adds an additional term, similar to equation (36), to the total current density. Each type of recombination mechanism, be it Auger recombination or radiative recombination, has a typical n and an extraction of n from $I-V$ characteristics of a real p-n junction can give insight into the involved mechanisms. This is further discussed in the chapter 6 concerning a p-n junction made of thin layers of MoS_2.

3 Experimental techniques

3.1 Scanning tunnelling microscopy

The scanning tunnelling microscope (STM) was invented by Gerd Binnig and Heinrich Rohrer in the 1980s. STM allows the investigation of the electronic structure of surfaces and adsorbates with atomic resolution. For the design of the STM, Binning and Rohrer were awarded with the Nobel Prize in physics in 1986. In scanning tunnelling microscopy, a sharp metal tip is brought into close proximity, typically several Å, with the surface under investigation. A bias voltage is applied between the tip and the surface which causes electrons to tunnel from the tip to the surface or vice versa. When the tip is raster-scanned across the surface, the physical topography of the surface and adsorbates give rise to variations in the tunnelling current. The current is measured and used as a feedback parameter which is compared with a previously defined target value, which is typical of the order of 1 nA. A feedback circuit continuously adjusts the distance between the tip and the surface (z-direction) in order to keep the tunnelling current constant. The position of the tip (x,y,z) is recorded for a given number of points (n(x), n(y)) and can be displayed as an image, see Figure 11.

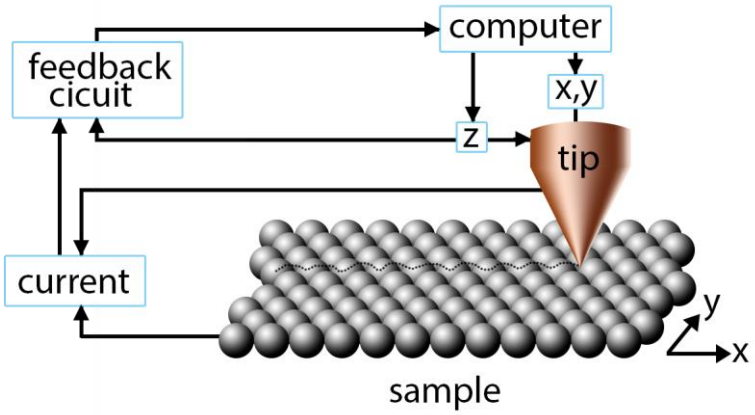

Figure 11: Scanning tunneling microscopy principle. A tip is raster-scanned across a surface in the x and y directions. The tunneling current is measured while a feedback circuit is used to adjust the tip-surface separation. x, y, z are monitored and displayed as an image.

A quantum mechanical description of an electron penetrating a potential barrier provides an understanding of an STM topography image. Figure 12 illustrates the tunnel effect through a potential barrier.

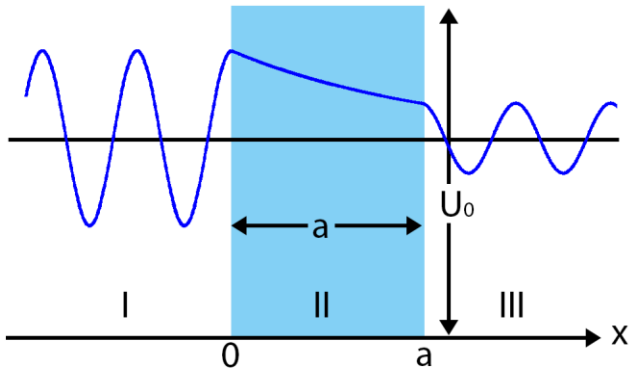

Figure 12: Tunnelling of an electron through a potential barrier (II) in 1D. An electron is incident from the tip I, tunnelling through vacuum (II) to the sample (III).

The form of the wave function along the tunnelling direction satisfies the Schrödinger equation.

$$-\frac{\hbar^2}{2m}\frac{\mathrm{d}^2}{\mathrm{d}x^2}\Psi(x) + U(x)\Psi(x) = E\Psi(x) \tag{38}$$

where $\Psi(\mathrm{x})$ is the electron wave function, m is the electron mass, $U(x)$ is the potential and E is the energy of the electron. In region II the wave function that describes an electron moving in the +x direction with energy $E < U(x)$ is $\Psi(x) = \Psi(0)\exp(-\kappa x)$ with $\kappa = \sqrt{2m(U_0 - E)}/\hbar$. For thick barriers ($\kappa d \gg 1$) the probability P of an electron passing through the barrier is exponentially dependent on the barrier width.

$$P \propto |\Psi(a)|^2 \propto \exp(-2\kappa a) \tag{39}$$

Thus, the tunnelling current ($I \propto VP$. V is the applied voltage bias) decreases exponentially with increasing separation between sample and tip.

In 1960 Bardeen developed a theoretical method to explain tunnelling between superconducting electrodes separated by a thin oxide layer [60]. This theory also

describes the tunnelling current in the tip-sample system. The transition probability for transfer from state Ψ_l in one electrode to a state Ψ_r in the other is given by Fermi's Golden Rule

$$\Gamma = \frac{2\pi}{\hbar}|M|^2\delta\left(E_{\Psi_l} - E_{\Psi_r}\right) \tag{40}$$

if only elastic tunnelling is considered and the tunnelling current is

$$I = \frac{2\pi e}{\hbar}\sum_{l,r}|M_{lr}|^2\delta(E_l - E_r)f(E_l)\left(1 - f(E_r + eV)\right) \tag{41}$$

Bardeen calculated the transition matrix element M_{lr} using the approximation that the setup can be considered as two independent systems (for wide barriers, i. e. weakly coupled), each with separate wave functions (Ψ_l and Ψ_r). The approximation is valid because the magnitude of the wave function of each side of the barrier is small in the barrier and on the other side of the barrier, see Figure 13.

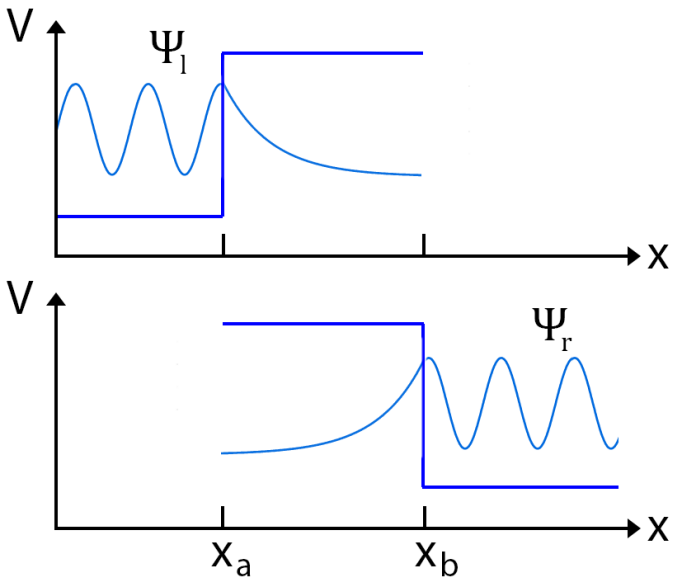

Figure 13: The potentials V_l and V_r of the left and the right system in Bardeen's derivation of the transition probability. The barrier extends from x_a to x_b.

M is determined by the overlap of the wave functions of the two subsystems at a surface S which lies entirely in the barrier region

$$M = \frac{\hbar^2}{2m}\int_S (\Psi_r^* \nabla \Psi_l - \Psi_l \nabla \Psi_r^*)\, \mathrm{d}S \tag{42}$$

For a formal derivation see, for example, "Scanning Probe Microscopies Beyond Imaging" by Samorí [61].

Tersoff and Hamman applied the Bardeen model to describe the STM tip-sample system. They used Bloch wave functions as an approximation for the surface (Ψ_r) described the tip with an s-wave function (Ψ_l) derived an expression for the tunnelling current from equation (41) and (42).

$$I = \frac{32\pi^3 e^2}{\hbar} V R^2 e^{-2\kappa R} \frac{1}{\kappa^4} \varphi^2 \rho_l \sum_S |\Psi_S(\boldsymbol{r_0})|^2 \delta(E_S - E_F) \tag{43}$$

*w*ith the further assumptions that the temperature is $T = 0$ K, the voltage V is small and the barrier is thick. This implies that the tunnelling current in STM depends on the radius of curvature of the tip R, the inverse decay length κ, such as in equation (39), the work function φ, which is approximately equal for sample and tip, the density of states of the tip ρ_l, the surface states Ψ_S with energy E_S and the Fermi energy E_F.

It also depends on $\sum_S |\Psi_S(\mathbf{r_0})|^2 \delta(E_r - E_F)$ which is the local density of states (LDOS) of the sample. This result is important for the interpretation of an STM-image. The image does not depict the physical topography of a surface and adsorbates but is rather a map of the LDOS.

For the study presented in chapter 4 a high accuracy in the measurement of lateral distances in the acquired STM images was crucial. However, STM images are often distorted due to thermal drift, that occurs due to thermal gradients over time and across different parts of the microscope. We hence developed the following model to correct for drift which relies on a comparison of an image with the consecutive, counter-scanned image, assuming a constant linear drift rate. All STM images in the results-chapters have been corrected for drift applying this model.

STM images are assembled from single line scans of the microscope in the x direction in a line-by-line fashion. We assume that no drift occurs during the scan of

each individual line. There are two components of drift which are to be compensated for by post-processing, drift in the x-direction and drift in the y-direction. Between the scan of consecutive lines the tip moves back from the position x=512 pixels to x=0 pixels, which needs time in which drift occurs in both, the x and the y direction. This is visualised in Figure 14.

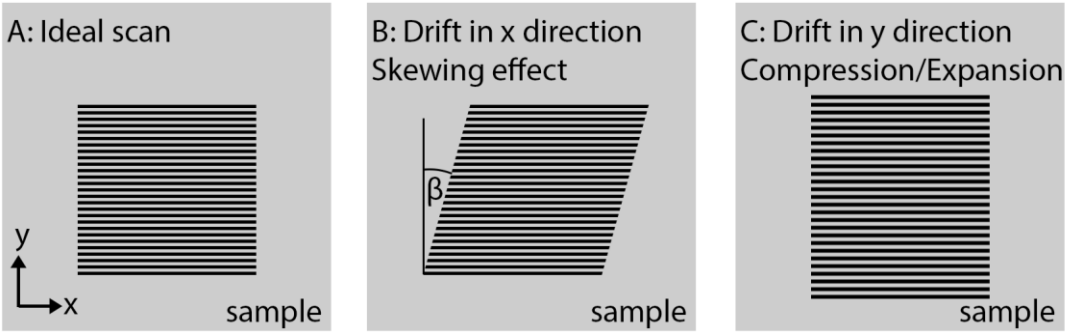

Figure 14: Visualisation of the influence of thermal drift on an STM image. Each line represents a line scan. Due to drift in the x-direction (see B) and the y-direction (see C) the accumulation of line scans does not represent a square.

The drift has a velocity $v(v_x, v_y)$ in pixels per time (t). Consider two lines, containing the pixels (x_i,y) and (x_i',y') in which i Є [1,512] giving the position of the pixel in the x-direction. We assume constant drift and hence, the lines are displaced in x with respect to each other by vt pixels, as in Figure 14 B. The time t has passed between scanning (x_i,y) and (x_i',y') so that

$$x_i' = x_i + v_x t \tag{44}$$

If v is known, an image free of drift in the x-direction can be calculated by

$$x_{i,real} = x_{i,measured} - vt \tag{45}$$

for each pixel.

To find the value of v, prominent features are chosen in two consecutively taken images, see for example the feature marked in the figure below. Figure 15A is an up scan and taken before the down scan shown in Figure 15B. The time t runs continuously during both scans; meaning that the time is t=513 when the first line

(line 512) of the down scan is measured. A feature m such as marked in Figure 15 has coordinates in pixels (x_m, y_m) in the up scan and (x_m', y_m') in the down scan.

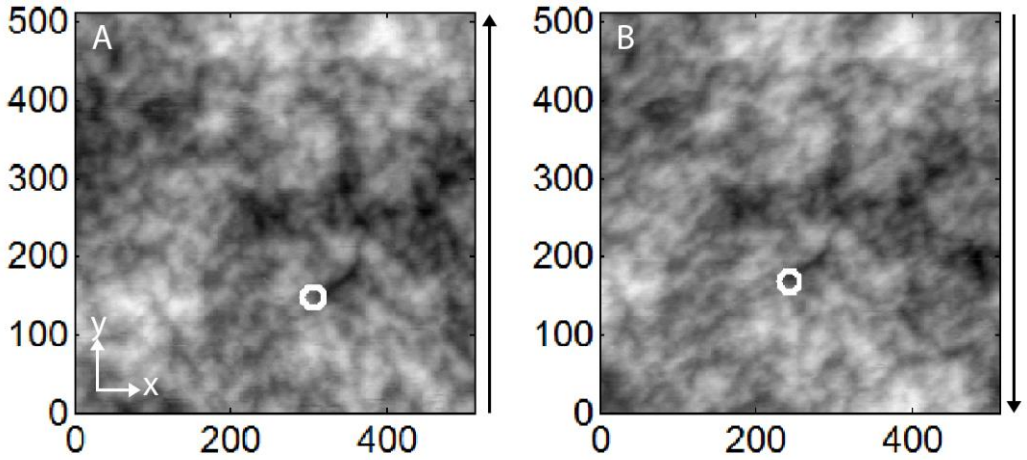

Figure 15: STM image of Graphene deposited on SiO_2 acquired in ambient conditions. Area $(95\ nm)^2$. The axis are labeled with the number of pixels i. A) Up-scan, which was taken first. B) Down-scan.

By comparing the positions (x_m, y_m) and (x_m', y_m'), the drift velocity can be determined using equation (44) as $v_x = (x_m' - x_m)/t$. This is done for 3 to 6 features per image to generate an accurate value by calculating the average. In the particular example, the correction, as shown in Figure 16, results in skewing the image by 6.8°. Similarly, the correction in the y-direction can be found by considering the line spacing γ in one scan and $1/\gamma$ in the consecutive scan, which can be determined by $\gamma = (512 - y_m)/(512 - y_m')$. In the example, this leads to a compression of the image in the y-direction by 3.96%.

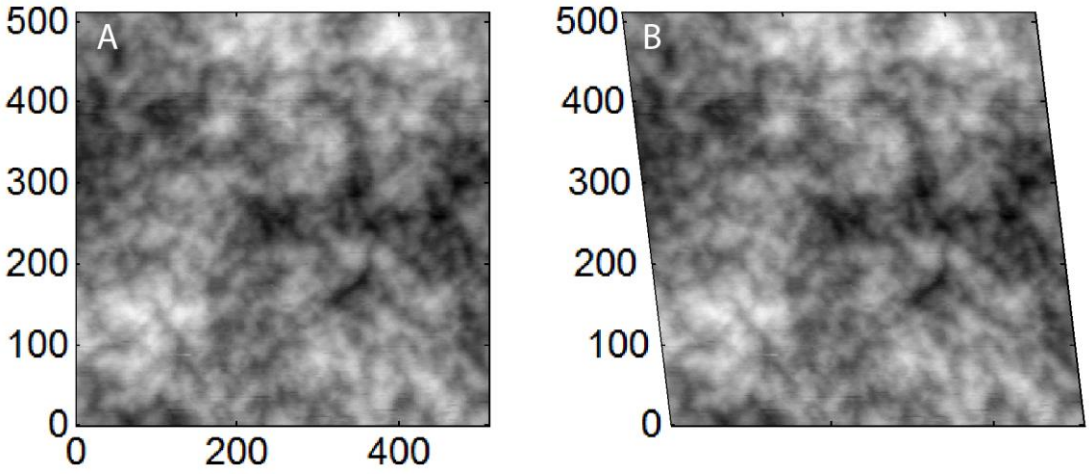

Figure 16: STM image of Graphene deposited on SiO_2 before (A) and after drift-correction (B)in the x-direction.

Drift-corrected images allow an accurate measurement of lateral dimensions. For lateral calibration, the atomic structure of graphite (0001) served as a reference, see Figure 17. An STM image of graphite with atomic resolution shows every second atom, since the LDOS over the other atoms is suppressed [62]. The characteristic distance between bright features corresponds therefore to the distance d = 0.246 nm shown in the inset in Figure 17.

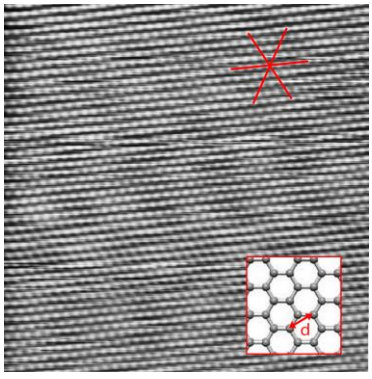

Figure 17: STM image of graphite(0001) acquired in ambient conditions. The bright features along the directions marked in red correspond to second-nearest neighbours in the graphite lattice, see inset. Their distance is d = 0.246 nm.

3.2 Conductive atomic force microscopy for high-accuracy voltage measurements

Gert Binnig, Calvin Quate, and Christoph Gerber implemented the first atomic force microscope [63]. Atomic force microscopy (AFM) is similar to STM but the feedback parameter is, instead of the tunnelling current, related to the force between the tip and the sample, which on the nanometer scale stems from van der Waals forces and Pauli repulsion. In AFM the tip is usually integrated into a micro-machined silicon cantilever to allow bending in response to changes in the forces between the surface and the tip, see Figure 18.

In the work described in this thesis two AFM's were used, a Cervantes Fullmode AFM from Nanotec Electronica SL for the results in Chapter 5 and an Asylum Research MFP-3D Infinity AFM for the results in chapter 7, in tapping mode in which the cantilever is driven to oscillate up and down near the resonant frequency (typically 50-400 kHz). The oscillation amplitude can be determined from the position of the reflection of a laser incident on the cantilever. If the cantilever is close to a surface the amplitude decreases due to changes in the force between the tip and the surface (force gradient). When the cantilever scans across the surface, the cantilever-sample separation is adjusted in order to keep the amplitude at a pre-set value. Consequently, an AFM image is a map of constant interaction-force gradient experienced by the tip.

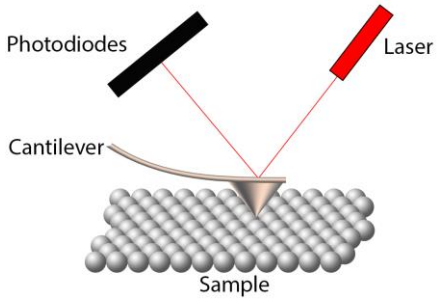

Figure 18: Diagram of an atomic force microscope. In tapping mode, the cantilever is driven to oscillate up and down. The oscillation amplitude of the cantilever can be measured using an arrangement of a laser and photodiodes. The change in the amplitude is proportional to the force gradient.

An AFM can be operated in conductive mode, in which the cantilever and the tip are made of or coated by a conductive material and a bias voltage is applied between the sample and the tip, allowing to electrically probe a sample with high spatial resolution. To enable the measurement of thermoelectric properties a hot plate was installed below the sample. When the tip is brought into light contact, i.e. with a force of several nN, with the sample, a nanometre-scale junction is formed, whose electrical and thermal resistance are high. When the sample is heated, a temperature gradient occurs across this junction causing the generation of a thermovoltage which can be measured at different points on the sample.

By sweeping the bias voltage and measuring the current, *I-V* characteristics of such nanoscale junctions can be extracted which, in the presence of a temperature gradient, typically have the form shown in Figure 19 A for small voltages (mV range). The curves are linear and their gradient is the small bias conductance in Siemens. They are offset from the point of origin by a thermally induced voltage ΔV which can be related to the thermopower of the junction using the heat circuit shown in Figure 19 B. The equations describing the voltages generated by the Seebeck effect are

$$S(T_2 - T_1) = -(V_2 - V_1)$$
$$S_{cable}(T_2 - T_0) = -(V_2 - V)$$
$$S_{cable}(T_1 - T_0) = -(V_1 - V_0)$$

where S_{cable} is the effective thermopower of the cabling connecting the measurement devices. The measured temperature gradient is $\Delta T = T_1 - T_2$ and the voltage at the voltmeter is $\Delta V = V - V_0$. Combining these equations and rearranging gives

$$S = \frac{\Delta V}{\Delta T} + S_{cable} \tag{46}$$

which allows to calculate the thermopower of the junction from the measured quantities ΔT and ΔV after S_{cable} has been determined. To find S_{cable} a wire with a well-known thermopower has been mounted into the c-AFM setup, connecting the cantilever with the surface. Using the equation above, rearranged to $S_{cable} = S - \Delta V/\Delta T$, and using a chromel wire ($S = 22$ µV/K), we find $S_{cable} = -2.2$ µV/K. This value has been confirmed using an alumel wire ($S = -18$ µV/K). Chromel and alumel are the constituent metals of K-type thermocouples. This implies that the thermopower and conductance can be determined simultaneously, which is an advantage over other techniques to measure the thermopower of small junctions

[64,65] which rely on separate measurements of the thermal voltage and the conductance.

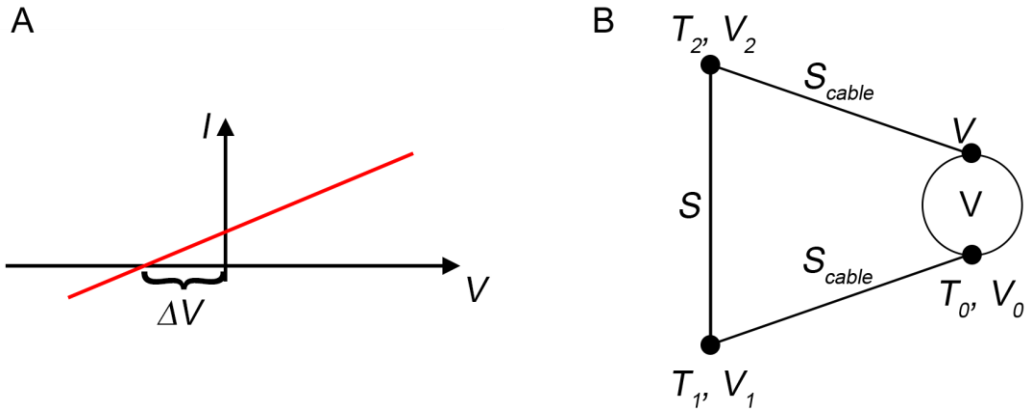

Figure 19: A) Small-bias *I-V* curve of a nanoscale-junction in the presence of a temperature gradient ΔT. The thermoelectric effect results in a shift by ΔV of the curve along the *V*-axis. B) Schematic showing the temperatures and voltages at the sample *T1, V1* and the tip *T2, V2*. The voltmeter is at temperature *T0* and measures the voltage drop *V-V0*. The thermopower of the junction is *S* and the thermopowers of the cables is S_{cable}.

We use low-noise equipment to conduct our experiments. We have built a circuit which is schematically shown in Figure 20 A, in which the voltage is given out by a data acquisition system (NI PCI-7833R) in the range -10 to 10 V and divided by R_2/R_1 = 3000 using an operational amplifier, leading to a μV precision in the bias voltage. Typical currents range from sub-nA to μA and are converted into a voltage by a low-noise current preamplifier (Stanford Research Systems SR570), which is measured by the data acquisition system. We typical use gains R_4 between 1e5 to 1e8 V/A. The latter results in a precision of approximately 30 pA in the current reading.

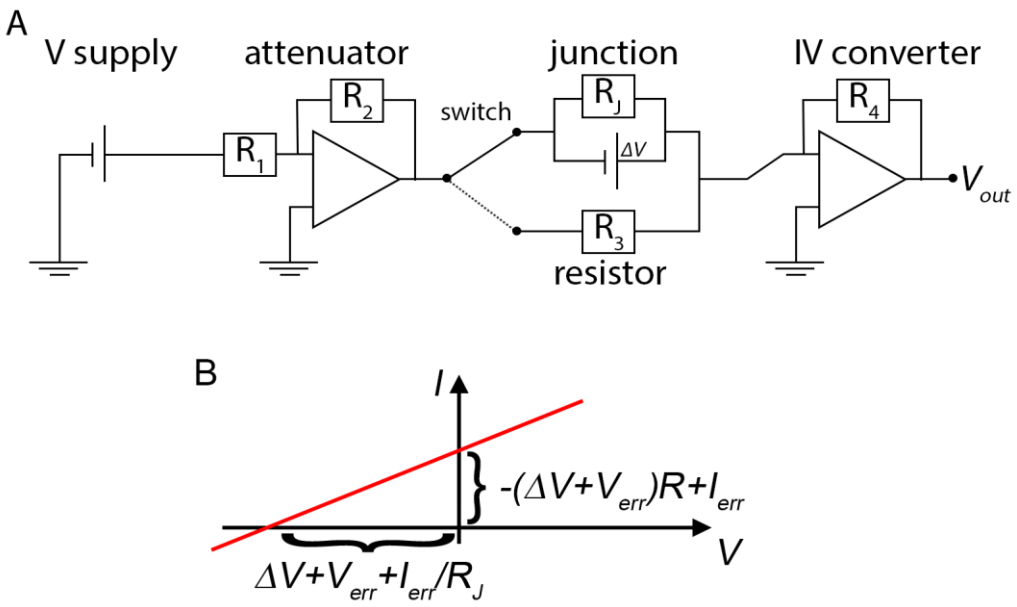

Figure 20: A, circuit schematic to acquire the data. A voltage is supplied and attenuated by a factor 3000, resulting in a bias voltage applied to either the junction, represented by a resistor R_J and a voltage supply in parallel, or to a resistor R_3. The current is converted to an output voltage V_{out}.

We have found that our measurements are always accompanied by systematic errors in the current- and voltage-reading (I_{err} and V_{err}), affecting measured *I-V* curves as shown in Figure 20 B. The errors stem from the fact that practical measurements are generally non-ideal, and, specifically, the ground on our operational amplifiers is offset and drifting when compared to the ground on the voltage supply. To account for these errors I_{err} and V_{err}, we use the switch shown in Figure 20 A. To determine the error in the current reading the AFM, and thereby junction, is disconnected resulting in an open circuit. The current measured in open-circuit conditions is generally non-zero and equal to I_{err}. To determine the error in the voltage reading the AFM is disconnected and a resistor R_3 is connected instead. Several *I-V* curves are taken over the resistor and linear regressions are used to find the crossing point of the curves with the voltage axis V_0. The error in voltage relates to this by $V_{err} = V_0 - I_{err}/R_3$. After I_{err} and V_{err} have been found, the AFM is connected to measure the sample under investigation and all data can be acquired with a correct calibration. We have found that V_{err} drifts by several µV over the course of minutes and we perform this zero-calibration therefore every two minutes as part of the experimental procedure to ensure a high measuring accuracy.

To test our setup we have reproduced the main results in Tan et al. [65] in which the thermopower of Au-1,1',4',1'' terphenyl-4-thiols-Au junctions have been determined as $S = 16.9 \pm 1.4$ μV/K. We prepared 1,1',4',1'' terphenyl-4-thiols on Au(111) by solution deposition from dichloromethane, which results in a self-assembled monolayer covering the entire surface. A thermal gradient of $\Delta T = 5$ K was applied and the tip was approached at several different positions on the sample to record approximately 100 *I-V* curves at each position. A typical *I-V* curve is shown in Figure 21 A, from which ΔV and thereby S can be determined. A histogram of S values from 600 curves is shown in Figure 21 B, from which we extract the mean value by fitting a Gaussian distribution and find S = 18 μV/K in agreement with published results [65].

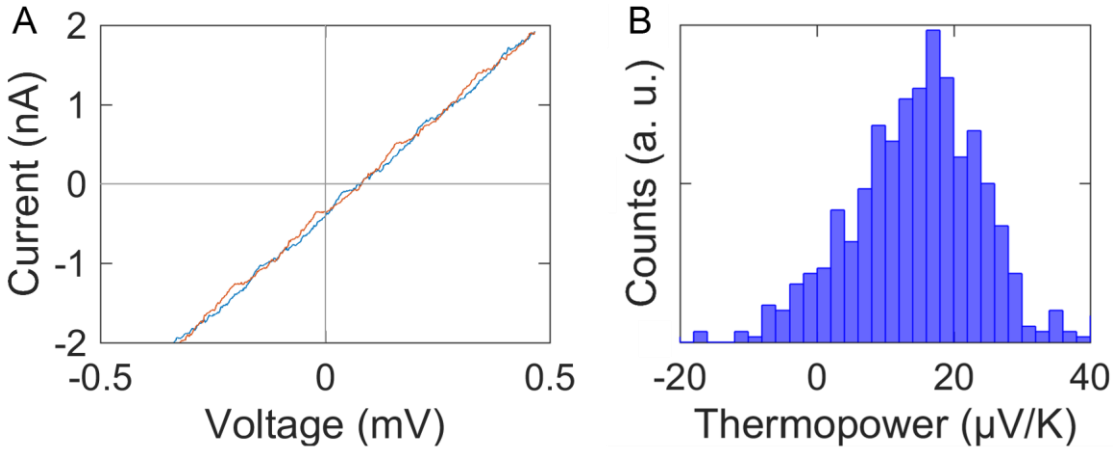

Figure 21: **A**, *I-V* curve of Pt-terphenyl thiol-Au junction in the presence of a temperature gradient of $\Delta T = 5$ K. The *I-V* curve is offset by a thermally induced voltage ΔV which relates to the thermopower by $S = -\Delta V/\Delta T$. **B**, Thermopower values extracted from 600 *I-V* curves, showing an average value of 18 μV/K.

3.3 Device fabrication techniques

2D material based devices typically have a lateral size in the micrometre scale and can therefore be processed by typical microfabrication techniques which are also used in semiconductor manufacturing. Microfabrication techniques have been used to fabricate the devices discussed in chapters 6-7 and can be divided into surface patterning, deposition, and etching which are shortly discussed in the following. For 2D materials in particular a processing technique called deterministic stamping has recently been developed which has also been used in this work and is discussed below.

Electron beam lithography (EBL) is a process used to pattern a resist on a surface. It involves the exposure of the resist by electron irradiation and the development, i.e. removal of the exposed or unexposed areas of the resist. To expose the resist, which is usually a thin film of polymers deposited by spin-coating, the sample is loaded into a scanning electron microscope (SEM). Electrons are emitted from a filament and accelerated by an electric field (30 kV) causing a beam of electrons which can be focussed by electro-magnetic lenses and impinges on the sample. The highly energetic electrons initiate chemical changes in the resist, usually a break-up of the chemical structure causing a higher solubility. The electron beam moves in a predefined path and exposes certain areas on the surface. This creates a latent image in the resist that is revealed through development. In the development step, either the exposed or unexposed part of the resist is dissolved under controlled conditions (defined temperature, composition of solvent, time scale). The fabrication steps are schematically shown in Figure 22. One distinguishes between positive and negative resist in which, respectively, the exposed or unexposed parts are dissolved. The SEM system which has been used in this work is a JEOL/XENOS JSM-7000F + XPG2. The manufacturer specifies a resolution of 30 nm at a typical writing field area of (200 μm)^2. For a positive resist, we use polymethyl methacrylate (PMMA), which is resistant to most acids and unaffected by visible or UV-light. It degrades by chain scission under electron bombardment if the energy is at least 5 eV [66]. The degraded PMMA can be dissolved selectively with respect to PMMA with higher molecular weight which remains on the wafer [67]. We used Micro Chem 498 PMMA A5 resist.

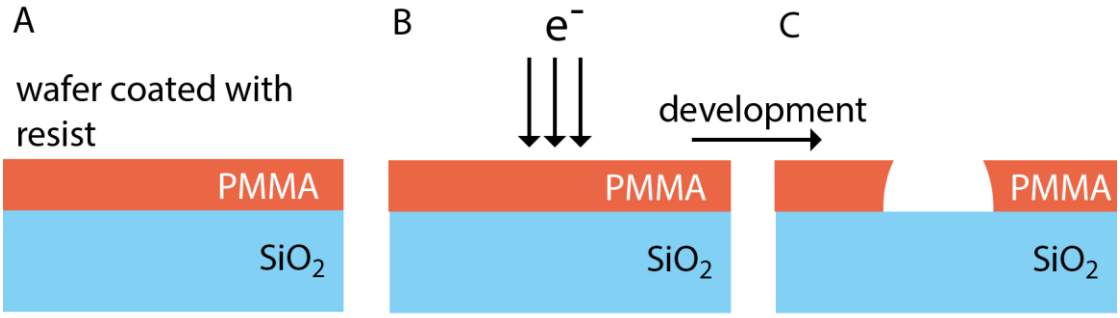

Figure 22: Schematic of EBL. A) SiO_2 wafer is covered with a PMMA. B) Electrons impinge on the surface with spatial definition and trigger a chemical modification of the resist. C) The modified resist can be dissolved in the development.

After patterning a surface, material can be deposited or removed to form a device. For the results in chapter 4-7, metal was deposited onto the surface before or after the deposition of 2D materials, in order to form electrical leads, which allow to probe the material electrically by connecting macroscopic probes. To deposit material, I used mostly thermal evaporation in vacuum. A material, typical Au, Ti, or Cr is sublimed by annealing, travels to the target substrate and condenses. This method is applied in vacuum at a typical pressure of $\sim 10^{-6}$ mbar. A low pressure is used to prevent collisions of vapourised material with atmospheric particles on the way from the source material to the target substrate. I used an Edwards Auto 306 evaporator to evaporate metals (Au, Ti, Cr, Ge, Ni, Zn). If material was deposited onto a patterned surface, the resist is usually removed afterwards, as shown in Figure 23.

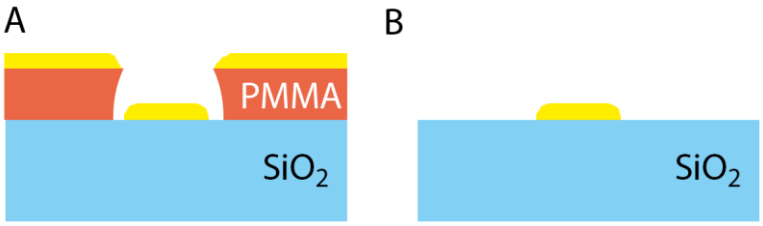

Figure 23: Schematic of metal deposition following EBL. The metal coats the entire surface area but is only in contact with the wafer in the areas which were previously defined by EBL. After removal of the PMMA, the metal is left on the surface.

In many cases, for example to form devices from CVD-graphene such as in chapter 7, material must be removed from the surface after the patterning step. To etch graphene, I used a Corial 200IL instrument reactive ion etcher (RIE). In reactive ion etching, reactive ions are generated in a plasma initiated and sustained by a strong, oscillating magnetic field. As a result the ions gain a high kinetic energy perpendicular to the sample surface and impinge on the substrate triggering a chemical reaction. The reaction products are composed of ions and substrate atoms and removed by vacuum pumps. By appropriately selecting the parameters and chemicals we achieve a selective etching of, for example, only organic material.

To form devices from non-etched 2D materials, such as in chapter 6, a processing technique has been developed independently by a number of groups [14,68,69]. This technique is typically called deterministic stamping and relies on the optical localisation of an exfoliated 2D crystal on a transparent substrate to place it at a pre-defined position, typically overlapping with electrodes or other 2D crystals that have previously been deposited. In order to do so, thin flakes are prepared by micromechanical exfoliation of bulk crystals and deposited onto a viscoelastic stamp (we use GelFilm by GelPak). Amongst a great number of exfoliated flakes one flake is chosen by optical inspection. The stamp is inverted and mounted on a micrometer stage. This allows that the stamp and thereby the flake can be placed with a high positional accuracy onto a sample. By releasing the stamp slowly from the substrate, it can be removed and the flake is transferred to the substrate.

4 Adsorbate-induced curvature of graphene

Molecular adsorption is known to modify the chemical and electronic properties of graphene [70,71] and is therefore of great interest in the context of graphene device fabrication. A method to control the spatial organisation of adsorbates is two-dimensional supramolecular assembly. Studies in this field have, so far, focused on graphene on SiC [72,73], metal surfaces [74–76], or, most relevant to potential applications [77,78], dielectrics, which results in strong adhesion and a high rigidity. These investigations have provided interesting insights, which may be understood within well-established models of molecular adsorption, whereby the graphene is treated as a passive and rigid substrate. However, one of the many interesting properties of graphene is its intrinsic flexibility [79].

Here an example is given in which the graphene actively responds to the adsorption of molecules through mechanical deformation. Specifically, in these experiments monolayer graphene is suspended between trapped water layers and an organic solvent and we observe that the supramolecular organisation of adsorbed alkanes induces curvature and anisotropic mechanical properties in the graphene. This shows that molecular adsorption can influence the mechanical properties of graphene, and is thus relevant to applications in electronic materials, membrane technologies and micromechanical systems. Additionally, this study extends current research into surface supramolecular organisation to encompass adsorption on soft, deformable interfaces which must be treated as responsive surfaces.

4.1 Formation of extended alkane layers on graphene

We have investigated the adsorption of the n-alkane, tetratetracontane (TTC; $C_{44}H_{90}$) on graphene (G) transferred to either exfoliated hexagonal boron nitride (hBN) flakes on a supporting SiO_2 layer, or onto mica [80]. hBN single crystals, were prepared by K. Watanabe and T. Taniguchi (NIMS, Japan) using previously published methodologies [81,82] and were exfoliated onto thermally oxidized Si wafers (300 nm SiO2) using Scotch tape and subsequently annealed in forming gas (5% H2 in Ar) at 400 °C to drive off tape residue. Ruby muscovite mica (Agar Scientific) was used in our experiments and was cleaved before the graphene was transferred. The graphene was grown by chemical vapour deposition on copper and provided by Neil Wilson (University of Warwick, UK).

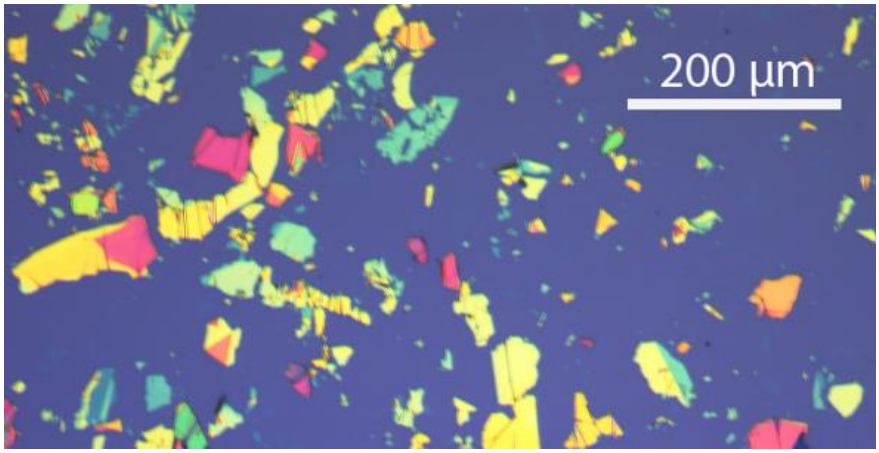

Figure 24: Optical image of hBN exfoliated onto a SiO_2/Si wafer showing a great number of flakes with lateral dimensions over 20 µm.

We tested several transfer methods similar to reference [83] and achieved our best results using the following recipe. To transfer graphene (G), G/copper was coated with PMMA and placed on a $FeCl_3$ etching solution (Transene, CE-100) until the copper was visibly gone and then left for a further 30 minutes. The PMMA/G film was placed into a HCl bath and subsequently into five de-ionised water baths for rinsing and was transferred onto the substrate. The PMMA was removed in solvent

baths (acetone, IPA) and, finally, the samples were annealed in forming gas (5% H_2 in Ar) at 400 °C for 4 hours. This results in an atomically clean surface, see Figure 25.

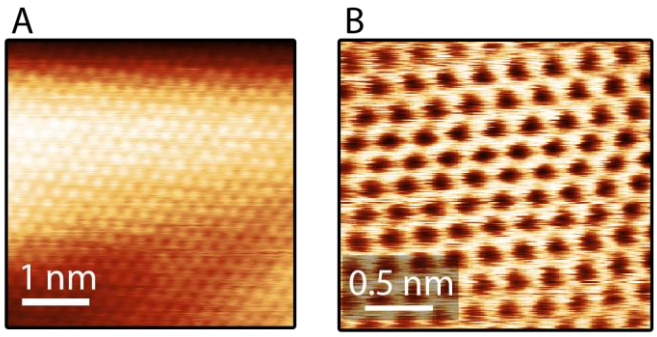

Figure 25: High resolution STM images of G/Cu (A) and G/SiO_2 (B) aquired in ambient conditions. The graphene was transferred from Cu to SiO_2 and then annealed in Ar/H_2 at 400 °C for 2 h to restore the cleanliness.

Following the preparation of G/BN and G/mica, a solution of the TTC (Sigma Aldrich, 7098-22-8) in tetradecane ($C_{14}H_{30}$) (1.32 mg/mL) was drop-deposited on the surface. Images of TTC molecules absorbed at the graphene/solvent interface were acquired using an Agilent Technologies 4500 PicoPlus STM operating in constant current mode under ambient conditions using a cut PtIr (80:20) wire as an STM tip. A metal clip holding the sample in place provided an electrical contact to the graphene layer. All images have been corrected for drift and calibrated using graphite(0001) as a reference.

The STM images of TTC on G/hBN in Figure 26 show lamellar rows of molecules which run continuously the graphene/hBN subtrate. The lamellar arrangement is clearly resolved for TTC and is very similar to the arrangement for analogue alkanes adsorbed on graphite, see chapter 2.2.2. The rows in Fig. 1a are superposed on a hexagonal moiré pattern arising from the orientational mismatch between the graphene and the hBN [84–86]. The presence of the moiré pattern confirms that the G and hBN are in direct contact, which implies that the adhesion between these surfaces is maintained in the presence of the TTC/tetradecane solution.

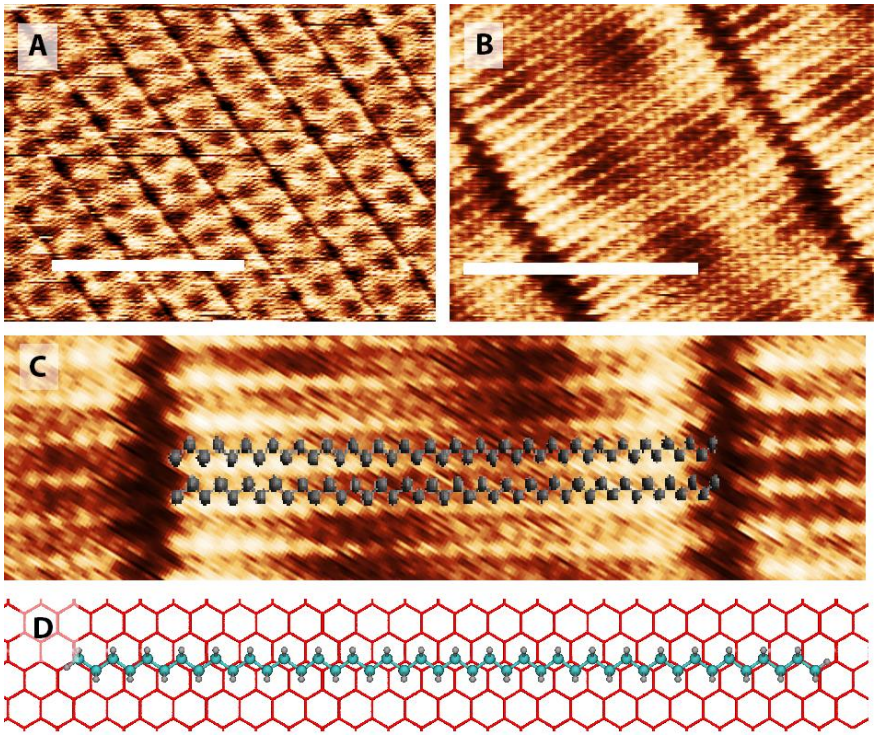

Figure 26: TTC on G/hBN A) Lamellar rows of TTC on G/BN; the G/BN moiré pattern is also resolved. Scale bar: 20 nm (sample voltage -1 V, tunnel current 0.07 nA). B) High resolution STM image of lamellar rows. Scale bar: 5 nm (-1 V, 0.1 nA). C) Zoom of (B) showing atomic resolution. D) Schematic of adsorption of an n-alkane on graphene. Due to the mismatch in lattice constants -CH2- groups are adsorbed at different local environments on the flat graphene.

The images in Figure 26B and C show the molecular arrangement within the lamellar rows and provide intramolecular resolution showing the zig-zag structure of the alkanes. The separation of the lamellar rows is 5.8±0.1 nm and corresponds to the molecular length and the separation of molecules within the row is 0.42±0.01 nm, in agreement with the expected [47,87,88] value, $\sqrt{3}a$, where a is the graphene lattice constant. Additionally, we observe a variation of topographic height (contrast) along the molecule.Figure 26 This has previously been attributed [47,87,88] to a mismatch between the graphene lattice constant and the separation of alternate carbon atoms in the alkane, $a_{alk} = a + \delta a$. A consequence of this mismatch is that not all carbon atoms in the alkane can be simultaneously adsorbed above their preferential adsorption sites, as illustrated in Figure 26D.

STM images of TTC on G/mica also show lamellar rows of molecules which run continuously over the graphene, although it is in this case significantly rougher than the graphene/BN. The image in Figure 27 shows a terrace-like morphology arising from graphene overlaid on regions where there are varying numbers of trapped water layers at the G/mica interface [89–93]. In previous studies it has been reported that trapped water forms, predominantly, ice-like monolayer or bilayer islands [89,91,92], and that graphene transfer methodologies involving the immersion of mica in water [90] result in the adsorption and trapping of at least one layer, and in most areas 2 or more layers of water. It was also found that step edges could no longer be resolved in areas with more than three water layers trapped under the graphene. In such regions the roughness increases significantly, and this was attributed to a liquid-like thicker film of trapped water [89,90]. The adsorption of molecules on such regions forms the focus of this work.

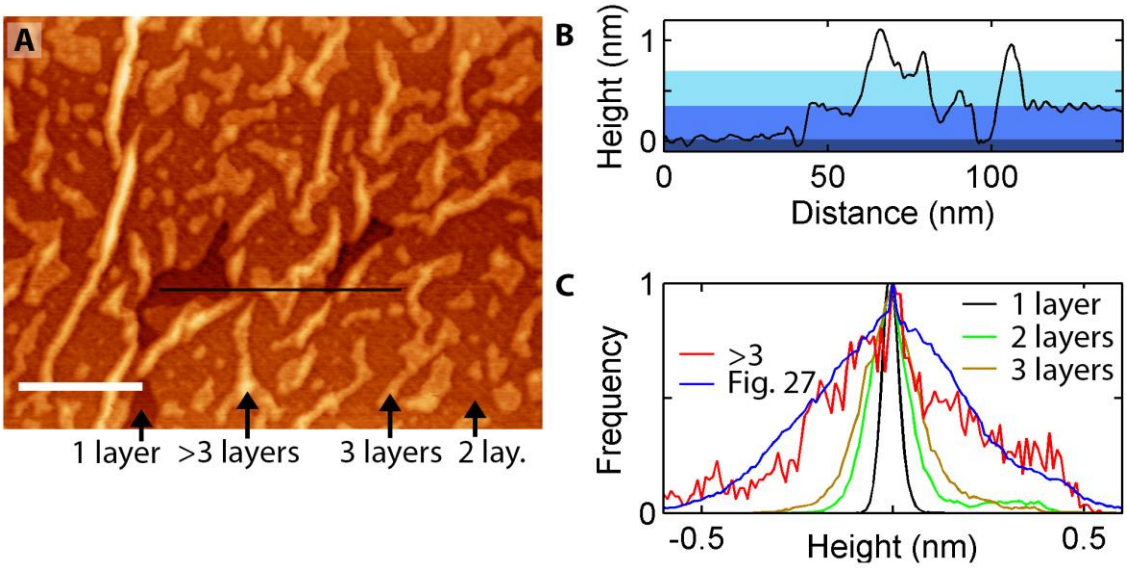

Figure 27: A) TTC on G/mica. Lamellar rows run continuously across the graphene and across step edges arising from different numbers of water layers trapped at the graphene/mica interface. B) Height profile across line marked in A, showing step heights across water layers. C) Histogram of heights for different number of water layers trapped at the G/mica interface indicating an increasing roughness for a higher number of trapped water layers.

Following He et.al. [90] we identify the lowest contrast level in Figure 27A as a single trapped water layer. The step heights between the plateaus 1-2 and 2-3 are extracted from line profiles (such as shown in Figure 27B) and are 0.36±0.03 nm,

0.42±0.03 nm, respectively, in good agreement with reported values which range from 0.35 nm to 0.42 nm [89–92]. In common with previous work the roughness increases as the number of trapped water layers increases. Figure 27C shows a histogram of heights and we find a roughness value of 0.05 nm (taken as the full width half-maximum) for a single water layer which increases to 0.10 nm (0.12nm) for two (three) water layers. A big increase in roughness to ~0.40 nm occurs where the number of trapped layers is greater than three. This roughness value is comparable with the layer height indicating, as suggested in previous studies [89,90], that the water is not ice-like at these thicknesses.

The lamellar structure as on G/BN runs continuously across step edges introduced by the layered nature of the trapped water and is be resolved in Figure 27A as diagonal lines separated by 5.8 nm running across the entire image. This is shown more clearly in the following Figure 28.

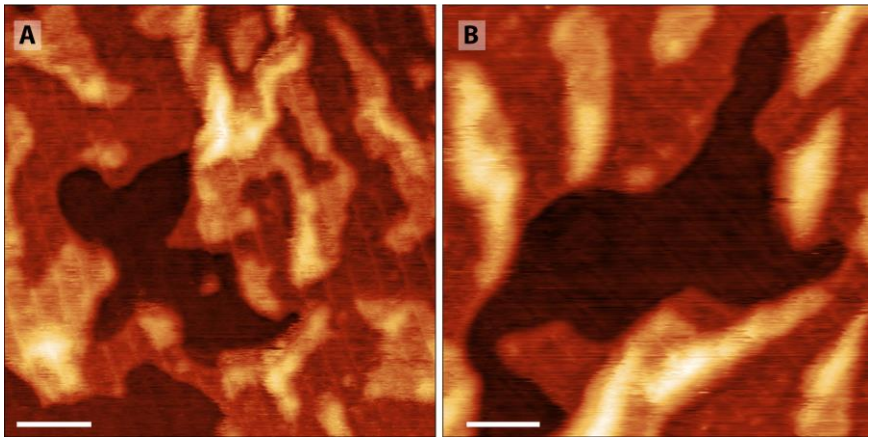

Figure 28: TTC on G/mica showing that the lamellar rows run continuously over terrace steps of height ~0.3 - 0.4nm. Scale bars: 18 nm in A, 15 nm in B. B is a zoomed area of the image in the previous Figure.

Figure 29 shows STM images of TTC adsorbed on an area with more than 3 layers of water at the graphene/mica interface. The lamellar structure is visible, but in addition the roughness, apparent in the background contrast variation, is anisotropic; many of the brighter regions have an elliptical shape with the long axis aligned in a fixed orientation which is perpendicular to the lamellar rows. The molecular structure within the lamellar rows may also be resolved. The anisotropy is also clear in the two-dimensional Fourier transform (FT) of the STM image, see Figure 29 B,

which shows a series of spots arising from the periodic lamellar rows (a diffraction spot due to the packing along the rows is also resolved at higher wavevector and is marked by arrows) superposed on an elliptical central spot. This ellipticity confirms the anisotropic nature of the background fluctuations of the surface. In particular, non-periodic fluctuations with characteristic length scales which are smaller than the molecular length are present parallel to the lamellar rows, but strongly suppressed in the perpendicular direction. Importantly, this anisotropy indicates that the supramolecular structure on areas with more than three water layers under the graphene is not simply a periodic arrangement overlaid onto the surface, but a structure that modifies graphene morphology.

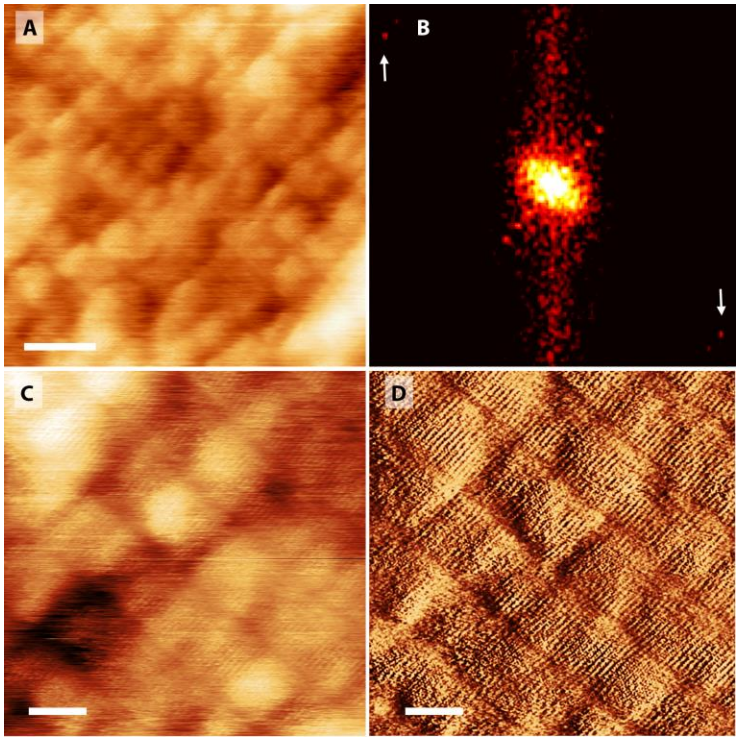

Figure 29: TTC on G/mica. Strong anisotropy of the shape of trapped water is apparent in areas where more than three layers of water are trapped. Scale bar: 10 nm in A, 5 nm in C and D. B) Fourier transform of image showing an elliptical central spot indicating deformation of underlying graphene; the molecular structure along the lamellae gives rise to the spots identified by arrows. D) Differential image of C showing the expected molecular arrangement within the lamellar rows. The scanning parameters were (-1 V, 0.15 nA).

Figure 30 shows a comparison of the variation of heights across the lamellar rows for TTC adsorbed on different substrates. The height variation of TTC on G/hBN is very low (< 0.03 nm). On G/mica with 1-3 trapped water layers the periodic structure is larger, but still comparable with the background roughness ~0.05 nm. However, when adsorbed on regions where there are > 3 trapped water layers the height variation shows a clear periodicity with a peak-to-peak height of 0.20 – 0.25 nm; these changes indicate that the underlying graphene substrate is deformable in regions where there are multiple trapped water layers, and adopts a corrugated conformation, which is further evidence that the water is not ice-like at these water thicknesses and the surface is responsive.

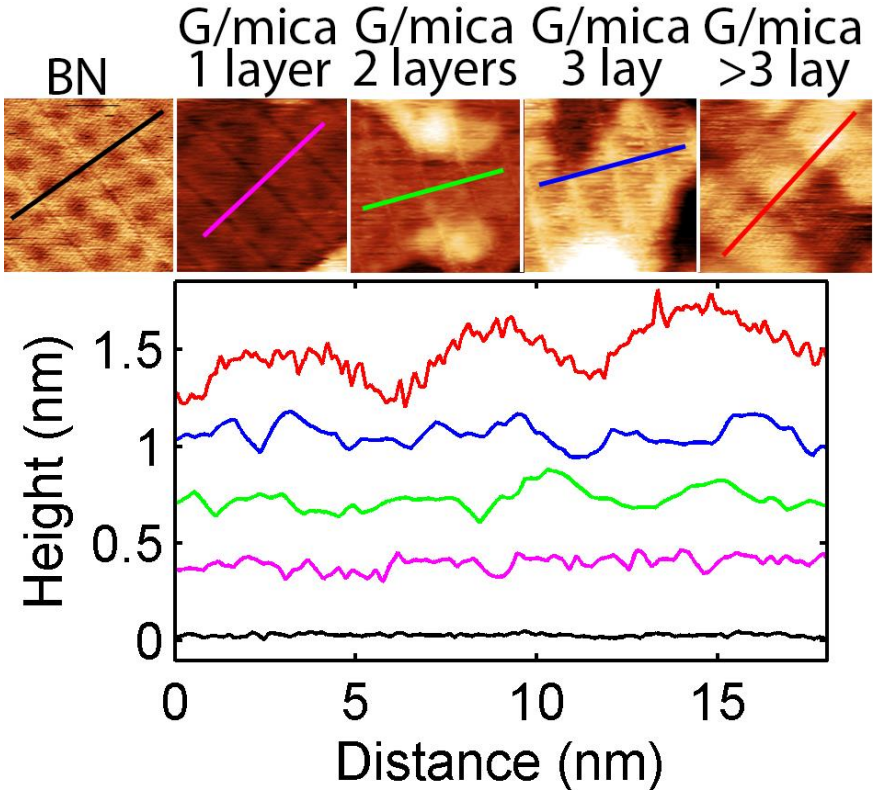

Figure 30: Comparison of the variation of heights across the lamellar rows for TTC adsorbed on different substrates (extracted from images in prefious images). For TTC on G/BN and G/mica with 1-3 water layers, the corrugation amplitude is below 0.1 nm. A larger, and more regular corrugation is found for > 3 layers.

4.2 Energetics of alkane adsorption on curved graphene

In the following it is shown that the curvature of the surface results in an overall reduction in the total energy by increasing the interaction energy between the alkane chain and graphene at the expense of bending energies of the alkane chain and the graphene. As discussed above and in chapter 2.2.2, the carbon atoms in the alkane chain cannot all sit above their preferred adsorption sites on the graphene if the surface is flat. However, the preferred registry can be partially recovered through the introduction of curvature. Here we use an analytical model, complemented by molecular dynamics simulations, to show that adsorbate-induced curvature accounts for our experimental observations. I developed the analytical model together with Peter Beton and the molecular dynamic simulations were done by Matteo Baldoni and Elena Bichoutskaia.

Figure 31 shows the elements of the model. We consider the lattice constant of graphene to be, a, and the separation of a pair of carbon atoms in the alkane chain to be $a + \delta a$, see Figure 31 A. The total length of the chain is equal to $d = N\,a$ where N is the number of carbon pairs, $N = 22$ for TTC . The preferred adsorption site for each -CH_2- group is in alignment with the centre of a hexagon in the underlying graphene, which corresponds to x = 0 in the schematic in Figure 31 B. At position s along the alkane chain a given group is displaced out of registry by Δl, see Figure 31 C.

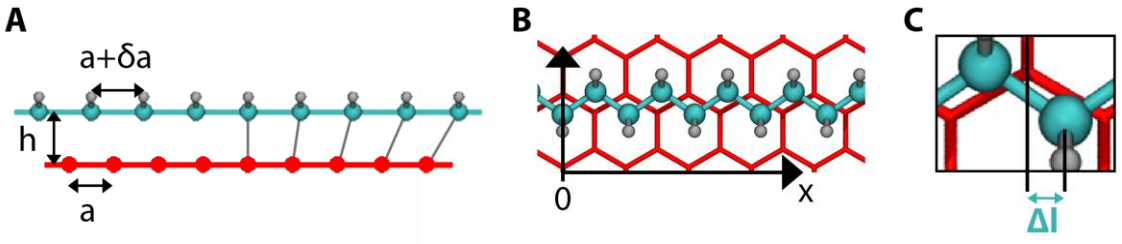

Figure 31: Schematics of a n-alkane adsorbed on G. A) Side-view. The atom separation is a+δa in the alkane and a in the graphene. The distance is h. The difference in periods leads to a variation in local registry. B) Top view and zoom (C). The -CH2- group at s=0 is positioned at the preferred adsorption site. Due to the mismatch in separation of carbon atoms in the chain and the graphene the -CH2- groups along s are offset relative to their preferred adsorption site by an amount Δl.

Consider the carbon in the preferred adsorption site at x=0 such as in Figure 31 B. Due to the mismatch in carbon separation the neighbouring atom are not in their preferred adsorption site, but the registry is restored after m atom pairs, that is after a distance $R_m = a\,m$,

$$m\,(a + \delta a) = (m + 1)a$$

Rearranging gives

$$m = \frac{a}{\delta a} \rightarrow R_m = \frac{a^2}{\delta a} \tag{47}$$

which is the moiré length associated with the mismatch between the alkane and graphene repeat lengths.

We assume that the binding energy of a given carbon pair is equal to $-V_0 \cos(2\pi x/a)$ which is the simplest form of a periodic potential with the given periodicity. We can then calculate the total binding energy for a chain on flat graphene, assuming that the carbon pair at the centre of the adsorbed chain is in phase with the graphene lattice,

$$E = -V_0 \sum_{n=-N/2}^{n=N/2} \cos\left(2\pi \frac{n\delta \mathrm{a}}{a}\right) \tag{48}$$

which can be re-written as an integral,

$$E = -\frac{V_0}{a} \int_{-d/2}^{d/2} \cos\left(2\pi \frac{\mathrm{x}\delta \mathrm{a}}{a^2}\right) dx \tag{49}$$

We can also consider the energy for a chain in which the centre is exactly out of phase with the graphene lattice. Here, we have an extra phase of π, resulting in

$$E = -\frac{V_0}{a} \int_{-d/2}^{d/2} \cos\left(2\pi \frac{\mathrm{x}}{R_m} + \pi\right) dx = \frac{V_0}{a} \int_{-d/2}^{d/2} \cos\left(2\pi \frac{\mathrm{x}}{R_m}\right) dx \tag{50}$$

which is equivalent to the above energy apart from the reversal of sign. The notation can be shortened to E_+ and E_- to represent the energies of the in-phase and out-of-

phase solutions. Note that these energies are always the maxima or minima of energies, so that no other phase relationships have to be considered. In this notation,

$$E_{\pm} = \mp\frac{V_0}{a}\int_{-d/2}^{d/2}\cos\left(2\pi\frac{\mathrm{x}}{R_m}\right)dx \tag{51}$$

If we introduce curvature such as in Figure 32 A the relative displacement may be reduced due to the difference in radius of curvature of the graphene, R, and the adsorbed molecule (R and $R+h$). A phase difference of $(n\delta a)/a$ on a flat surface is reduced by (nh/R) if a curvature is introduced, and assuming a constant radius of curvature R, see Figure 32 B. Including these effects gives a modified energy,

$$\begin{aligned} E_{\pm} &= \mp V_0\sum_{n=-N/2}^{n=N/2}\cos\left(2\pi\left(\frac{n\delta\mathrm{a}}{a}-\frac{nh}{R}\right)\right) \\ &= \mp\frac{V_0}{a}\int_{-d/2}^{d/2}\cos\left(2\pi x\left(\frac{1}{R_m}-\frac{h}{\mathrm{a}R}\right)\right)dx \end{aligned} \tag{52}$$

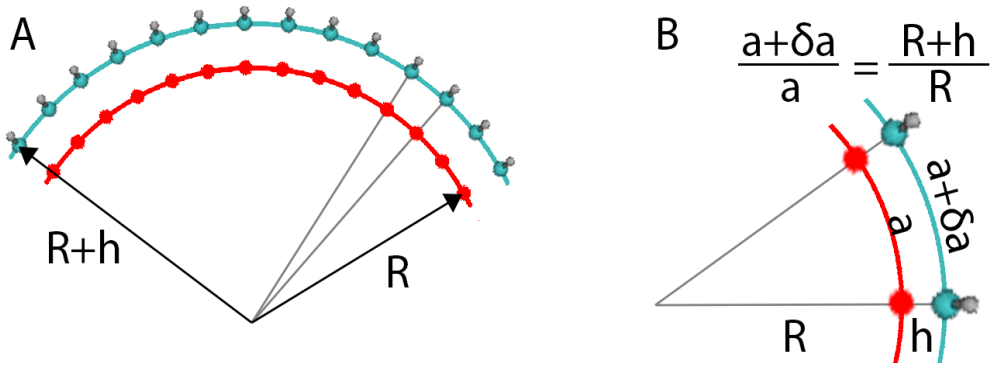

Figure 32: Schematic of n-alkane on curved G. A) The variation of registry can be modified if the TTC/G surface is curved, and completely eliminated if the ratios of the arc lengths (periods) is equal to the ratio of radii of curvature, i.e. $(a+\delta a)/a=(R+h)/R$, or $R=R_c=ha/\delta a$. B) Zoomed part of A, for geometrical argument $(a+\delta a)/a=(R+h)/R$.

We define R_{eff},

$$\frac{1}{R_{\text{eff}}} = \frac{1}{R_m} - \frac{h}{\text{a}R} = \frac{\delta\text{a}}{a^2} - \frac{h}{\text{a}R} \tag{53}$$

as the effective moiré length scale at which the registry on a curved surface is restored. Using the notation with R_{eff}, and on performing the integration, we get

$$E_{\pm} = \mp \frac{V_0}{\pi a} R_{\text{eff}} \sin\left(\frac{\pi d}{R_{\text{eff}}}\right) \tag{54}$$

which is an expression that relates the alkane-graphene binding energy to the radius of curvature. The preferred registry is restored at curvature at which the energy is minimised. To find the according radius of curvature we derive E_+ after x and set to zero,

$$\frac{\partial E_+}{\partial x} = 0 = -\frac{V_0}{\pi a} \sin\left(\frac{\pi d}{R_{\text{eff}}}\right) + \frac{V_0 d}{a R_{\text{eff}}} \cos\left(\frac{\pi d}{R_{\text{eff}}}\right) \tag{55}$$

which is satisfied if $1/R_{\text{eff}} = 0$, which gives the minimum energy (with sin expanded to first order),

$$E_{x,min} = -\frac{V_0}{\pi a} R_{\text{eff}} \frac{\pi d}{R_{\text{eff}}} = V_0 \frac{d}{a} = -NV_0 \tag{56}$$

for a radius of curvature,

$$\frac{1}{R_{\text{eff}}} = 0 \rightarrow R = R_c = \frac{ha}{\delta\text{a}} \tag{57}$$

which we call the critical radius R_c, at which the registry for all atoms along the molecule is restored.

Figure 33 shows a graph of $E_{\pm}$, showing the energy gain of the alkane-graphene system due to binding. The energy will be equal to whichever E_+ or E_- is the lower; thus the configuration would be expected to switch from having the centre of the alkane in phase with the graphene to being out of phase when $E_+ = E_-$.

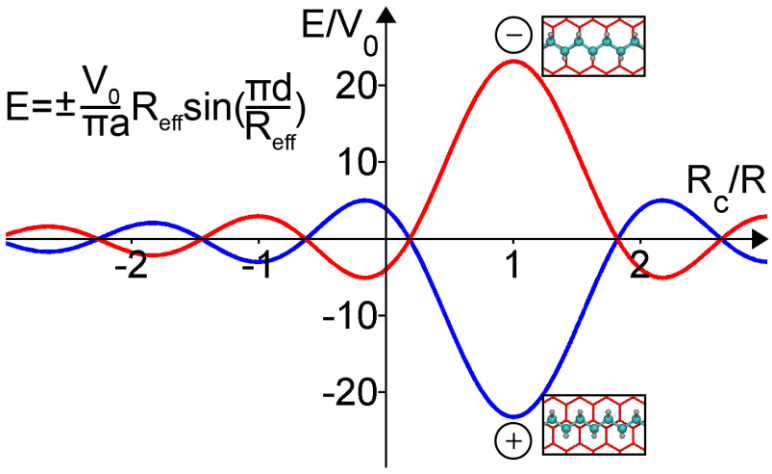

Figure 33: In-phase (blue) and out-of-phase (red) curvature dependent moiré variation of binding energy with respect to a surface with a radius of curvature R. The radius at which the registry is restored is R_c and the depth of the minimum energy is $-NV_0$ with $N = 22$ for TTC.

The total adsorption energy involves the binding energy (equation (54), Figure 33) and another term due to an increase in atom-surface separation for positive curvature, schematically shown in Figure 34 A.

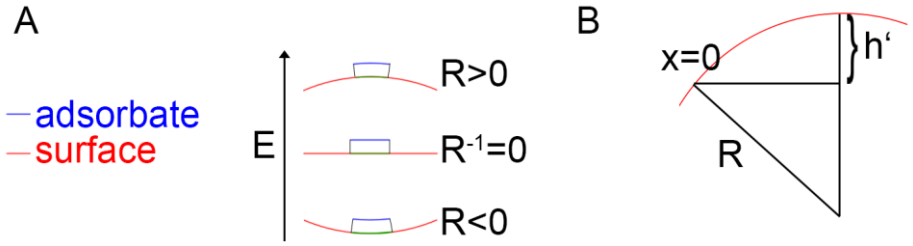

Figure 34: A) Schematic of an adsorbed particle on a surface. The section marked in green, and thereby the energy, at which the particle is in a given distance interval to the surface varies with R. B) Schematic for argument in the text considering geometry of a circle.

To find an expression for this change in adsorption energy, we consider an atom placed a height h above a surface interacting through potentials of the form B/r^m. Assuming that we have a density of n atoms per unit area in the surface the potential arising from an element dA in the surface is $C/r^m\ dA$, where $C = nB$. Summing over the potentials arising from different sites on the surface gives for a planar surface

$$V_{plane} = C \int dx \int dy \frac{1}{(x^2 + y^2 + h^2)^{m/2}} \tag{58}$$

For a cylindrically curved surface (cylinder axis parallel to y) the term for r^2 is modified to

$$r^2 = x^2 + y^2 + \left(h + R - (R^2 - x^2)^{1/2}\right)^2 \tag{59}$$

which effectively is a change in h by the distance h' marked in Figure 34 B. We may approximate for R≫x, h,

$$r^2 \approx x^2 + y^2 + \left(h + \frac{x^2}{2R}\right)^2 \approx x^2\left(1 + \frac{h}{R}\right) + y^2 + h^2 \tag{60}$$

Accordingly we can rewrite equation (58) for a cylinder

$$V_{cylinder} = C \int dx \int dy \frac{1}{(x^2(1 + h/R) + y^2 + h^2)^{m/2}} \tag{61}$$

which simplifies after a change of variables $x' = (1 + h/R)^2 x$, to

$$\begin{aligned} V_{cylinder} &= C\left(1 + \frac{h}{R}\right)^{-\frac{1}{2}} \int dx' \int dy \frac{1}{\left(x'^2 + y^2 + h^2\right)^{m/2}} \\ &\approx \left(1 + \frac{h}{2R}\right) V_{plane} \end{aligned} \tag{62}$$

which is an expression for the curvature induced change in adsorption energy. The total adsorption energy is therefore the binding energy, equation (54), modified by a factor according to equation (62),

$$E_{\pm} = \mp \frac{V_0}{\pi a} R_{\text{eff}} \sin\left(\frac{\pi d}{R_{\text{eff}}}\right) + \frac{h}{2R} E_A \tag{63}$$

where E_A is the adsorption energy in the flat configuration. E_A = -3.33 eV simulating TTC on flat graphene. $V_0 = 6$ meV has been extracted by simulating the shorter alkane chain C_8H_{18}, whose registry can be (approximately) in-phase or out-of-phase with the preferred registry along the entire chain on flat graphene. By displacing the chain with respect to the graphene lattice, as shown in Figure 35, and comparing the total

energies in-phase and out-of-phase, V_0 is the change of the total energy divided by the number of carbon pairs (4 for C_8H_{18}). Matteo Baldoni and Elena Bichoutskaia have extracted these values from molecular dynamics simulations; for details see Supporting Information of [94].

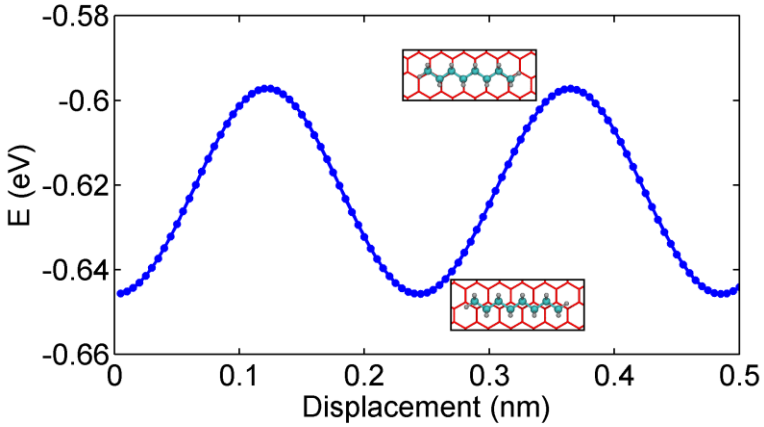

Figure 35: Energy/displacement diagram of C_8H_{18} on graphene. The energy is minimized when the alkane lies in-phase with the preferred registry (bottom inset), and increases when displaced into the out-of-phase registry (top inset).

Using further molecular dynamics simulations a TTC molecule adsorbed on a frozen cylindrical graphene surface was optimised (a zig-zag carbon nanotube (CNT) with an artificially large radius of curvature). We extracted the dependence on curvature, R^{-1}, of the adsorption energy and the bending energy of the adsorbed alkane. These calculations confirm that the alkane is adsorbed with the zig-zag chain locally parallel to the graphene at a height, h = 0.38 nm, which is near-independent of curvature. Figure 36 A shows a comparison of the theoretical adsorption energy, with the numerically-calculated values (blue points). Despite the simplicity of the model (solid, black line), the principal physical results are captured correctly. In particular we observe an energy minimum for $R \approx R_c$ corresponding to the matching condition discussed above, combined with a background linear slope (as in equation (62)). The cusp-like behaviour, at the curvatures where the red and blue curves in Figure 33 intersect, is due to the lowest energy configuration, which always results from numerical optimization, undergoing a transition from an in-phase (+) to an out-of-phase (-) solution. This comparison confirms that the simple, analytic form (equation (63)) accounts for the calculated variation of adsorption energy, and that no other

deformation processes, such as bond angle distortion and other elastic effects, play a significant role.

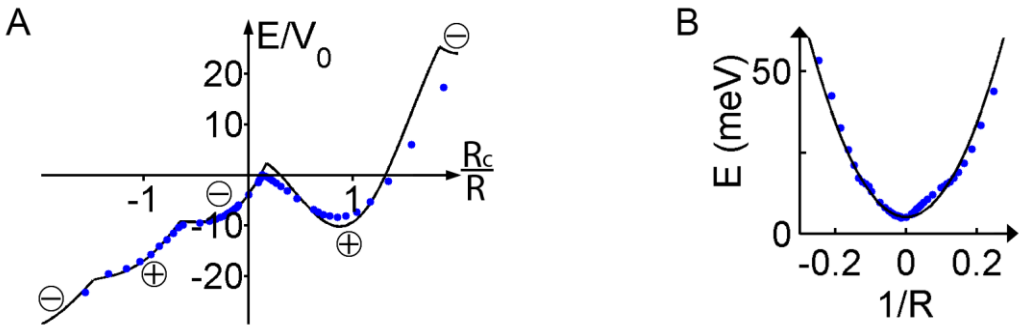

Figure 36: A) Adsorption energy of TTC on graphene (solid line) and numerical calculations (blue dots) for a curved graphene surface indicating that the curvature-related moiré effect successfully accounts for the calculated behavior. B) Bending energy of the adsorbed TTC versus inverse radius of curvature.

Additional terms to consider are the bending energies of the graphene and the alkane. For an isotropic graphene monolayer the energy cost of bending is given by $E = \kappa/2 \int R^{-2} dA$ where κ is the bending coefficient, which has been estimated [95,96] to be κ = 0.19 nN nm. The energy cost of bending the alkane is given by $E_B = \kappa_B d/2R^2$, where we treat the molecule as an elastic rod with bending coefficient κ_B. To find κ_B, we consider the combined adsorption and bending energy (E_{tot}) of alkane chains on CNTs. It was evaluated as $E_{\text{tot}} = E(\text{Alk@CNT}) - E(\text{CNT}) - E(\text{Alk})$, where E(Alk@CNT), E(CNT) and E(Alk) are the total electronic energies of the alkane-CNT complex, CNT and alkane chain, respectively. The bending energy (E_{ben}) for the alkane chain is evaluated as $E_{\text{ben}} = E(\text{Alk})\text{@CNT} - E(\text{Alk})$, where E(Alk)@CNT is the total electronic energy of the chain in the geometry of the complex; the bending energy is plotted in Figure 36 B. We find the expected parabolic dependence on R^{-1}, and determine the alkane bending coefficient by fitting a parabola to be κ_B = 0.04 nNnm^2.

4.3 Extension to variable curvature

Our experimental configuration differs from the simple scenario in which the alkane lies on a surface with a constant curvature since the average curvature over the surface in the experiment is zero, i.e. it is macroscopically flat with regions of positive and negative curvature. This can be taken into account by formulating the expressions for the energy contributions (equations (52) and (62)) as a path integral,

$$E = -\int_{-\frac{d}{2}}^{\frac{d}{2}} \frac{V_0}{a}\cos\left(2\pi\left(\frac{\delta a}{a^2}s - \frac{h}{a}\theta\right)\right) - E_A\left(1 - \frac{h}{2}\frac{d\theta}{ds}\right) + \frac{\kappa_B}{2}\left(\frac{d\theta}{ds}\right)^2 + \frac{\kappa a\sqrt{3}}{2}\left(\frac{d\theta}{ds}\right)^2 ds \tag{64}$$

in which s is the path along the graphene and $\theta(s)$ is the angle between the x axis and the local tangent of the graphene, and the curvature is $d\theta/ds = 1/R$. In the equation we include the factor $a\sqrt{3}$, the separation of molecules along the lamellar rows, in the term for the graphene bending energy, since we consider the energy per molecule on a corrugated surface.

To determine the stability of a surface against curvature we consider the energy change arising from a variation in $\theta(s)$ which is periodic with period d, that is

$$\theta(s) = \theta_0 \sin\left(\frac{2\pi}{d}s\right) \tag{65}$$

with which the energy due to bending, equation (64), can be determined. We consider a surface fully covered by molecules, and hence the term $\int E_A\left(1 - \frac{h}{2}\frac{d\theta}{ds}\right)ds$ must be dropped because it refers to the energy arising from curvature-induced changes arising from the effective binding energy of a single molecule. We define $f = 2\pi h\theta_0/a$ and $R_m = a^2/\delta a$ for short notation, and consider small amplitude variations (small θ_0, small f),

$$E = -\int_{-\frac{d}{2}}^{\frac{d}{2}} \frac{V_0}{a}\cos\left(2\pi\left(\frac{\delta \mathrm{a}}{\mathrm{a}}s - \frac{h}{a}\theta_0 \sin\left(\frac{2\pi}{d}s\right)\right)\right) + \left(\frac{\kappa_B + \kappa a\sqrt{3}}{2}\right)\left(\frac{2\pi\theta_0}{d}\cos\left(\frac{2\pi}{d}s\right)\right)^2 ds$$

$$= -\int_{-\frac{d}{2}}^{\frac{d}{2}} \frac{V_0}{a}\cos\left(\frac{2\pi}{R_m}s - f\sin\left(\frac{2\pi}{d}s\right)\right) + \left(\frac{\kappa_B + \kappa a\sqrt{3}}{2}\right)\left(f\frac{a}{dh}\cos\left(\frac{2\pi}{d}s\right)\right)^2 ds$$

$$= -\frac{V_0}{a}\int_{-\frac{d}{2}}^{\frac{d}{2}} \cos\left(\frac{2\pi}{R_m}s\right) + f\sin\left(\frac{2\pi}{R_m}s\right)\sin\left(\frac{2\pi}{d}s\right) - \frac{1}{2}f^2\left(\sin\left(\frac{2\pi}{d}s\right)^2\cos\left(\frac{2\pi}{R_m}s\right)\right)$$

$$+ f^2\frac{a^2}{d^2h^2}\left(\frac{\kappa_B + \kappa a\sqrt{3}}{2}\right)\cos\left(\frac{2\pi}{d}s\right)^2 ds$$

which can be solved without further expansions and simplified to,

$$E = -\frac{V_0 R_m}{a\pi}\sin\left(\frac{\pi d}{R_m}\right)\left(1 + f\frac{R_m d}{R_m^2 - d^2} - f^2\left(\frac{R_m^2}{4R_m^2 - d^2} + \frac{\pi a^3}{4h^2 d}\frac{\kappa_B + \kappa a\sqrt{3}}{V_0 R_m \sin\left(\frac{\pi d}{R_m}\right)}\right)\right)$$

We find f for which this energy is minimised, $dE/df = 0$,

$$\frac{4R_m^2 - d^2}{R_m^2 - d^2}\frac{d}{2R_m} = f\left(1 + \frac{4R_m^2 - d^2}{R_m^2}\frac{\pi a^3}{4h^2 d}\frac{\kappa_B + \kappa a\sqrt{3}}{V_0 R_m \sin\left(\frac{\pi d}{R_m}\right)}\right) \equiv f\frac{1}{\beta} \qquad (66)$$

which implies, since $f = 2\pi h\theta_0/a$, that the energy dependence has a minimum at

$$\theta_0 = \frac{a}{4\pi h}\frac{4R_m^2 - d^2}{R_m^2 - d^2}\frac{d}{R_m}\beta \neq 0 \qquad (67)$$

confirming that spontaneous curvature due to molecular adsorption is expected.

Neglecting the contributions from the bending energy terms proportional to κ and κ_B, results in a predicted peak-to-peak height variation

$$A = \frac{\theta_0 d}{\pi} = \frac{a}{4\pi^2 h}\frac{4R_m^2 - d^2}{R_m^2 - d^2}\frac{d^2}{R_m} = \frac{ad}{4\pi^2 h}\frac{4-\gamma^2}{1-\gamma^2}\gamma \qquad (68)$$

Inclusion of the intrinsic bending energies of the graphene and the molecule leads to a reduction in amplitude, A, by a factor β.

Experimentally we find A = 0.22 ± 0.02 nm which, using the values of κ_m and κ_B discussed above, implies γ = 0.68 ± 0.03 and β = 0.54. This in turn implies that $R_m \approx 3d/2$, and recalling that $R_m = a^2/\delta a$, gives $\delta a \sim 2a/3N \sim 0.03a \approx 7$ pm. This corresponds to a spacing of carbon pairs in the alkane of a_{alk} = 0.253 nm. This value is slightly larger than assumed previously [47,87,88] (0.251 nm), but is close to published values for carbon atoms in propane, 0.2536 nm [97]. Note that these differences, which are in the picometre scale, are significant since the amplitude, A, is proportional to the difference between periodicities between graphite and the alkane. This agreement supports our interpretation of adsorbate-induced curvature of graphene.

For graphene adhering to a solid substrate surface the bending coefficient κ should be replaced by that of the underlying substrate, which would be orders of magnitude higher. Consequently $\beta \rightarrow 0$, and no spontaneous curvature would be expected; this corresponds to the case of hBN. The reduction of energy and the corresponding corrugation of the surface is only observed parallel to the alkanes implying that fluctuations around the corrugated configuration are suppressed relative to fluctuations perpendicular to the alkanes. We attribute the observation of anisotropic height fluctuations in Figure 29 to this effect. We also note that recent measurements have shown that the bending stiffness of bilayer graphene is significantly greater than that of monolayer [98]. It is possible that this is also related to the relative displacement of carbon atoms in one layer from their preferred adsorption site on a neighbouring layer.

4.4 Conclusion

In summary, this work shows that the adsorption of supramolecular structures can induce elastic deformation in transferred graphene. In particular, this effect is shown through the adsorption of alkanes on graphene deposited onto mica in the presence of trapped water layers at the graphene/mica interface. Alkanes are present as atmospheric contaminants in many environments, making this finding relevant to applications in microfluidics, electronics, composite materials, and nanomechanical systems, both in terms of gaining understanding of device operation, and also for new modalities, for example related to control of mechanical properties. Furthermore, this work provides an example of molecular self-assembly on a soft support. The property of mechanical deformability of such an 'active' substrate in response to adsorbates reminds of interfaces in biological systems, and this work motivates further studies of adsorption in such systems and on soft supports.

5 Quantum thermopower in MoS_2

The electron transport through a 2D material in the cross-plane direction is on the nanometre-scale and is therefore quantised. It can be described as a scattering process, in which incident electrons are either transmitted or reflected, which is formally described by the Landauer approach for coherent transport, in which the conductance G is proportional to the transmittance, $G = T\,e^2/h$. In this respect, 2D materials are reminiscent of molecules, in which electron transport can be understood in the same way. This similarity implies that electrical or thermal phenomena that have been observed in individual molecules connected to electrodes are likely to occur in the cross-plane direction of 2D materials. An example for such a phenomenon is quantum thermoelectricity, which is of interest because of the strong demand for cost-effective, pollution-free forms of energy conversion. This motivates to study the effects of a thermal gradient on 2D materials.

Additional motivation to investigate the thermoelectricity of 2D materials in the cross-plane direction stems from equation (27), derived in chapter 2.3.3,

$$q_{max} = \frac{1}{l}\left(\frac{S^2 T_C^2}{2\rho} - k(T_H - T_C)\right) \tag{27}$$

which states that the maximum heat-flux pumping capability of a thermoelectric element inversely proportional to the device thickness. This manifests in the q_{max} values that have been found in thermoelectric materials. Commercial bulk thermoelectric materials typically have q_{max} values (at $T_H - T_C = 0\ K$) in the range $\sim 5 - 10$ W/cm^2 with thicknesses above 100 µm. Conversely thin-film thermoelectrics with thicknesses of ~5 µm [99] can reach values closer to 100 W/cm^2, and a device with q_{max} =250 W/cm^2 with $l = 8.1$ µm has recently been demonstrated [100]. Since 2D crystals represent a further scaling-down step higher q_{max} values can be anticipated.

Among 2D materials, MoS_2 is particularly interesting for thermoelectric applications because monolayer MoS_2 has a large in-plane thermopower, which has been reported to be between 200 and 30 000 µV/K [101–105]. Furthermore, electric devices based on thin layers of MoS_2 have previously shown excellent performance as, for example, field effect transistors [106], diodes [107], photodetectors [108] and solar cells [109].

In the following, the first measurement of the cross-plane thermopower in a 2D material is discussed. We study the thermoelectric properties of single- and few-layer MoS_2 and find that the cross-plane thermopower in MoS_2 depends on the number of layers, with values ranging from -22 ± 1 μV/K for a monolayer to -330 ± 70 μV/K at 6 layers and the conductance per unit area decreases exponentially. These thickness-dependencies indicate the quantum nature of the phenomena. Besides, we find a heat-flux pumping capability of 640 W/cm^2 for bilayer MoS_2, exceeding previously reported values. The thermopower and q_{max} values imply high potential for 2D materials in thermoelectric applications and our results encourage future work on cross-plane thermoelectricity in these materials.

5.1 Thermopower measurement by conductive AFM

Thin flakes of MoS_2 were prepared by exfoliation of bulk crystals, acquired from Moly Hill mine, Quebec, Canada, and deposited onto a stamp, as described in chapter 3.2. The flakes were then transferred onto a 295 nm SiO_2/Si wafer with a layer of previously evaporated Au/Ti (15 nm + 5 nm). The Au layer serves as a bottom contact for the c-AFM experiment. We chose this substrate, as opposed to bulk Au, because Au with a thickness of 15 nm exhibits both, high transparency and high conductivity. The transparency ensures the visibility of thin exfoliated layers. Following the transfer, the samples were annealed in vacuum (10^{-2} mbar) at 120 °C for 2 h to improve the electrical contact at the MoS_2/Au interface. Afterwards the samples were characterised in ambient conditions at room temperature.

To determine the flake thickness Patricia Gant conducted micro-reflectance spectroscopy, in which a light source is focussed on the sample (spot size 2 µm) and the intensity and spectral distribution of the reflected light is measured. Such spectra exhibit distinctive peaks at wavelengths which are preferably absorbed. For MoS_2, the peaks correspond to excitons, whose energy changes with the number of layers, allowing a facile and certain determination of the flake thickness, see Figure 37.

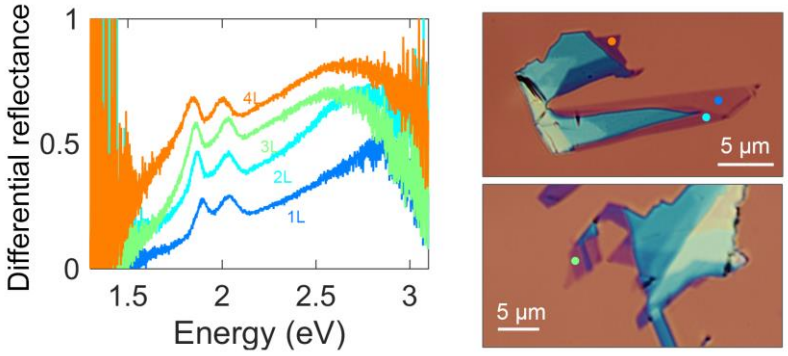

Figure 37: Differential reflectance spectra of MoS_2 with 1 to 4 layers. The incident light was pointed at the marked positions. The flake thickness can be determined from the peak positions and the total reflectance, as in Frisenda et al. [110].

Additionally, the flake thickness was measured by AFM in tapping mode. Figure 38 A shows an AFM image of a monolayer region, as determined by micro-reflectance spectroscopy, alongside with a line profile. The apparent height is 2.3 nm which differs from the MoS_2 interlayer spacing by ~1.7 nm. this discrepancy is a known phenomenon in the height determination of 2D materials which is typically attributed to tip-surface interactions, image feedback settings and surface chemistry [111] or to adsorbates on or under the MoS_2. For higher layer-numbers we find the thicknesses shown in Figure 38 C. The increase in thickness per layer (>1) is 0.65 nm, equal to the MoS_2 interlayer spacing [8], as expected.

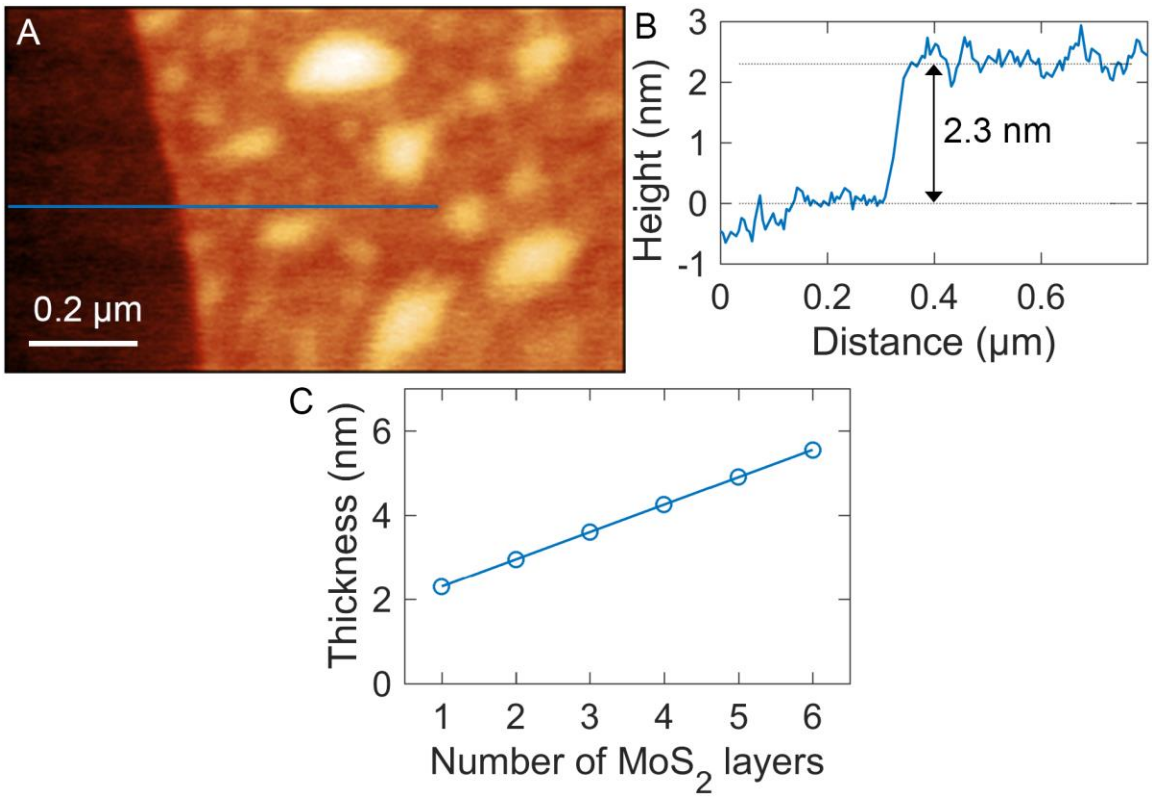

Figure 38: A) AFM image of the edge of monolayer MoS_2 on $Au/SiO_2/Si$. B) Profile along the line indicated in A, showing an apparent height of 2.3 nm. C) Number of layer dependence of the apparent MoS_2 thickness. The increase in thickness per layer is 0.65 nm.

After the determination of the number of layers N in a given region, the thermopower was measured as described in chapter 3.2.. In short, the tip is put into light contact (~ 30 nN) with the sample and held still by manually adjusting the z-

axis. A Peltier element, mounted in the AFM setup, heats the sample from below generating a temperature gradient ΔT across the MoS_2. A voltage is applied between the tip and the sample and the current is measured. The *I-V* characteristics are offset by a through the Seebeck effect generated voltage in the range of 0.1 mV. To precisely determine this voltage, offsets in current and voltage need to be determined. In order to do so, the current flow through the AFM is interrupted and guided through a resistor R which allows a precise zero-calibration of the voltage. The offset in current can be determined in open-circuit conditions. Figure 39 shows a schematic of the instrument and typical *I-V* curves for $N = 1, 2, 3$.

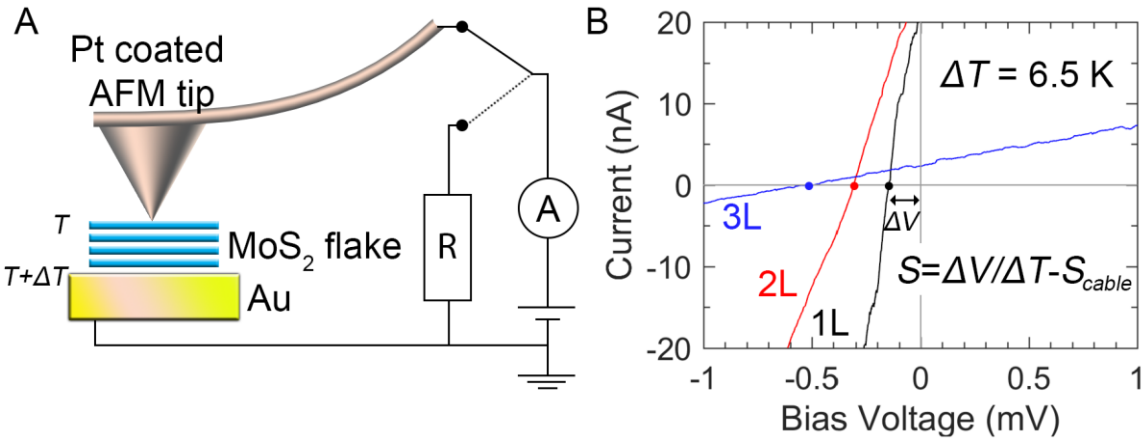

Figure 39: A) Schematic of the c-AFM set-up. MoS_2 is deposited on a Au substrate and contacted with a Pt-coated c-AFM tip. A bias is applied to either the c-AFM to extract I-V characteristics or to a resistor R in order to calibrate the bias voltage. The Au substrate can be heated to establish a temperature difference between tip and substrate ΔT. B) Typical *I-V* characteristics for mono-, double-, and tri-layer MoS_2. The curves show a voltage offset ΔV induced by the thermoelectric effect.

By relating ΔV to S using the heat circuit and consideration described in chapter 3.2, we get one data point for S per *I-V* curve. Besides, we get one data point for the conductance G from each *I-V* curve from the slope. To obtain statistically significant values we record approximately 200 *I-V* curves per approach and approach the tip in at least 5 different areas per N. The measuring procedure at a given area begins at $t = 0$ s, after the erroneous offsets have been determined. The voltage is continuously ramped up and down and the resulting *I-V* curves are saved. The S- and G values of a representative data set for monolayer MoS_2 are shown in Figure 40. In

interval I, from $t = 0$ s to $t = t_1$ the tip approaches from a distance of several hundreds of nanometres until it is in close proximity (several nm) to the sample. The conductance in this time interval is below the signal detection threshold and hence the corresponding C and S values are discarded. At $t = t_1$ the tip jumps into contact and is held still by manually readjusting the force to a constant value of ~30 nN until $t = t_2$. The conductance in this time interval, interval II, is at a constant value which changes slightly with the pressure. Typically, we detect changes in S by 5 % in a random fashion. This, in particular the fact that S does not tend to 0 μV/K, implies that there is no reduction in ΔT with time. After measuring approximately 200 *I-V* curves the tip is retracted at $t = t_2$.

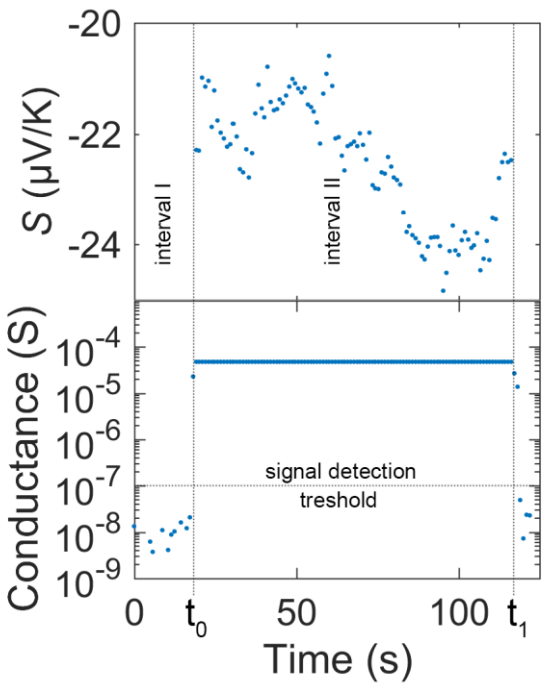

Figure 40: Typical S and conductance values during the recording of a dataset on monolayer MoS_2. The tip is approached in interval I, in electrical contact with the MoS_2 in interval II, and retracted afterwards, while *I-V* curves are continuously measured.

The data can be represented in histograms, see Figure 41 A. We determine S_{1L} = -22 ± 1 μV/K, S_{2L} = -48 ± 2 μV/K, and S_{3L} = -88 ± 1 μV/K for 1L, 2L, and 3L, respectively. We measured flakes with thicknesses up to 6L and the results are shown in a

thermopower *vs.* number of layers-graph, see Figure 41 B. The error bars represent the standard error, i.e. the variance of Gaussian fits to the corresponding peaks in the histogram divided by the square root of the number of measuring points. We find a continuous increase of the absolute value of S up to S_{6L} = -330 ± 70 µV/K, which is one order of magnitude higher than typical quantum thermopower values in the range of 10-40 µV/K which, by this time, have only been reported for molecular junctions [55,64,112,113] and atomic-size contacts [56]. Furthermore, the sign of the thermopower is negative at all thicknesses indicating transport through the conduction band as expected since our material exhibits n-type conduction, which is further discussed in chapter 6.

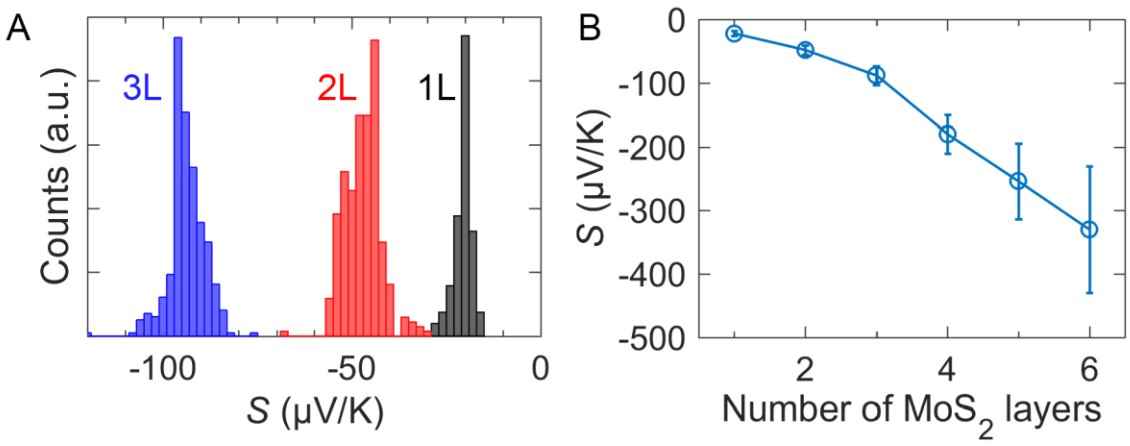

Figure 41: A) Histogram of the thermopower S extracted from hundreds of *I-V* curves acquired at different sample locations, showing distinct peaks for flakes with different number of layers. B) *S* values extracted from histograms (blue circles). The error bars represent the standard error.

Colin Lambert, Hatef Sadeghi, and Sara Sangtarash at the Lancaster University created a density functional theory model to investigate the origin of the thermopower. They first found the optimal ground state crystal structure and then created the Hamiltonian using the SIESTA implementation of density functional theory, and used then the transport simulation tool Gollum to find the transmission T(ε), which is shown in Figure 42 A. The thermopower was calculated from equation 17 for the interval E = [0.1, 0.2] eV. A thermopower vs. number of layers-graph is shown in Figure 42 B in which the error corresponds to the edges of

the energy interval [0.1, 0.2] eV and the value is their average. We find a good agreement with the experimental results in Figure 41 B.

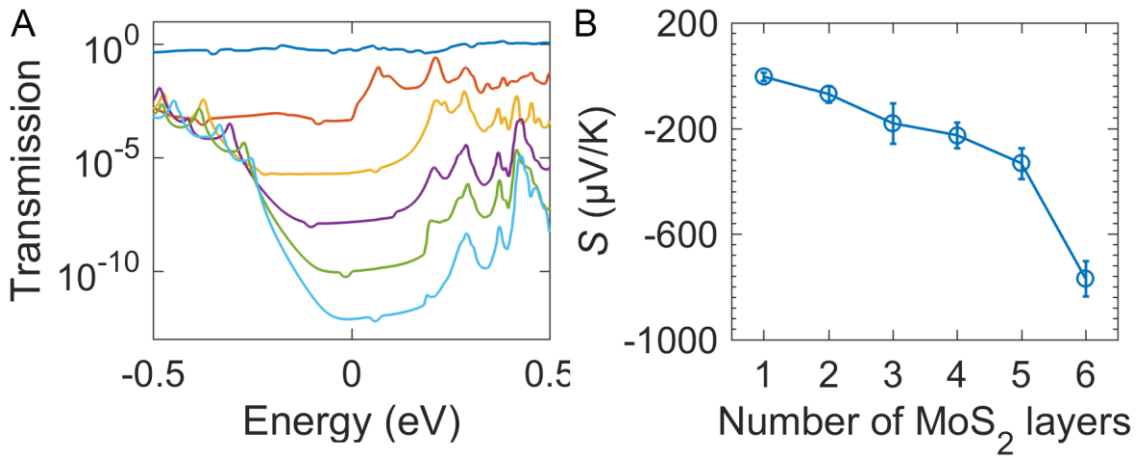

Figure 42: A) Cross-plane thermopower in multilayer MoS_2. B) Room-temperature thermopower for electrons with energy E = [0.1, 0.2] eV vs. the number of MoS_2 layers.

5.2 Maximum heat pumping capacity per unit area

The conductance values extracted from the c-AFM experiment show small variations of about 10 %, depending on the tip shape. To find the heat pumping capacity, i.e. to solve equation (27), the resistivity, $\rho = A/l\ R$, has to be determined. The effective contact area A is a priori unknown but can be determined by an additional experiment. To determine A, we exfoliated MoS_2 flakes onto a Au substrate and evaporated 60 nm of Au through a shadow mask with circular openings 800 nm in diameter, creating a Au/MoS2/Au sandwich structure with a given area, see Figure 43 A and B. We measured the *I-V* characteristics by probing the evaporated Au disks with the c-AFM tip. The thus obtained *I-V* curves are linear for small biases [-1 mV, +1 mV] which allows to extract the zero-bias conductance per unit area. Such as in the c-AFM experiment, the conductance drops exponentially with N, see red crosses in Figure 43 C. By comparing the conductance values obtained in the two experiments we can estimate the effective area of the tip to be 1300 nm^2 which is in good agreement the area corresponding to the manufacturers specifications of the tip radius of 10 nm. The conductance per area values obtained from the c-AFM experiment are plotted in Figure 43 C as blue circles.

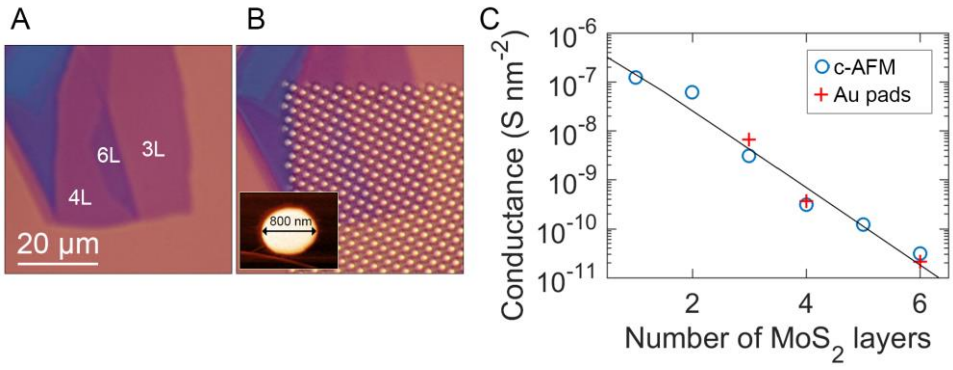

Figure 43: Optical image of a MoS_2 flake on Au before (A) and after (B) deposition of Au disks through a shadow mask. Inset: AFM micrograph of a Au disk. B) Conductance dependence on the number of MoS_2 layers. The red cross signs show the conductance in the Au/MoS_2/Au sandwich structure, the blue circles show the conductance determined in the c-AFM tip/MoS_2/Au experiment assuming an effective tip area of 300 nm^2.

The maximum heat absorbed from the cold side per unit area can now be determined. Equation (27) with $\Delta T = 0$ K and $\rho = A/l\ R$ becomes

$$q_{max} = \frac{1}{2}\frac{S^2\ T_C^2}{RA}$$

where A is the area, R is the resistance, and T_C is the temperature of the cold side, see Figure 44. The highest values are $q_{max} = \sim 270$ W/cm^2 for a monolayer and $q_{max} = \sim 640$ W/cm^2 for a bilayer. The value for bilayer MoS_2 is two orders of magnitude larger than that of commercial bulk thermoelectric materials and comparable to that of recently demonstrated superlattice-based thin-film devices [114].

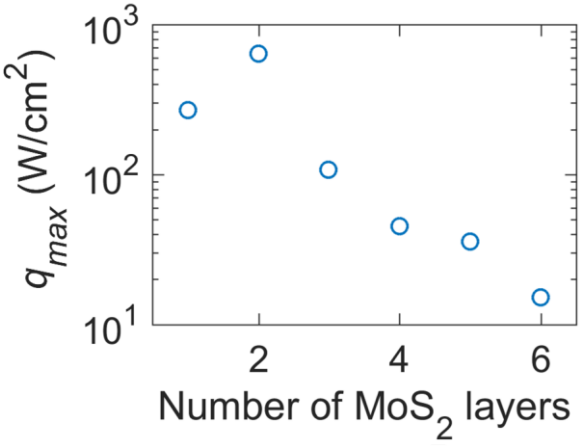

Figure 44: Maximum heat-flux pumping capability $q_{max} = \frac{1}{2}S^2{T_C}^2/RA$ for $\Delta T = 0$, where A is the contact area

Since quantum thermopower has previously been reported in molecular junctions, we put our results into context by drawing comparisons. We find here a conductance per unit area 0.0016 G_0/nm^2 for single-layer MoS_2. This is similar to reported conductances of single-molecular junctions, which are around 0.001 G0 [65,115–117] and the cross section of a molecule is typically estimated to be in the order of 1 nm^2. Moreover, the exponential decay of the conductance and the rise in S with the electrode distance is also known from studies of molecular junctions [118,119]. These similarities likely extent to other 2D materials and imply that 2D materials bear at least the same potential for thermoelectric applications as molecular junctions.

5.3 Summary

In summary, this work shows that quantum thermopower is generated in the cross-plane direction of MoS_2, suggesting that this effect occurs also in other 2D materials. This has been shown by contacting thin layers of MoS_2 which have been deposited on a gold electrode with a conductive AFM tip while a temperature gradient was applied, which results in the generation of a thermally induced voltage. This is relevant both to applications based on individual 2D materials and also to heterostructures made by stacks of dissimilar 2D materials in which the electrical and, in realistic conditions, thermoelectrical properties of each constituent influence the overall performance and functionality. Our findings are relevant for applications in hot-spot cooling and thermoelectric generators, both in terms of an improved understanding of device operation and also for new functionalities. Our work also provides an example of a high heat pumping capacity per unit area, which could lead to applications in hot-spot cooling, using cheap, non-toxic materials and a simple fabrication. These results represent the starting point for the search for 2D materials with optimal thermoelectric characteristics.

6 Ultrathin vertical MoS_2 p-n junction

Photovoltaic devices made of transition metal dichalcogenides, such as WSe_2 and MoS_2, are of great interest due to their strong light-matter interactions [120–122] and tuneable (thickness-dependent) band gaps [10,123]. The physical mechanisms governing rectification and photovoltaic response in vertical TMDC devices composed of monolayers are fundamentally different to the mechanisms in conventional p-n junctions. In monolayer MoS_2/WS2 heterojunctions the photovoltaic response is produced by spontaneous charge separation at the heterointerface [36,124,125]. At this interface illustrated in Figure 45 A, there is a type-II band alignment between the two materials with a band offset for electrons (ΔE_C) and for holes (ΔE_V), which allows photogenerated excitons to dissociate into free carriers because the lowest energy electron and hole states are spatially separated. The free carriers diffuse to the respective contacts and a part of them recombines through interlayer recombination mechanisms. In summary, the current-voltage characteristics of heterojunction devices are governed by interlayer tunnelling recombination of majority carriers rather than by conventional drift and diffusion processes. As a consequence, they have been reported not to follow an exponential law even for an ideal junction [36] and cannot be described by the Schockley diode model.

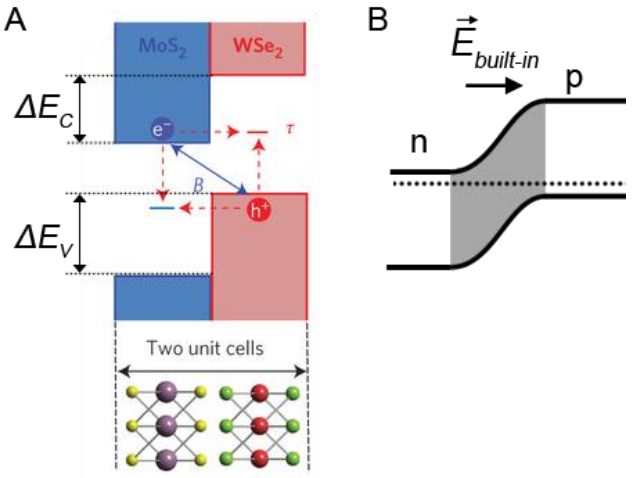

Figure 45: A) Band profiles of a MoS_2/WSe_2 heterostructure. Under forward bias, electrons (blue circles with 'e–') in the conduction band of MoS2 and holes (red circles with 'h+') in the valence band of WSe_2 undergo interlayer recombination via Shockley–Read–Hall (red dashed) or Langevin (blue arrow) mechanisms, contributing the dark current. τ and B are, respectively, the tunnelling-assisted recombination lifetime and the Langevin recombination constant. Note that there is no significant band bending in the lateral transport direction. Adapted from [36] B) Band structure of a classical p-n junction in which a built-in field occurs. The fermi level is marked as a dashed line.

The maximum achievable power of a photovoltaic device, and hence the potential efficiency, grows with the maximum achievable voltage, the open circuit voltage V_{OC}. In a p-n heterojunction V_{OC} is limited by the smallest of the band offsets, which is $\Delta E_C \approx 0.7$ eV (with $E=eV$) in the case of MoS_2/WSe_2 [125]. Contrarily, in a conventional p-n homojunction which is made exclusively of one material with spatial p- and n-doping, V_{OC} is limited by the built-in field (V_{bi}) and ultimately by the material bandgap (E_G = 1.8 eV for a MoS_2 monolayer), see Figure 45 b, which is higher than the smallest of the band offsets, resulting in a higher potential efficiency in homojunctions with respect to heterojunctions. This consideration motivates studies into 2D material homojunctions for photovoltaic applications

The formation of MoS_2 homojunctions is hampered by the lack of samples with both transport characteristics, n-type and p-type, since MoS_2 typically exhibits only n-type doping. Previous experimental efforts to form junctions have therefore focused on layered heterojunctions formed by vertical van der Waals stacking of dissimilar materials, mostly in combination with WSe_2 [36,126–128], and less frequently with other compounds such as GaTe [129], black phosphorus [130], and

graphene [37,131]. Besides, the possibility to form bipolar devices exclusively from MoS_2 has been explored with promising results but this could only be realized through superficial doping by exposing devices after processing to $AuCl_3$ [132,133], or through local electrostatic gating [134–137]. Recently, stable p-type conduction by substitutional niobium doping has been demonstrated in MoS_2 [138], which enables the formation of all-MoS_2 pn-junctions.

In this work, the characterization of vertical MoS_2 homostructures from vertical van der Waals assembly of p-type MoS_2 (0.5% Nb doping, $\sim 3 \times 10^{19}$ cm^{-3}) and n-type MoS_2 (either 0.5% Fe doping, or native n-type material) in the intermediate thickness regime (15 - 19 nm) between monolayer and bulk is presented. This thickness was chosen to allow V_{bi} associated with uncompensated dopant atoms in the space charge region to be allocated in the vertical dimension. It is demonstrated that in this thickness regime the current density-voltage (*J*-*V*) characteristics are in excellent agreement with the Shockley diode model, implying that the carrier dynamics in MoS_2 homojunctions is predominantly governed by drift and diffusion processes across the junction. The ideality factors are around 2.5 which indicate strong trap-assisted recombination in the depleted regions. The performance of the devices is substantially affected by the gate voltage (V_G) through the modulation of carrier densities. In particular, a positive effect of V_G on the open-circuit voltage (V_{OC}) is always accompanied by a negative effect on the short-circuit current (I_{SC}) which points to a carrier collection influenced by the spatial extent of the space charge region. Interestingly, not only the ideality factor but also the parasitic shunt resistance is modulated by the gate, suggesting that tunnel-assisted recombination at the surfaces is still relevant in devices of moderate thickness ($\sim$ 15 nm).

6.1 Light absorption in vertical MoS2 p-n junctions

p-type MoS_2:Nb and n-type MoS_2:Fe single crystals were provided by Ko Tsung-Shine and Lin Der-Yuh (National Changhua University of Education in Taiwan) who grew the crystals by the chemical vapour transport method described in Wang, S. Y. et al. [139]. Thin flakes of MoS_2:Nb, MoS_2:Fe, or not-intentionally doped MoS_2 (natural MoS_2) were prepared by exfoliation of bulk crystals, deposited onto a stamp, as described in chapter 3.3, and transferred onto a substrate with pre-patterned Au/Ti leads (40 nm/10 nm) on a 295 nm SiO_2/Si wafer. Figure 46 A shows a schematic of a device in which the transferred flake overlaps on both sides with contact pads. The flake can be biased by a source-drain voltage V_{SD} and a gate voltage V_G can be applied to the silicon. To illustrate the influence of V_G, the device can be modelled as a parallel plate capacitor, as shown in Figure 46B. One side of the capacitor, the flake, is approximately at a constant potential equal to ground (for $V_G >> V_{SD}$). A gate voltage can hence induce a charge $Q_\square$ in the flake,

$$Q_\square = C_\square V_G = e n_\square \qquad (69)$$

where $n_\square$ is the sheet carrier density (electrons), and $C_\square$ is the capacitance per unit area of the SiO_2 wafer, given by $C_\square = \varepsilon\varepsilon_0/d$. This is accompanied by the generation of an electric field E_{Gate}. = V/d, pointing as depicted in Figure 46B. For our samples, the thickness of the SiO_2 is d = 295 nm, the permittivity of SiO_2 is ε=3.9, and hence $C_\square = 1.2 \cdot 10^{-8}$ F/cm^2, which means that $n_\square$ increases by $7 \cdot 10^{10}$ cm^{-2} per Volt.

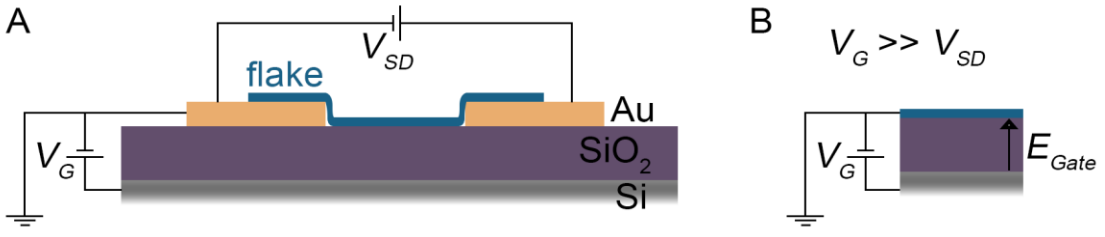

Figure 46: A) Schematic of a flake transferred to Au leads on a SiO_2/Si wafer. B) Simplified schematic for $V_G >> V_{SD}$. The voltage V_G induces an electric field E_{Gate}.

Since an increase in $n_{\square}$ results in an increase in conductivity of an n-doped material and a decrease if the material is p-doped, devices such as in Figure 46 can be used to qualitatively determine the doping. We have produced such devices with our materials, see Figure 47. The V_G-dependencies of p-type MoS_2:Nb and n-type MoS_2:Fe, confirm their supposed doping and we find that the not-intentionally doped MoS_2 is n-type. Note, that the quantitative values in conduction depend on the device size and geometry and are not further considered.

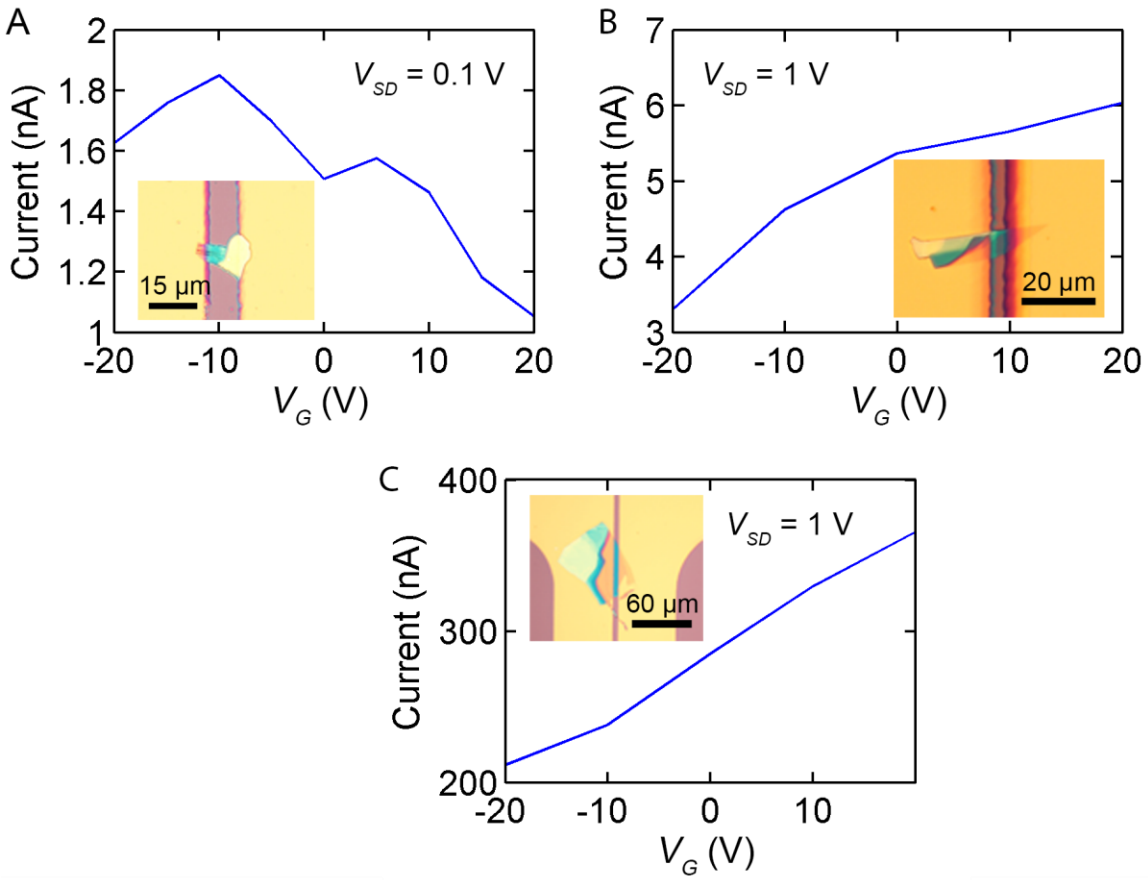

Figure 47: Gate dependence of dark current under a source drain bias V_{SD}. a) MoS_2:Nb. b) MoS_2:Fe. c) Natural MoS_2.

To form a p-n junction we deposited n-type MoS_2:Fe overlapping with one gold electrode and consecutively p-type MoS_2:Nb was deposited, overlapping with the n-type flake and thereby creating a vertical p-n homojunction. Figure 48 shows

schematics and optical images of the device after, respectively, the first and the second deposition of a crystal. The thicknesses of the flakes were determined to be 9 nm (MoS_2:Nb) and 6 nm (MoS_2:Fe) by atomic force microscopy.

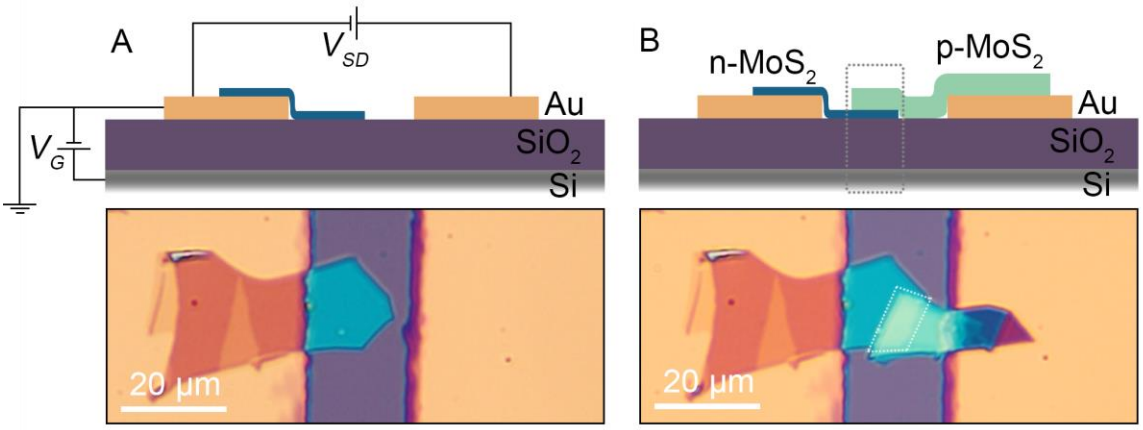

Figure 48: Device schematic and optical image of the n-type MoS_2:Fe flake on top of Au/Ti lead before (A) and after (B) the transfer of p-type MoS_2:Nb.

To characterise the p-n junctions, the current density J was recorded as a function of V_{SD} and V_G, in ambient conditions. Figure 49A, C, and D show J-V_{SD} characteristics of the device in the dark and under illumination with monochromatic light with a wavelength λ = 660 nm, and intensity 80 mW/cm^2 at various V_G values. As expected, the J-V_{SD} curves are rectifying and a photocurrent is produced under illumination. Each J-V_{SD} trace has been fitted using the circuital model depicted in Figure 49B. It comprises a Shockley-diode (equation (37)) and resistances in series (R_S) and in parallel (R_P) and is described by the equation

$$J = J_0\left(\exp\left(\frac{V_{SD} - JR_S}{nkT}\right) - 1\right) + \frac{V_{SD} - JR_S}{R_P} - J_L \qquad (70)$$

where k is the Boltzmann constant, T is the temperature, n is the ideality factor, J_0 is the reverse saturation current density and J_L is the photogenerated current density. The fits are overlaid in Figure 49A as solid lines. We find a good agreement between the experimental data and the Shockley model. The parameters n, J_0, J_L, R_S, and R_P characterise the diode and the photoresponse and have been extracted from the fits,

further discussed in subsection 6.2. Each of them is modulated by V_G and their V_G-dependence is in the focus of the discussion in the next section.

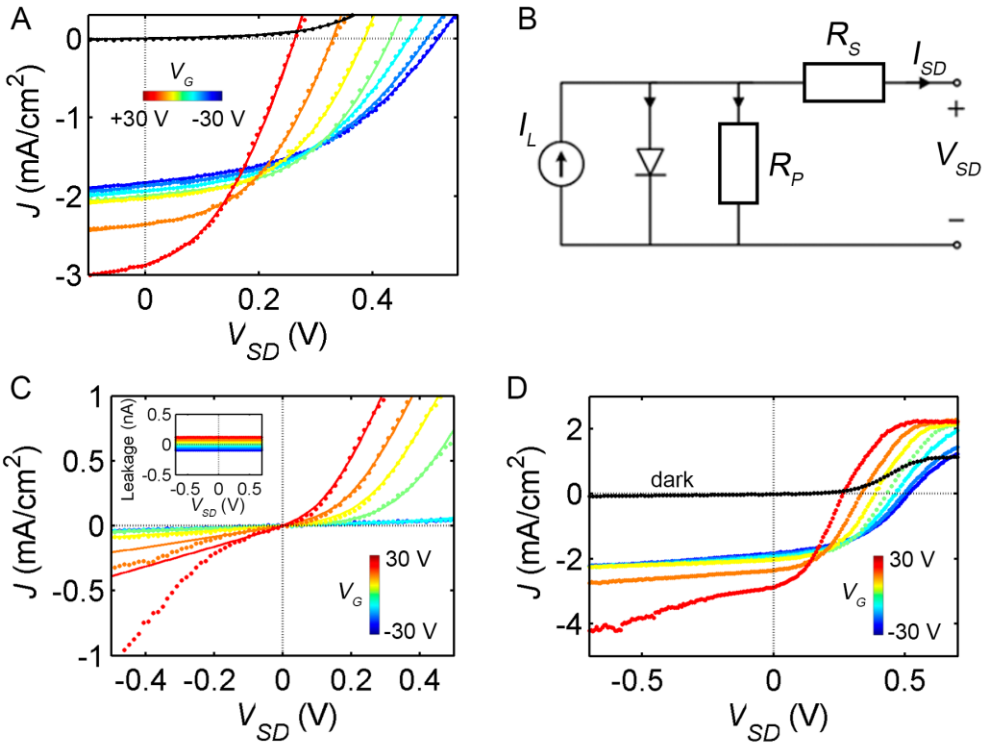

Figure 49:A) J-V_{SD} curves under illumination with λ = 660 nm at 80 mW/cm² at V_G = [+30 V, -30 V] in 10 V-steps (black: J-V_{SD} curve in the dark at V_G = 0 V). Experimental data is depicted as points and fits assuming the Shockley diode model are overlaid. B) Equivalent circuit model for a diode affected by a series resistance R_S and a shunt resistance R_P. C) Dark J-V_{SD} curves. Inset: gate leakage. D) J-V_{SD} curves under illumination as in, A, with a higher V_{SD} range.

The dark J-V_{SD} curves in Figure 49C also show gate-tuneable rectification. We find that the device is closer to reverse breakdown at high V_G, which is further discussed in the next section. The Shockley model equations do not model the reverse breakdown which accounts for the deviation of the model from the data for negative V_{SD}. The inset in Figure 49C shows the gate leakage-current, which, in no device, exceeds 150 pA.

Figure 49D shows J-V_{SD} curves for higher V_{SD}, showing a saturation of J at positive biases. We attribute this to either Schottky barriers formed at the

MoS_2/metal interface or barriers forming in the direction parallel to the flake when moving away from the junction area toward the electrode contacting the MoS_2 [140] However, most relevant for photovoltaic applications is quadrant IV, i.e. at positive V_{SD} and negative J, in which the effects of the leads are small, which has been confirmed by scanning the incident light across the surface with micromanipulators and measuring that J in quadrant IV is unaffected.

Figure 51 shows the generated electrical power density $P_{el} = -J\,V_{SD}$ for various V_G. A maximum of P_{el} = 0.42 mW/cm^2 and V_{OC} = 0.51 V is generated at V_G = -30 V. As discussed above, the V_{OC} is only limited by the band gap (with $E=eV$) and indeed exceeds reported values at similar intensities of van der Waals heterojunctions made of MoS_2/WSe_2[36,141], MoS_2/GaTe[129], and MoS_2/black phosphorous[130], although has been exceeded by graphene/MoS_2/WSe_2/graphene junction[36] due to enhanced extraction.

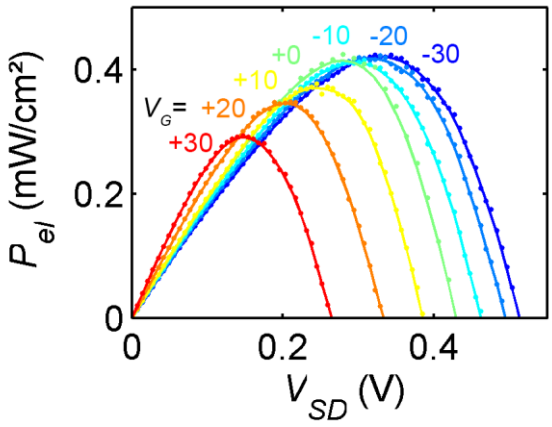

Figure 50: The generated electrical power density P_{el} against V_{SD} at various V_G.

Figure 51A, B show the dependencies of the J-V_{SD} characteristics and P_{el} on the incident power under illumination (λ = 660 nm). The maximum values are P_{el} = 0.68 mW/cm^{2}and J_{SC} = 3.3 mA/cm^2 which corresponds to an external quantum efficiency of EQE = 4.7 % and a responsivity of 25 mA/W., which is similar to reported values of MoS_2 homojunctions formed through surface doping and measured in vacuum (30 mA/W) [132]. The fill factor $FF \approx 0.46$ has been determined from max(P_{el})= $V_{OC}\,J_{SC}\,FF$.

The dependencies of V_{OC} and J_{SC} are, respectively, logarithmic and linear on the incident power as expected for a Shockley-diode, see Figure 51C. This also implies that the photocurrent is predominantly caused by the photovoltaic effect and not by thermoelectric effects [137], since V_{OC} goes linear with the incident power when it is induced by thermoelectricity as discussed in section 2.3, The Seebeck effect.

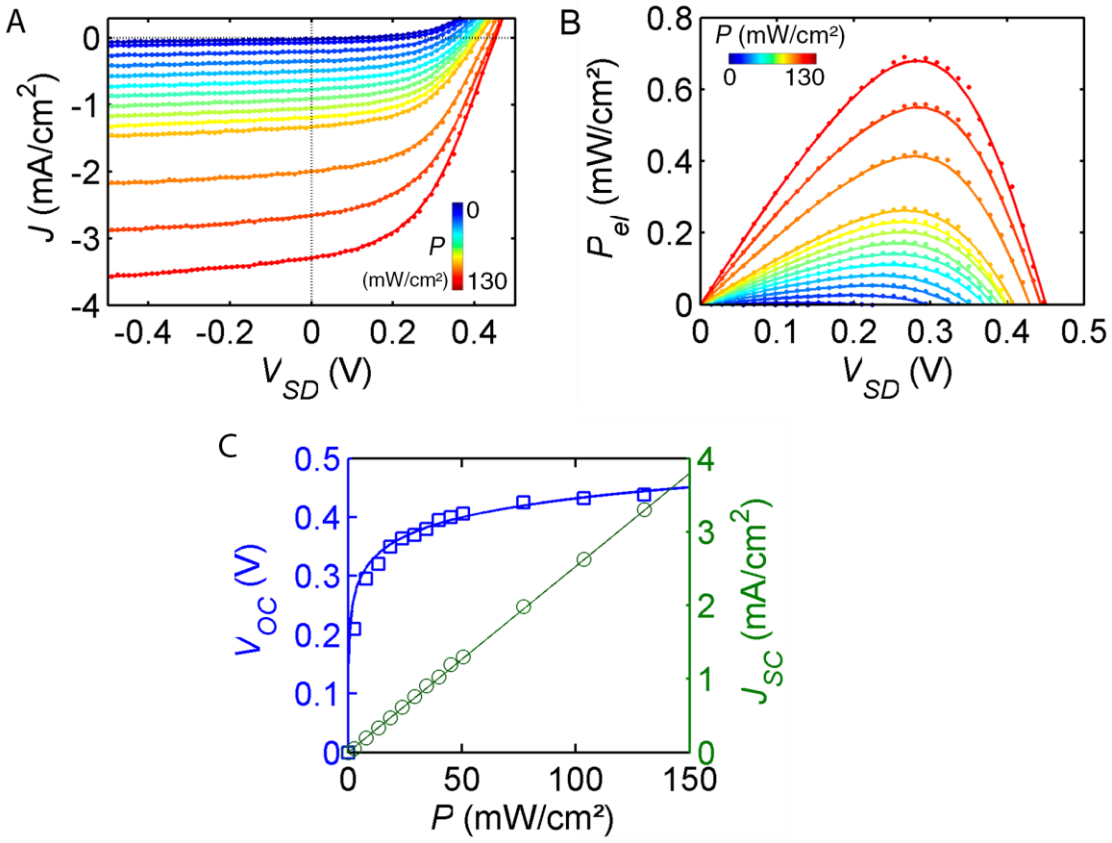

Figure 51: Device characteristics under illumination with λ = 660 nm at V_G = 0 V. The incident power ranges from 0 to 130 mW/cm². A) Power dependence of J-V_{SD} characteristics. B) Incident power dependence of the electrical power density P_{el} vs. V_{SD}. C) Logarithmic (linear) power-dependence of V_{OC} (J_{SC}) extracted from A.

J-V_{SD} characteristics were recorded for various illumination wavelengths between 405 nm and 1050 nm, see Figure 52. The response has a peak in the vicinity of the exciton energies 659 nm and 611 nm (in monolayer material)[142], where the optical absorption is enhanced. Photons with λ ≥ 850 nm correspond to energies below 1.46 eV ($E=hc/\lambda$). We find that these photons do not cause a photovoltaic response, and

are therefore not absorbed. Since the bulk band-gap is 1.29 eV [10], this implies that the band gap is widened. The response for wavelengths between 455 nm and 660 nm corresponds to *EQEs* which range from 1.6 % to 4.5 %.

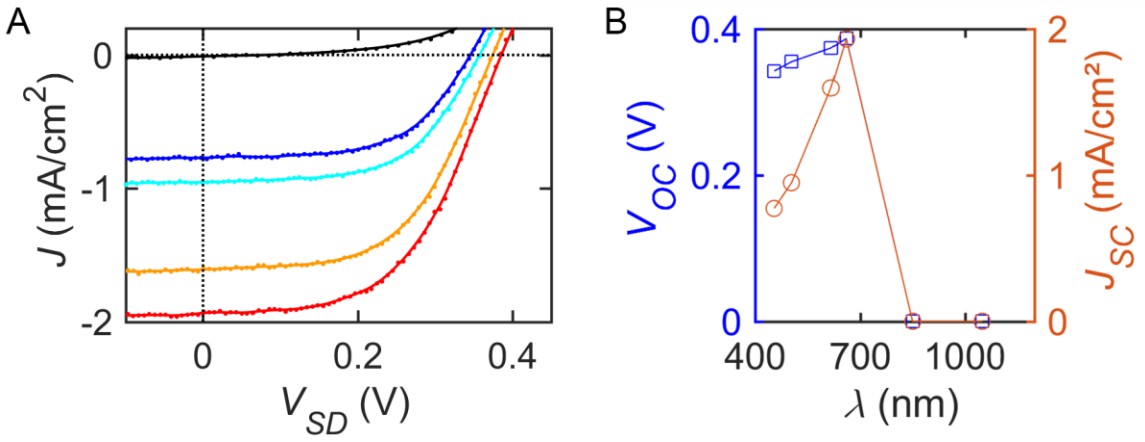

Figure 52: A) J-V_{SD} curves at different illumination wavelengths at 80 mW/cm². The device shows no photoresponse at wavelengths $\lambda \geq 850$ nm. B) Dependencies of V_{OC} and J_{SC} on the wavelength of the incident light.

A diode can be used as a light sensor. A typical figure of merit to characterise a sensor is the switching speed, which defines the time that passes when the signal appears or disappears before the sensor recognises this change. To determine the switching speed we recorded J vs. time while the illumination (λ = 660 nm, intensity 80 mW/cm^2) was alternatingly turned on and off (Figure 53). When the device is unbiased we extract an upper limit of 80 ms for both the rise and decay times (black curve). Note, that this value is limited by our experimental setup. This temporal response is one order of magnitude faster than previously reported MoS_2 photodetectors with planar geometries[143], however, 9 orders of magnitude slower than values reported in graphene/transition metal dichalcogenide/graphene devices[108]. The strong variation in response times can be attributed to differences in the device geometries and extraction efficiencies. Response times in planar MoS_2 photodetectors are limited by the capacitance that is induced by trapped charge carriers. Faster response times in few-layer MoS_2 in ambient conditions (~10 ms) could only be realised by surface treatments, such as encapsulation with HfO_2[144]. Under forward bias, V_{SD} = 0.5 V (red curve), the photoresponse comprises also a

photoconductance mechanism and the response time has been determined as 180 ms. In summary, that the photovoltaic effect is at least 100 ms faster than other response mechanisms, which is attributed to the device geometry. As above, the switching behaviour is also similar to classical p-n junctions, in which the response time decreases with increasing V_{SD} [145].

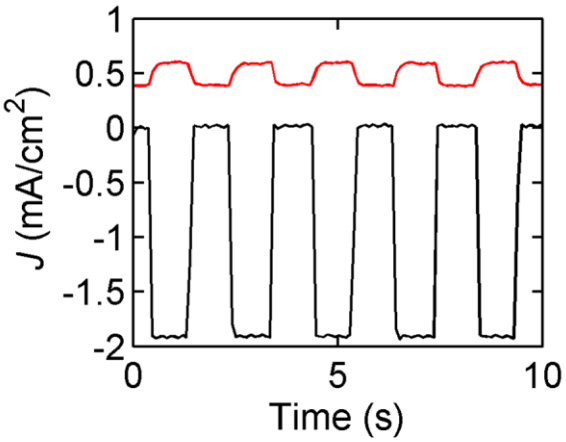

Figure 53: Current density across the device against time at VG = 0 V. The illumination (80 mW/cm at λ = 660 nm) was alternatingly turned on and off. Under short circuit conditions (black) we extract 80 ms as an upper limit for the response time. The response time at at VSD = 0.5 V (red) is determined as 180 ms.

We furthermore explore the potential for transparent and flexible substrates. Figure 54 A-D show optical images of a p-n (MoS_2:Nb – MoS_2:Fe, 10 nm – 9 nm) homojunction on a polycarbonate substrate in reflection- and transmission-mode. Approximately 50 % of the incident white light is transmitted through the electrodes. The transmittance of the device area varies in the range of 70 ± 15 %, suggesting that our materials may be used in quasi-transparent applications.

Figure 54 F shows the J-V_{SD} characteristics in dark and under illumination. From fitting the Schockley diode, as above, we find n = 2.46, I_0 = 0.3 pA, R_S = 0.7 GΩ, and negligible R_P in the dark and n = 2.84, I_0 = 5.8 pA, R_S = 70 MΩ and R_P = 7 GΩ under illumination with λ = 660 nm at a power of 80 mW/cm². We extract the maximum power density P_{el} = 0.11 mW/cm² at V_{SD} = 0.21 V. The other figures of merit are EQE = 1.5 %, and responsivity of 8 mA/W for J_{SC} = 0.66 mA/cm², V_{OC} = 0.32 V, and FF = 0.51. After bending the substrate 50 times to a local radius of curvature of 2.5 cm as

in Figure 54 E the *J-V*$_{SD}$ characteristics remain unaltered. Compared with the devices discussed above, the absence of a reflective background causes the lower device performance.

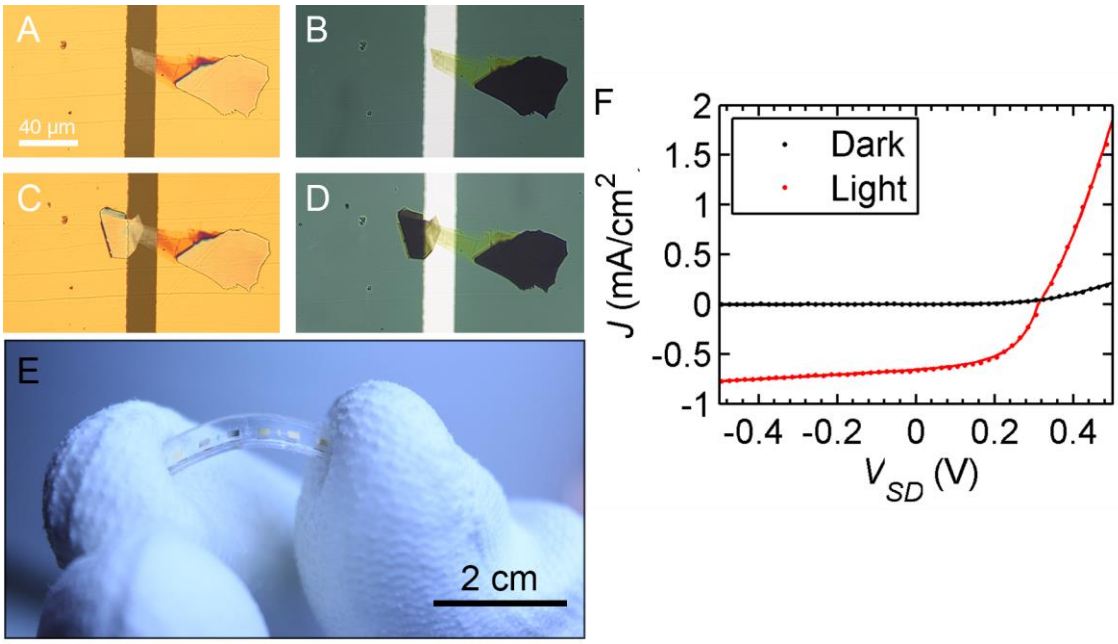

Figure 54: A-D) Optical images of a quasi-transparent device with MoS_2:Nb (A, B) and the MoS_2:Nb - MoS_2:Fe junction (C, D) in bright field (A, C) and transmission-mode (B, D) on a polycarbonate substrate with Au/Ti (70 nm/15 nm) leads. E) A photograph of the device. The scale bar refers to the focal plane of the camera. e) *J-V*$_{SD}$ curves in dark and under illumination with λ = 660 nm and 80 mW/cm². Fits assuming the Shockley diode model are overlaid as solid lines

6.2 Gate-voltage dependence of the diode characteristics

The possibility to modulate the diode and photoresponse characteristics by a gate voltage is novel, since in bulk semiconductors the number of carriers that can be generated by a gate voltage is insignificant and hence the device characteristics are unaffected. Studying the gate-dependence of a p-n junction is therefore only possible since the advent of 2D materials. In the following we analyse the gate-dependence of the parameters n, J_0, J_L, R_S, and R_P which have been extracted from Figure 49 using equation (70).

The agreement between the data and the Shockley-diode model implies that the carrier dynamics can be explained using the concepts described in section 2.4, Shockley p-n junction model, most importantly the built-in field $E_{built\text{-}in}$ and the associated space charge region. This is illustrated in an ideal band diagram, see Figure 55, in which the space charge region is marked in grey. Note that only the junction area, marked with dotted lines in Figure 48, is considered in the band diagram. In these devices, drift and diffusion of minority carriers exclusively takes place in the junction area and the space charge region does not spread horizontally beyond. This was confirmed by scanning the incident light across the surface with micromanipulators and measuring that the photocurrent in short-circuit conditions is generated only in the junction area. This also confirms that none of the observed effects originates from Schottky junctions at the contacts.

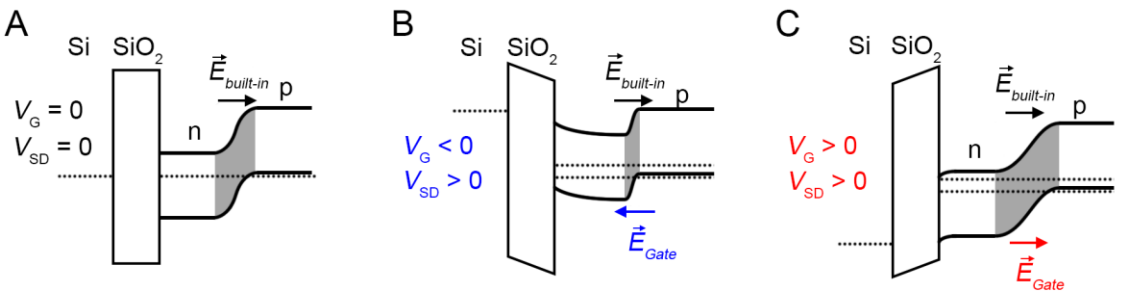

Figure 55: Ideal band diagrams of the junction area at V_G=0 (A), V_G < 0 (B), and V_G > 0 (C). The space charge region is marked in grey. V_G introduces E_{Gate} which enhances or reduces the total field $E_{built\text{-}in}$+E_{Gate} and thereby contributes to the band bending.

The thickness of the space charge region grows with V_G because a non-zero V_G produces either depletion or accumulation in the carrier population of the flakes and causes an additional field E_{Gate} parallel to the built-in field $E_{built\text{-}in}$ at the junction, which alters the band bending and the relative position of the bands with respect to the Fermi level. For negative V_G, the n-MoS_2 tends to be depleted, the p-MoS_2 accumulates carriers, and consequently $E_{built\text{-}in}$ is reduced by E_{Gate}. This is accompanied by a reduction of the thickness of the space charge region since the density of ionized dopant atoms which provide the field is predetermined by the doping. A positive V_G has the opposite effects. Furthermore, the band bending introduced by E_{Gate} resembles a forward source-drain bias for negative V_G and vice versa.

The diode characteristics are dominated by recombination at traps in the space charge region. This can be inferred from the V_G dependence of the ideality factor n, which is in the range [2 – 3.5], see Figure 56A. This V_G dependence is indicative of recombination mechanisms that become less efficient as V_{SD} increases. Such recombination is associated with coupled defects and tunnelling mechanisms [146,147], which most likely occur in the space charge region where defects are not saturated and where the electric field enhances tunnelling. The dramatic increase of n with decreasing V_G is consistent with tunnelling–assisted recombination at traps in the space charge region since tunnelling becomes less effective as the total field in the junction is reduced. It has to be noted that the depleted regions generated by V_G at the MoS_2/SiO_2 interface (see Figure 55) do not necessarily contribute to this recombination because carriers are prevented to approach the MoS_2/SiO_2 interface by the presence of the depleting fields.

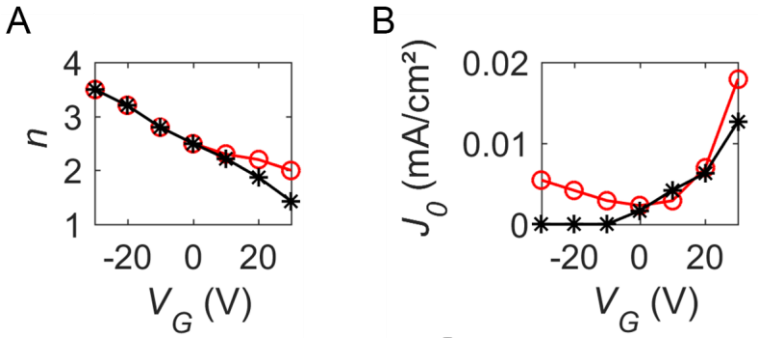

Figure 56: V_G dependencies of the ideality factor n (A) and the

Since the diode characteristics are dominated by recombination at traps in the space charge region the amount of recombination, characterized by J_0, is expected to increase with the thickness of the space charge region. This is consistent with the extracted values of J_0, see Figure 56B.

The parameter J_L is the photogenerated current when no voltage is applied across the junction. Under such circumstances there can be no quasi-Fermi level split in the space charge region and therefore recombination can only take place in the rest of the device. Hence, J_L accounts for the total photogenerated electron-hole pairs reduced by the recombination that takes place in the volume which is not occupied by the space charge region under short-circuit conditions [59]. Consequently, J_L increases with V_G, see . The absolute value of J_L in our devices is in the range [1.9 – 3.0 mA/cm^2].

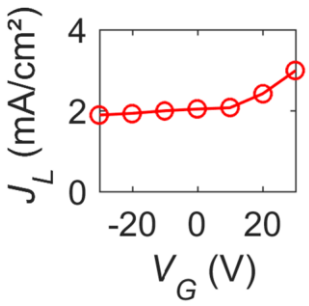

Figure 57: V_G dependence of the reverse saturation current density J_0.

Interestingly, we find different R_P values in the dark and under illumination, see Figure 58A. R_P quantifies local shuntings, which here, are due to defects in the space charge region. As above, the tunnelling is enhanced when the total field is increased by V_G, which leads to a higher current flow per trap, and hence a decrease in R_P. Under illumination we find a constant R_P independently of the gate. This is an apparent R_P related to a modulation of the photogenerated current and not to shunting. It reflects an increase of the photogenerated current as V_{SD} decreases which occurs due to the enlargement of the space charge region (similar to the case of positive V_G discussed above). This is known from other technologies of thin film solar cells, such as CdTe and chalcopyrite-based devices, in which the space charge region occupies a significant part of the total volume, and it is known as *voltage-dependent collection* [148].

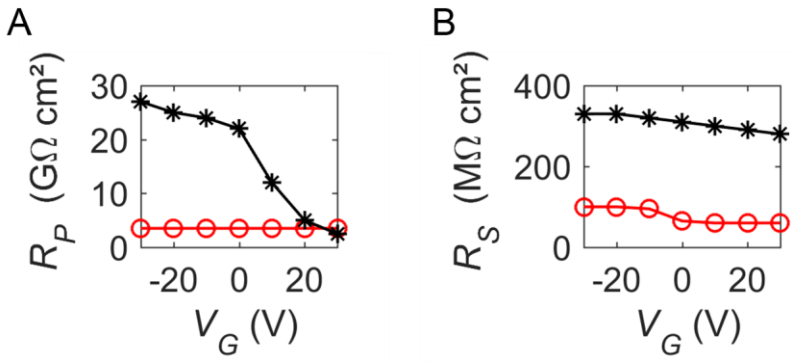

Figure 58: V_G dependence of the series resistance R_S (a) and shunt (parallel) resistance R_P (B).

The series resistance R_S of the flakes depends on the occupation levels, such as discussed above for regarding Figure 46. As V_G increases the Fermi level is shifted towards the conduction band causing the resistance of the n-type (or p-type) flake to decrease (or increase). In the p-n junction we observe a decrease of the resistance with an increasing V_G which implies that the gate-dependence of the n-type flake is predominant. This is attributed to the lower thickness of the n-type flake. R_S shows the same gate-dependence in the dark and under illumination. When illuminated R_S is smaller than in the dark because of a higher over-all population. The values are in the range [60 - 100 MΩ] under illumination and [280 - 330 MΩ] in the dark.

The positive effect of V_G on the photogenerated current is counteracted by a negative effect on the photovoltage, causing P_{el} to increase as V_G decreases (Figure 49 C). The previous analysis allows us to attribute both effects to the modulation of the space charge region. This result differs fundamentally from the behaviour of heterojunction-based WSe_2/MoS_2 devices, where a variation in V_G affects directly the amount of interlayer recombination and leads to either an increase of photovoltage and photocurrent, or the reduction of both [36]. Note that the device performance does not improve indefinitely since V_G introduces non-linear effects in the series resistance of the flakes leading to the junction.

6.3 Comparison to MoS_2:Nb – native MoS_2 device

The device fabrication and characterisation described in the section above were repeated twice and we found the same qualitative dependencies of all device parameters with variations in the absolute numbers due to a varying device thickness. Additionally, p-n (MoS_2:Nb – native MoS_2, 13 nm – 6 nm) homojunctions were prepared and characterised in the same way. Figure 59 gives an overview of the results.

We find the same qualitative dependences of n, I_0, R_P, and R_S on the gate voltage. Under illumination with λ = 660 nm and an intensity of 80 mW/cm, the maximum power P_{el} = 0.012 mW/cm² is generated at V_G = -10 V and at V_{SD} = 0.09 V. We extract V_{OC} = 0.14 V and FF = 0.4. The J_{SC} = 0.64 mA/cm² corresponds to EQE = 2.6 % and a responsivity of 14 mA/W. We attribute the lower device performance to the lower doping level of the native MoS_2 in comparison to the intentionally doped MoS_2. The device performance increases also with V_G, as above, but non-linear effects in the series resistance of the flakes lead to a maximum at V_G = -10 V.

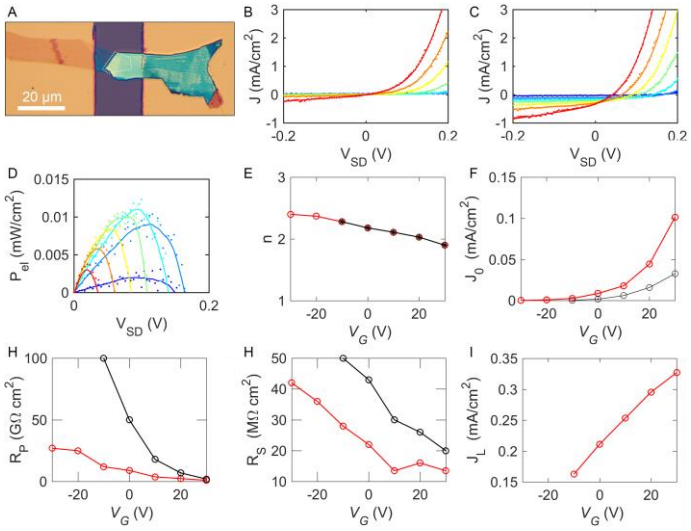

Figure 59: A) optical image of p-type MoS_2:Nb – natural n-type MoS_2 junction. B-C) *J-V* curves in the dark (B) and under illumination (C, λ = 660 nm at 80 mW/cm²). D) Electrical power generated. E-I) Fitting parameters extracted from Shockley-model-fits. Red: under illumination (λ = 660 nm at 80 mW/cm²), black: in the dark.

6.4 Summary

In summary, few-layer MoS_2 homojunctions have been fabricated. A p-type MoS_2:Nb – natural n-type MoS_2 junction exhibits an external quantum efficiency at 660 nm of 1.5 %. An equivalent device made of p-type MoS_2:Nb and n-type MoS_2:Fe shows an external quantum efficiency of 4.6 %. We find that devices in this intermediate thickness regime (15 - 19 nm) behave according to the Shockley diode model. We have thoroughly analysed the effect of electrostatic gating on the photoresponse and conclude that the thickness of the space charge region decreases with the gate voltage which is correlated with an increase in device performance. We have demonstrated a gate-induced shifting of the maximum power point, J_{SC} and V_{OC}. The device shows fast response times compared with previous studies on MoS_2 layers, which indicates that a vertical design could pave the way to faster MoS_2-based photodetectors. We have shown that devices made from substitutionally doped n-type material show superior device characteristics than devices made from native MoS_2. The p-n junctions demonstrate the potential of doped MoS_2 for quasi-transparent optical components in light harvesting cells and nanoscale optoelectronics.

7 Graphene/InSe hybrid devices

Vertical 2D material heterostructures in which a 2D material is contacted with graphene electrodes hold promise for high performance photodetectors because the high mobility of graphene implies potential for ultrafast detection speeds [149,150], and the separation of the graphene electrodes, determined by the thickness of the 2D material, is small, leading to a small carrier transit time, implying potential for high photosensitivity. Using 2D semiconductors as the absorbing material gives access to a broad spectral range by choosing appropriately the constituents [151] and the electronic band structure in 2D materials can be tuned by quantum mechanical confinement of charge carriers, enabling fine-tuning of the spectral range [151–154] and a high mechanical robustness facilitates band engineering through strain [155,156].

InSe is of particular interest for photodetectors because it is optically active in the technologically important near-infrared spectral range between 0.8 and 1 μm. Bendable photodetectors [157], image sensors [158], light-emitting diodes [159] based on InSe have been demonstrated showing the great potential for technological applications. Here, the formation of graphene/InSe/graphene vertical stacks is discussed. To fabricate these devices the transfer of CVD graphene with a focus on optimising the electrical properties was established, and a strategy to incorporate InSe into subsequently deposited graphene sheets, avoiding electrical shorts, was developed, all of which is laid out in the next section. This is followed by section 7.2, which contains a description of the optoelectrical properties of the devices.

7.1 Development of a fabrication process

Graphene was grown by chemical vapour deposition on copper by Neil Wilson's group at the University of Warwick and transferred to a SiO_2/Si as described in section 4.1. Figure 60 shows an optical and an SEM image of G/SiO_2 after the transfer. Defects have occurred during the transfer process whose nature has been investigated by characterisation with AFM, STM, SEM, energy dispersive x-ray analysis, optical microscopy and comparing the results of variations of the transfer method. The green contaminants in Figure 60 A are chrome oxide which is often used as an anti-oxidant for commercially available Cu foils. The bright patches are holes in the graphene. The dark patches in Figure 60 B are areas of bi-layer graphene and the dark lines are wrinkles. The graphene transfer was repeated numerous times in order to minimise the occurrence of these unwanted effects and further characterisation has been done by STM as discussed in section 4.1.

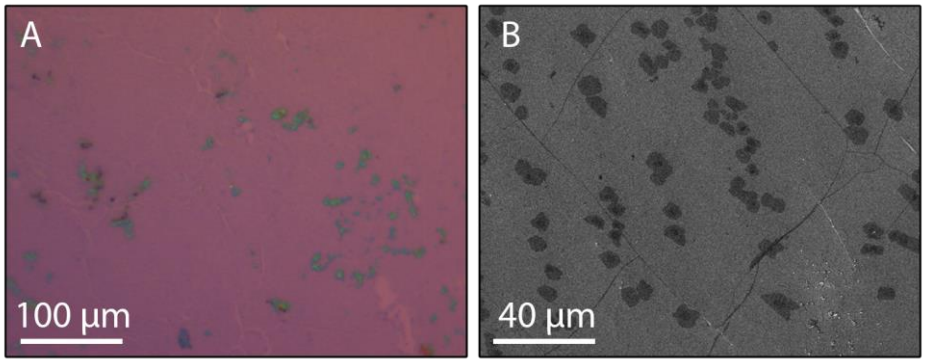

Figure 60: A) Optical and (B) SEM image of CVD graphene transferred to a SiO_2/Si wafer. The optical image shows traces of contaminants and tears in the graphene sheet. The SEM image reveals areas of double-layer graphene and wrinkles.

In order to form devices, the graphene was patterned by EBL. The procedure starts with spin-coating of the wafer with Micro Chem 498 PMMA A5 at 4000 rpm, which is subsequently annealed at 180 °C for 10 min, resulting in a film-thickness of ~150 nm. For this thickness and the typical accelerating voltage of the electron beam in our set-up (30 kV) we find to form well-defined patterns at doses of 200 $\mu C/cm^2$. The exposed PMMA is developed in a 7:3 mixture of propanol and deionised water at

room temperature for 8 s and afterwards rinsed in pure propanol and blow-dried. The lithographic pattern can be imprinted into the graphene by plasma etching the surface in an RIE system. We find that the recipe from reference [160] (200 mTorr, 25 sccm O_2, 75 W, 15 s) removes ~ 50 nm of PMMA and the entire uncovered graphene. Afterwards the PMMA is dissolved in acetone at an elevated temperature (60° C), leaving the graphene in a shape defined by the pattern. Alternatively, the pattern in the PMMA-film can define the lateral shape of metal contacts. In order to fabricate metal contacts, the material is deposited after the development by thermal evaporation on top of the partially coated wafer with a thickness of less than half of the thickness of the PMMA. After the PMMA is dissolved the metal is left on the surface. It is worth noting that the finding of these parameters and the correct execution of these seemingly simple steps are, in their practical implementation, troublesome and time-consuming.

By subsequently transferring graphene, finding a patch of graphene free of bilayers and contaminants, depositing metal contacts, and etching the graphene into shape, we fabricated hallbars to test if the procedure yields good results. A representative device is shown in Figure 61.

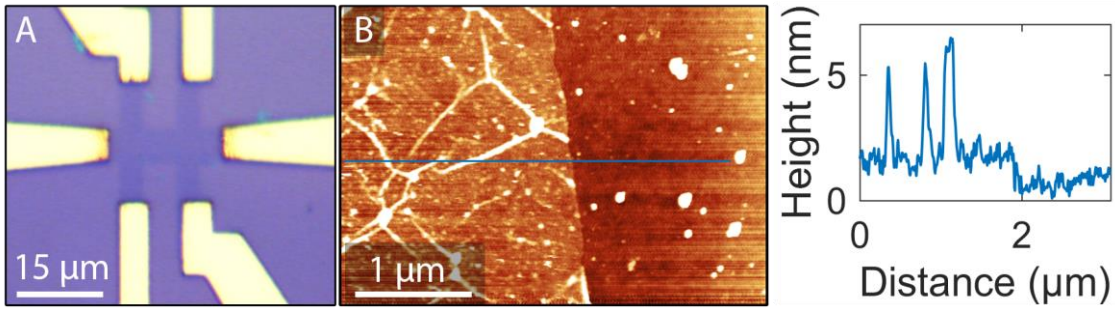

Figure 61: A) Optical image of a graphene hallbar on SiO_2./Si. Au/Ti leads connect the hallbar to contact pads. B) AFM image of the edge of the hallbar and a line profile along the indicated trace.

Figure 61 B shows an AFM image and a line profile. Folds run across the graphene with a height of $4 - 5$ nm, which is typical for transferred CVD graphene. Resist residue shows up as an increased roughness and thickness (~ 0.8 nm) of the graphene with respect to the SiO_2 and can be reduced by annealing which has been done for the samples in chapter 4 to enable STM. However, we have found that annealing does not necessarily improve the electrical properties but results in worsening in the values

for doping and mobility in the majority of our devices. This has been found by measuring the current I through the graphene while a constant bias V_{SD} was applied and the gate voltage V_G was varied, such as in section 6.1. A conductance G-V_G trace is shown in Figure 62. The shape of the trace is typical for graphene and is a manifestation of the gap-less band-structure. An applied gate voltage, or doping, shifts the Fermi-level with respect to the Dirac point, at which the conduction and valence band touch. At this point the carrier density and thereby the conduction is minimised, which is in Figure 62 at $V_G = 3$ V. The charge carrier density can be increased by shifting the Fermi level into either, for higher V_G, the conduction band or, for lower V_G, into the valence band. Consequently, the majority charge carriers at the left (right) hand side of the conductance minimum are holes (electrons).

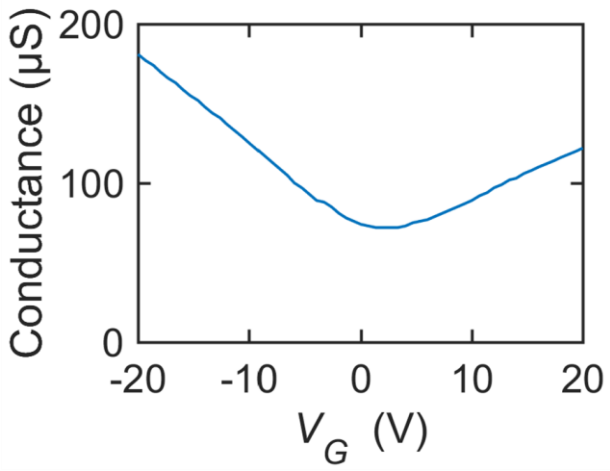

Figure 62: Conductance−V_G characteristics of a graphene field effect transistor fabricated using the methods described above, measured in ambient conditions. $V_{SD} = 0.1$ V.

To find the doping and the mobility we use the same model as described in section 6.1, which connects the sheet carrier density to the gate voltage by equation (69),

$$C_{\square} V_G = e n_{\square}$$

The mobility is per definition $\mu = \sigma_{\square}/(e n_{\square})$, where, in two dimensions, $\sigma_{\square} = G\ L/W$, where L is the length and W is the width of the graphene bar. Their ratio (here $20/6$) is the number of squares. This is plugged into equation (69) and solved for the mobility,

$$\mu = \frac{L}{W}\frac{1}{C_{\square}}\frac{dG}{dV_G}$$

The gradient dG/dV_G can be extracted from the linear regions in the Figure 62. We find an asymmetry in the mobilities of holes, $\mu = \sim 1500\ \mathrm{cm}^2/\mathrm{Vs}$, and electrons, $\mu = \sim 900\ \mathrm{cm}^2/\mathrm{Vs}$, which is common in CVD graphene [161]. The charge neutrality point is shifted from the optimal position by ~ 2 V, indicating unintentional p-doping by $\sim 1.4 \cdot 10^{11}\ \mathrm{cm}^{-2}$. We considered these electrical properties sufficient to start developing a processing procedure for more complex devices.

The fabrication of a G/InSe/G sandwich structure starts with the transfer of CVD graphene. InSe bulk crystals were grown at the Institute for Problems of Materials Science at the National Academy of Sciences of Ukraine in Chernivtsi by Z. D. Kovalyuk and Z. R. Kudrynskyi. The crystals were deposited onto the graphene by exfoliation which results in a random spatial distribution of InSe flakes. Appropriate flakes were chosen by optical inspection and the thickness was determined using AFM, see Figure 63 A and B for an example. This was followed by EBL and plasma etching to form a graphene strip below the InSe, see figure Figure 63 C.

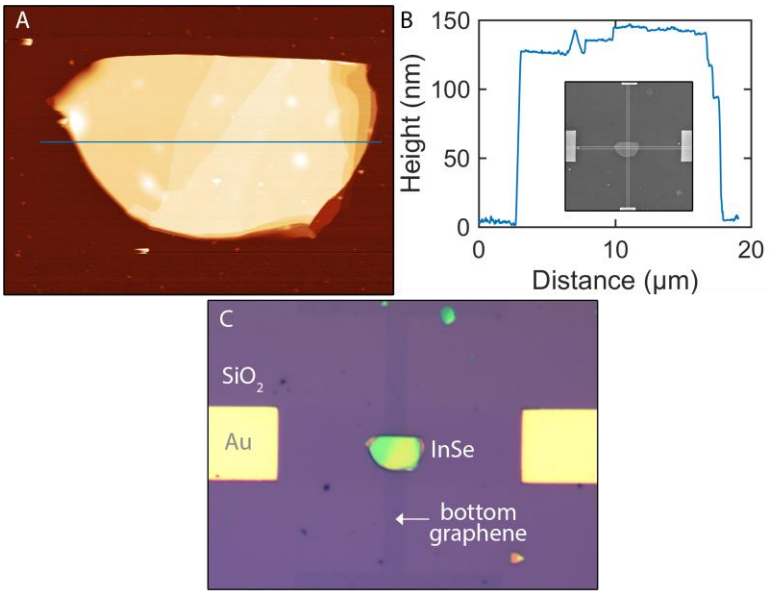

Figure 63: A) AFM image of InSe on G/SiO_2/Si. B) Profile along marked line in (A), showing a flake thickness of 130-145 nm. Inset: SEM image with lines indicating where the top and bottom graphene layers will be formed. C) Optical image of the device after the bottom graphene has been plasma-etched into a bar.

To form the top contact another layer of CVD graphene has to be transferred and, afterwards, etched into shape. However, we found that this produces short circuits between the top and the bottom graphene strip or the plasma-etching removes parts of the bottom strip. We therefore introduced a layer of positive resist into the device architecture, to be deposited before the transfer of the top graphene. The positive resist, once developed, remains on the sample in subsequent development steps, protects the lower graphene strip from etching, and prevents short circuits between the top and the bottom graphene. The positive resist covers the bottom graphene entirely and a window in the centre is left blank to allow the formation of physical contact between the top graphene and the InSe. This has the additional advantage that the active device-area is well-defined by the size of the window. A thus fabricated device is shown in Figure 64 A. Schematics of the device design are shown in Figure 64 B, and more devices fabricated in the same way are shown in Figure 64 C.

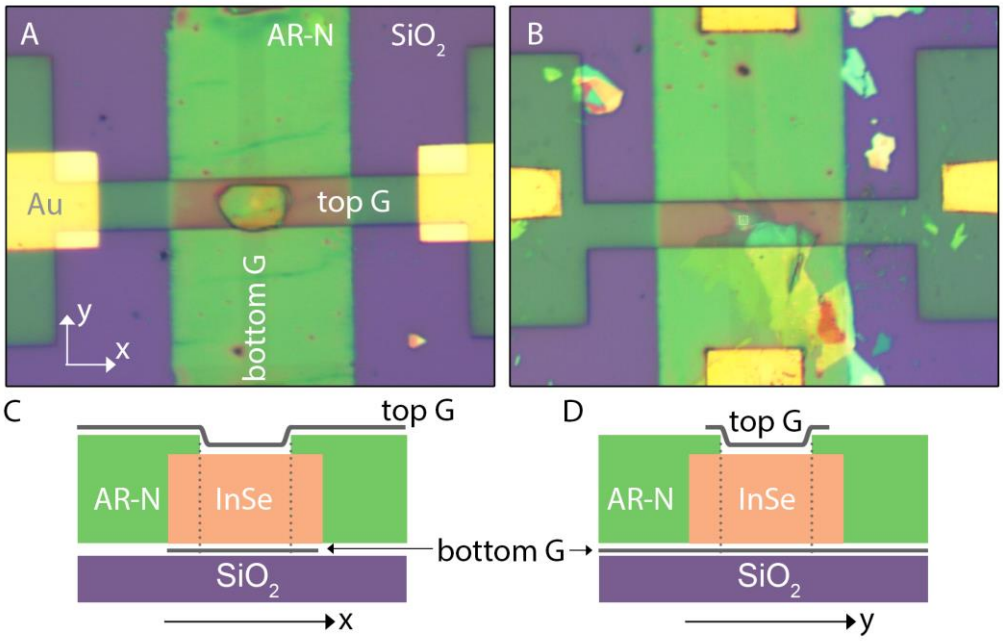

Figure 64: Optical images of graphene/InSe/graphene device 1 (A) and device 2 (B). The top and bottom graphene bars can be individually probed and connect the top and bottom of a InSe flake. The negative resist AR-N prevents electrical short circuits between the graphene bars. The active device-area is marked with a dotted white line in (B). C, D) Cross-sectional device schematics along the x and y axis, respectively. The dotted lines indicate the active device-area.

7.2 Optoelectrical characterisation

The optoelectronic characterisation of these devices was done jointly with Garry Mudd at the University of Nottingham. Figure 65 A shows the I-V_{SD} characteristics of the device 1, depicted in Figure 64 A, which are non-linear and asymmetric. This is in contrast to ohmic behaviour in devices in which InSe flakes are contacted by two graphene electrodes in a planar device architecture, which has been discussed in my Master's Thesis and in reference [162]. We attribute this difference to the fabrication procedure during which the InSe surfaces suffer from prolonged air-exposure and come in contact with polymer resists and organic solvents, which may compromise the graphene-InSe interfaces. Despite this non-ohmic behaviour the device exhibits a stable and reproducible photoresponse, shown in Figure 64 B. By raster scanning the illumination source with across the device, we confirmed that the photoresponse is indeed only generated in what is indicated as the active device-area in Figure 64 B.

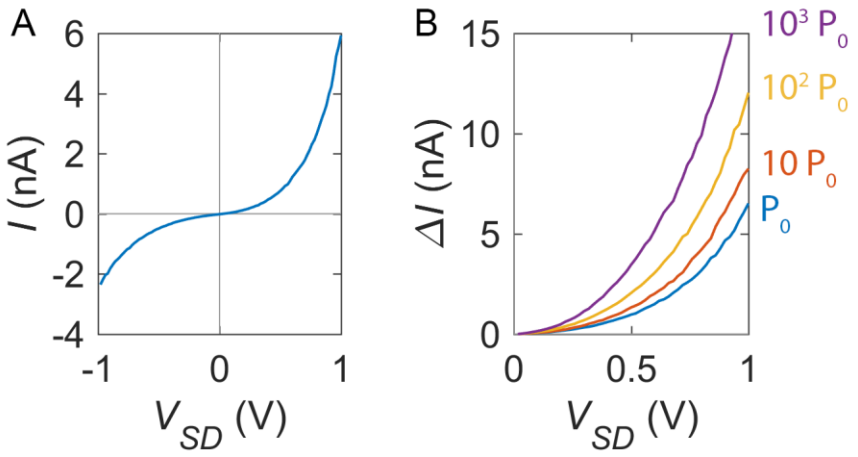

Figure 65: A) I-V_{SD} characteristics of a graphene/InSe/graphene sandwich structure in the dark, showing non-ohmic behaviour. B) Photocurrent vs. V_{SD} at room temperature under illumination with powers ranging from $P_0 = 100$ fW to $10^3\ P_0$ at $\lambda = 633$ nm.

The temporal response of the dark current has been measured by applying a square-wave voltage and measuring the maximum in I, see Figure 66. We find that the cut-off frequency is an order of magnitude higher ($\sim 10^5$ Hz) in the vertical structure

when compared to the devices with planar geometry. To measure the temporal response of the photogenerated current the illumination was mechanically modulated using a chopper wheel and we find a similar behaviour as reported for planar InSe-graphene structures.

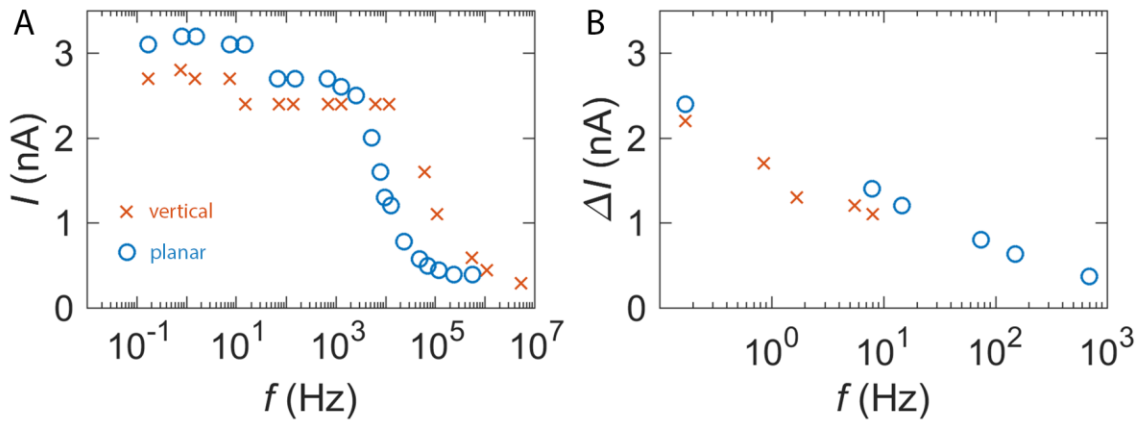

Figure 66: Temporal responses of the dark current (A) and the photocurrent (B) of the vertical G/InSe/G structures (red crosses, device 2, Figure 64 B, L = 80 nm) and the planar G/InSe devices (blue circles) (P < 1 mW, λ = 633 nm, V_{SD} = 1 V). For comparison, the values current-values of the planar device have been multiplied by 0.1 in (A) and 0.015 in (B).

The photoresponsivity $R = \Delta I/P$ is extracted from *I-V* curves at 1 V for a range of illumination powers with λ = 633 nm, see Figure 67. We find a maximum value of $R = 8{\cdot}10^3$ A/W. The mechanism responsible for this high responsivity is known as photoconductive gain [163], which occurs when incident light creates electron-hole pairs whose energy exceeds the band gap energy. Under steady state conditions, the densities of photogenerated electrons Δn and holes Δp are equal and can be expressed as

$$\Delta n = \Delta p = G\,\tau_p \tag{71}$$

where G is the generation rate and τ_p is the minority carrier lifetime, hence, the lifetime of holes since we use n-type material. The generation rate can be expressed as

$$G = \frac{\alpha l}{V}\frac{P\lambda}{hc} \tag{72}$$

where α is the absorption coefficient, l is flake thickness, V is the effective device-volume, and $P\lambda/hc$ is the number of incident photons. Since we use n-type material, and since the effective mass of electrons is smaller than the effective mass of holes in InSe [164] and consequently electrons have a higher mobility, the photocurrent is most probably dominated by electrons. It can be expressed as

$$\Delta I = \Delta n\, e\frac{V}{\tau_t} \tag{73}$$

where τ_t is the carrier transit time. Collecting equations (71) to (73), ΔI can be expressed as

$$\Delta I = e\alpha l\,\frac{P\lambda}{hc}\,\frac{\tau_p}{\tau_t} \tag{74}$$

The responsivity $R = \Delta I/P$ is therefore

$$R = e\alpha l\,\frac{\lambda}{hc}\,\frac{\tau_p}{\tau_t} \tag{75}$$

This suggests that large responsivities can be achieved if the lifetime of holes is longer than the transit time of the electrons. Using equation (75) with $R = 8{\cdot}10^3$ A/W, $\alpha = 4\cdot 10^5$ m^{-1}from references [165,166], $l = 80$ nm, λ = 633 nm, we can estimate $\tau_p/\tau_t \approx 5\cdot 10^5$.

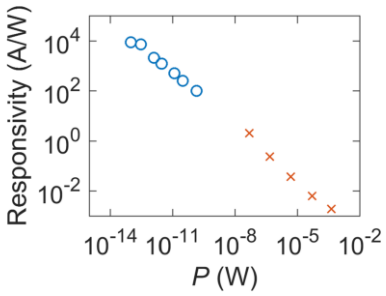

Figure 67: Responsivity of the graphene/InSe/graphene sandwich structure under illumination with λ = 633 nm at T = 300 K. Blue circles: Device 1, L = 130 and red crosses: Device 2, L = 80 nm.

The decrease of responsivity with increasing incident illumination powers is a common characteristic of photodetectors based on 2D materials with graphene electrodes [108,167–172], and can be understood considering equation (75). The ratio τ_p/τ_t governs the behaviour of *R.* With increasing incident power, the density of photogenerated carriers rises, causing an increase in scattering effects which likely increases the carrier transit time τ_t. A high population of charge carriers could also induce other recombination processes, and thereby decrease τ_p, which is reminiscent to the processes described in chapter 6, and is a very likely process in 2D materials which in general suffer strongly from surface-defects because of the low volume/surface ratio.

The here reported responsivities of up to $R \approx 8{\cdot}10^3$ A/W exceed photodetectors based on GaS, GaSe, and elemental black-phosophorous, which have responsivities of 10^4, 4.2 and 2.8, and 0.1 A/W, respectively [173–175]. The highest responsivities for the bilayer and trilayer-chalcogenides are reported for MoS_2 (10^3 A/W) and TiS_3 (10^3 A/W) [176,177]. A back-gate voltage (V_g = 40 V) applied to In_2Se_3 phototransistors can induce a larger photoresponsivity ($R \approx 10^5$ A/W) but at the expense of a much higher response time (~ 9 s) [178]. Similarly, a responsivity of $\sim 5{\cdot}10^7$ A/W has been reported for hybrid graphene-quantum dot phototransistors with response times in the order of seconds, although they could be reduced to the millisecond scale through application of pulsed electric fields to empty charge traps [179]. The trade-off between high-gain and slow response, or vice versa appears to be a common characteristic for van der Waals semiconductors [151,178]. However, it was predicted that advances in fabrication processes, for example by integrating devices into optical cavities [180], will enable fast high-gain photodetectors.

7.3 Summary

Our graphene/InSe/graphene sandwich devices exhibit a large responsivity, exceeding those reported for other photodetectors based on 2D materials with graphene or metal electrodes, which is attributed to a fast transit time of the electrons across the InSe channel, and is only exceeded by devices based on graphene and colloidal nanocrystals [181], whose performance tends to be compromised by a slow optical response (~1 s) due to the slow escape rate of photogenerated charges. In contrast, for this work, the mechanism responsible for the photoresponse, photoconductive gain, does not rely on a charge trapping effect, such as photo-gating, which enables the modulation of the dark and photocurrent at millisecond time scales.

The implementation of the fabrication processes to realise stacked 2D material devices using large-area CVD graphene represents significant progress since it offers a route to device scalability. The fabrication methods could be extended to similar material systems and more complex device architectures. Selective band alignments could be achieved by combining InSe with other semiconducting monochalcogenides (i.e., InX and GaX, where X = S, Se and Te) which cover a wide spectral range. Such devices could also be integrated with transparent and flexible polymer substrates and be part of next generation nanoscale optoelectronics.

8 Summary and Outlook

This thesis covers the characterisation of 2D materials in the presence of adsorbates and solvents, in the presence of a temperature gradient, or under illumination to either harvest or detect light. Accordingly, the key findings are diverse and are summarised as follows:

1. A transfer process of CVD graphene was developed and samples free of resist residues in areas above 10^4 nm^2 were fabricated.
2. Graphene at the interface between water and an organic solvent can be studied using STM. Samples for such studies can be fabricated by transferring graphene onto mica using a wet transfer method. The hydrophilicity of mica causes the trapping of water at the graphene/mica interface and the phase of the trapped water is not ice-like when the number of molecular layers is above 3.
3. On a soft support, the mechanical properties of an alkane/graphene system are governed by the geometrical conformation of the atomic structure of the adsorbate with respect to the graphene lattice.
4. Quantum thermopower is generated in the cross-plane direction of single- and few-layer 2D materials. This has been demonstrated by modifying a c-AFM system to enable the simulations measurement of the tip-sample temperature gradient and voltage, and probing MoS_2 crystals deposited on gold.
5. A temperature gradient in the cross-plane direction of few-layer MoS_2 generates quantum thermopower with a maximum of -330 ± 70 μV/K at 6 layers. This exceeds the highest previously reported values for quantum thermopower by one order of magnitude.
6. The heat pumping capacity of bilayer MoS_2 is 640 W/cm^2, exceeding previously reported values, and implying high potential for 2D materials in thermoelectric applications.
7. By stacking p-type and n-type MoS_2 we can generate light-harvesting homojunctions whose open circuit voltage is only limited by the band-gap. In our prototype devices, we find an open circuit voltage of 0.51 V which indeed exceeds values of comparable 2D materials heterojunctions. The

diode characteristics are dominated by recombination at traps in the space charge region whose extent, and with it the device performance, can be modulated by the gate voltage.

8. Although the Shockley diode model is not applicable to devices based on single-layer materials, it holds for few-layer devices with thicknesses of ~10 nm.
9. A processing procedure for the formation of graphene/InSe/graphene vertical sandwich structures was developed, and we find that the resulting devices are amongst the most photosensitive photodetectors reported to date.

Vertically stacked heterostructures based on 2D materials are a new paradigm in materials science, which allow the formation of devices with unprecedented functionality and the investigation of novel device physics. To date, and such as in chapter 6 and 7, the building blocks used in such structures are either graphene or inorganic 2D materials, usually exfoliated from bulk crystals. I see potential that 2D molecular monolayers, such as described in chapter 4 might be added as a new class of building block which can be formed through supramolecular organisation in a bottom-up approach with tuneable photo- and thermoelectric properties depending on the chemical composition and structure.

8.B Conclusiones

This chapter is a translation of chapter 8 into Spanish, a requirement for PhD theses by UAM.

Esta tesis doctoral se ocupa de la caracterización de materiales 2D en presencia de adsorbatos y disolventes, en presencia de un gradiente de temperatura y, por último, bajo iluminación, ya sea para detectar luz o para convertir su energía. Los resultados más relevantes se pueden resumir como sigue:

1. Se ha desarrollado un proceso de transferencia de grafeno CVD con el que se han llegado a fabricar muestras con un área de limpieza a escala atómica de 10^4 nm^2.
2. Se ha concluido que el grafeno situado en la interfaz entre agua y un disolvente orgánico puede ser estudiado mediante microscopía de efecto túnel. Las muestras para este tipo de estudios se pueden fabricar transfiriendo grafeno sobre mica mediante un método de transferencia húmeda. La hidrofilia de la mica causa el atrapamiento de agua en la interfaz grafeno/mica y este agua no se encuentra en fase sólida siempre que el espesor supere tres capas moleculares.
3. Sobre un soporte blando, las propiedades mecánicas de un sistema alcano/grafeno están gobernadas por la conformación geométrica de la estructura atómica del adsorbato con respecto a la red cristalina del grafeno.
4. En la dirección transversal a la estructura laminar de los materiales 2D se produce termopotencia cuántica. Para demostrar este fenómeno se ha modificado un microscopio de fuerza atómica conductivo para permitir la medida simultánea de gradientes de temperatura y tensiones eléctricas, y se han caracterizado cristales de MoS_2 depositados sobre oro.
5. Un gradiente de temperatura aplicado en la dirección transversal a la estructura laminar de un cristal multicapa de MoS_2 genera termopotencia cuántica con un máximo de -330 ± 70 μV/K para 6 capas. Este valor supera al más alto publicado para termopotencia cuántica por un orden de magnitud.

6. El valor máximo de la densidad de flujo térmico de una bicapa de MoS_2 es 640 W/cm^2, excediendo los valores publicados previamente, lo cual implica que los materiales 2D tienen un gran potencial para aplicaciones termoeléctricas.
7. Mediante el apilamiento de cristales de MoS_2 de tipo n y p podemos generar homouniones fotovoltaicas cuyas tensiones de circuito abierto solo están limitadas por el ancho de la banda prohibida del MoS_2. En nuestros dispositivos prototipos encontramos una tensión de circuito abierto de 0,51 V, la cual excede los valores reportados para heterouniones comparables de materiales 2D. Las características del diodo están dominadas por recombinación a través de trampas en la zona de carga del espacio. Esta recombinación, y con ella el rendimiento del dispositivo, puede ser modulada a través de la tensión de puerta.
8. A pesar de que el modelo del diodo de Shockley no es aplicable al flujo de portadores en dispositivos compuestos por cristales 2D de una monocapa, sí que lo es para dispositivos de pocas capas con espesores ~10 nm.
9. Se han desarrollado una estrategia de procesado de apilamientos verticales grafeno/InSe/grafeno. Encontramos que los dispositivos fabricados están entre los fotodectores más fotosensibles publicados hasta el momento.

References

[1] Novoselov, K. S., Geim, A. K., Morozov, S. V., Jiang, D., Zhang, Y., Dubonos, S. V., Grigorieva, I. V., and Firsov, A. A., 2004, "Electric field effect in atomically thin carbon films.," Science, **306**(5696), pp. 666–9.

[2] Geim, A. K., and Novoselov, K. S., 2007, "The rise of graphene.," Nat. Mater., **6**(3), pp. 183–191.

[3] Castro Neto, A. H., Peres, N. M. R., Novoselov, K. S., and Geim, A. K., 2009, "The electronic properties of graphene," Rev. Mod. Phys., **81**(1), pp. 109–162.

[4] Wallace, P., 1947, "The Band Theory of Graphite," Phys. Rev., **71**(9), pp. 622–634.

[5] Morozov, S., Novoselov, K. S., Katsnelson, M., Schedin, F., Elias, D., Jaszczak, J., and Geim, A. K., 2008, "Giant Intrinsic Carrier Mobilities in Graphene and Its Bilayer," Phys. Rev. Lett., **100**(1), pp. 11–14.

[6] Bolotin, K. I., Sikes, K. J., Jiang, Z., Klima, M., Fudenberg, G., Hone, J., Kim, P., and Stormer, H. L., 2008, "Ultrahigh electron mobility in suspended graphene," Solid State Commun., **146**(9–10), pp. 351–355.

[7] Novoselov, K. S., Jiang, D., Schedin, F., Booth, T. J., Khotkevich, V. V., Morozov, S. V., and Geim, A. K., 2005, "Two-dimensional atomic crystals," Proc. Natl. Acad. Sci., **102**(30), pp. 10451–10453.

[8] Li, X., and Zhu, H., 2015, "Two-dimensional MoS_2: Properties, preparation, and applications," J. Mater., **1**(1), pp. 33–44.

[9] Saito, Y., Nakamura, Y., Bahramy, M. S., Kohama, Y., Ye, J., Kasahara, Y., Nakagawa, Y., Onga, M., Tokunaga, M., Nojima, T., Yanase, Y., and Iwasa, Y., 2015, "Superconductivity protected by spin–valley locking in ion-gated MoS2," Nat. Phys., **12**(2), pp. 144–149.

[10] Mak, K. F., Lee, C., Hone, J., Shan, J., and Heinz, T. F., 2010, "Atomically Thin MoS_2: A New Direct-Gap Semiconductor," Phys. Rev. Lett., **105**(13), p. 136805.

[11] Yin, Z., Li, H., Li, H., Jiang, L., Shi, Y., Sun, Y., Lu, G., Zhang, Q., Chen, X., and Zhang, H., 2012, "Single-layer MoS_2 phototransistors.," ACS Nano, **6**(1), pp. 74–80.

[12] Lee, H. S., Min, S.-W., Chang, Y.-G., Park, M. K., Nam, T., Kim, H., Kim, J. H., Ryu, S., and Im, S., 2012, "MoS 2 Nanosheet Phototransistors with Thickness-Modulated Optical Energy Gap," Nano Lett., **12**(7), pp. 3695–3700.

[13] Pakdel, A., Bando, Y., and Golberg, D., 2014, "Nano boron nitride flatland," Chem. Soc. Rev., **43**(3), pp. 934–959.

[14] Dean, C. R., Young, A. F., Meric, I., Lee, C., Wang, L., Sorgenfrei, S., Watanabe, K., Taniguchi, T., Kim, P., Shepard, K. L., and Hone, J., 2010, "Boron nitride substrates for high-quality graphene electronics.," Nat. Nanotechnol., **5**(10), pp. 722–6.

[15] Brotons-Gisbert, M., Andres-Penares, D., Suh, J., Hidalgo, F., Abargues, R., Rodríguez-Cantó, P. J., Segura, A., Cros, A., Tobias, G., Canadell, E., Ordejón, P., Wu, J., Martínez-Pastor, J. P., and Sánchez-Royo, J. F., 2016, "Nanotexturing To Enhance Photoluminescent Response of Atomically Thin Indium Selenide with Highly Tunable Band Gap," Nano Lett., **16**(5), pp. 3221–3229.

[16] Bandurin, D. A., Tyurnina, A. V., Yu, G. L., Mishchenko, A., Zólyomi, V., Morozov, S. V., Kumar, R. K., Gorbachev, R. V., Kudrynskyi, Z. R., Pezzini, S., Kovalyuk, Z. D., Zeitler, U., Novoselov, K. S., Patanè, A., Eaves, L., Grigorieva, I. V., Fal'ko, V. I., Geim, A. K., and Cao, Y., 2016, "High electron mobility, quantum Hall effect and anomalous optical response in atomically thin InSe," Nat. Nanotechnol., **12**(3), pp. 223–227.

[17] Castellanos-Gomez, A., Buscema, M., Molenaar, R., Singh, V., Janssen, L., van der Zant, H. S. J., and Steele, G. A., 2014, "Deterministic transfer of two-dimensional materials by all-dry viscoelastic stamping," 2D Mater., **1**(1), p. 11002.

[18] Wang, X., Zhi, L., and Müllen, K., 2008, "Transparent, conductive graphene electrodes for dye-sensitized solar cells.," Nano Lett., **8**(1), pp. 323–7.

[19] Berger, C., Song, Z., Li, X., Wu, X., Brown, N., Naud, C., Mayou, D., Li, T., Hass, J., Marchenkov, A. N., Conrad, E. H., First, P. N., and de Heer, W. a, 2006, "Electronic confinement and coherence in patterned epitaxial graphene.," Science, **312**(5777), pp. 1191–6.

[20] Kim, K. S., Zhao, Y., Jang, H., Lee, S. Y., Kim, J. M., Kim, K. S., Ahn, J., Kim, P., Choi, J.-Y., and Hong, B. H., 2009, "Large-scale pattern growth of graphene films for stretchable transparent electrodes.," Nature, **457**(7230), pp. 706–10.

[21] Li, X., Cai, W., An, J., Kim, S., Nah, J., Yang, D., Piner, R., Velamakanni, A., Jung, I., Tutuc, E., Banerjee, S. K., Colombo, L., and Ruoff, R. S., 2009, "Large-area synthesis of high-quality and uniform graphene films on copper foils.," Science, **324**(5932), pp. 1312–4.

[22] Coraux, J., N'Diaye, A. T., Busse, C., and Michely, T., 2008, "Structural coherency of graphene on Ir(111).," Nano Lett., **8**(2), pp. 565–70.

[23] Sutter, P. W., Flege, J.-I., and Sutter, E. A., 2008, "Epitaxial graphene on ruthenium.," Nat. Mater., **7**(5), pp. 406–11.

[24] Lee, Y., Bae, S., Jang, H., Jang, S., Zhu, S.-E., Sim, S. H., Song, Y. Il, Hong, B. H., and Ahn, J.-H., 2010, "Wafer-scale synthesis and transfer of graphene films.," Nano

Lett., **10**(2), pp. 490–3.

[25] Singh, A. K., Ahmad, M., Singh, V. K., Shin, K., Seo, Y., and Eom, J., 2013, "Tailoring the electrical properties of graphene layers by molecular doping.," ACS Appl. Mater. Interfaces, **5**(11), pp. 5276–81.

[26] Wei, Y., Wu, J., Yin, H., Shi, X., Yang, R., and Dresselhaus, M., 2012, "The nature of strength enhancement and weakening by pentagon-heptagon defects in graphene.," Nat. Mater., **11**(9), pp. 759–63.

[27] Lee, J.-H., Lee, E. K., Joo, W.-J., Jang, Y., Kim, B.-S., Lim, J. Y., Choi, S.-H., Ahn, S. J., Ahn, J. R., Park, M.-H., Yang, C.-W., Choi, B. L., Hwang, S.-W., and Whang, D., 2014, "Wafer-scale growth of single-crystal monolayer graphene on reusable hydrogen-terminated germanium.," Science, **344**(6181), pp. 286–9.

[28] Kim, K. K., Hsu, A., Jia, X., Kim, S. M., Shi, Y., Dresselhaus, M., Palacios, T., and Kong, J., 2012, "Synthesis and characterization of hexagonal boron nitride film as a dielectric layer for graphene devices.," ACS Nano, **6**(10), pp. 8583–90.

[29] Reina, A., Jia, X., Ho, J., Nezich, D., Son, H., Bulovic, V., Dresselhaus, M. S., and Kong, J., 2009, "Large area, few-layer graphene films on arbitrary substrates by chemical vapor deposition.," Nano Lett., **9**(1), pp. 30–5.

[30] Li, X., Zhu, Y., Cai, W., Borysiak, M., Han, B., Chen, D., Piner, R. D., Colombo, L., and Ruoff, R. S., 2009, "Transfer of large-area graphene films for high-performance transparent conductive electrodes.," Nano Lett., **9**(12), pp. 4359–63.

[31] Cheng, Z., Zhou, Q., Wang, C., Li, Q., Wang, C., and Fang, Y., 2011, "Toward intrinsic graphene surfaces: a systematic study on thermal annealing and wet-chemical treatment of SiO_2-supported graphene devices.," Nano Lett., **11**(2), pp. 767–71.

[32] Pirkle, A., Chan, J., Venugopal, A., Hinojos, D., Magnuson, C. W., McDonnell, S., Colombo, L., Vogel, E. M., Ruoff, R. S., and Wallace, R. M., 2011, "The effect of chemical residues on the physical and electrical properties of chemical vapor deposited graphene transferred to SiO2," Appl. Phys. Lett., **99**(12), p. 122108.

[33] Kedzierski, J., Reina, A., Healey, P., Wyatt, P., and Keast, C., 2009, "Graphene-on-Insulator Transistors Made Using C on Ni Chemical-Vapor Deposition," IEEE Electron Device Lett., **30**(7), pp. 745–747.

[34] Dean, C., Young, a. F., Wang, L., Meric, I., Lee, G.-H., Watanabe, K., Taniguchi, T., Shepard, K., Kim, P., and Hone, J., 2012, "Graphene based heterostructures," Solid State Commun., **152**(15), pp. 1275–1282.

[35] Walukiewicz, W., 2001, "Intrinsic limitations to the doping of wide-gap semiconductors," Phys. B Condens. Matter, **302**–**303**, pp. 123–134.

[36] Lee, C., Lee, G., van der Zande, A. M., Chen, W., Li, Y., Han, M., Cui, X., Arefe, G., Nuckolls, C., Heinz, T. F., Guo, J., Hone, J., and Kim, P., 2014, "Atomically thin p–n junctions with van der Waals heterointerfaces," Nat. Nanotechnol., **9**(9), pp. 676–681.

[37] Britnell, L., Ribeiro, R. M., Eckmann, A., Jalil, R., Belle, B. D., Mishchenko, A., Kim, Y.-J., Gorbachev, R. V., Georgiou, T., Morozov, S. V., Grigorenko, A. N., Geim, A. K., Casiraghi, C., Neto, A. H. C., and Novoselov, K. S., 2013, "Strong Light-Matter Interactions in Heterostructures of Atomically Thin Films," Science, **340**(6138), pp. 1311–1314.

[38] Georgiou, T., Jalil, R., Belle, B. D., Britnell, L., Gorbachev, R. V., Morozov, S. V., Kim, Y.-J., Gholinia, A., Haigh, S. J., Makarovsky, O., Eaves, L., Ponomarenko, L. A., Geim, A. K., Novoselov, K. S., and Mishchenko, A., 2012, "Vertical field-effect transistor based on graphene–WS_2 heterostructures for flexible and transparent electronics," Nat. Nanotechnol., **8**(2), pp. 100–103.

[39] Whitesides, G. M., Mathias, J. P., and Seto, C. T., 1991, "Molecular self-assembly and nanochemistry: a chemical strategy for the synthesis of nanostructures.," Science, **254**(5036), pp. 1312–9.

[40] Barth, J. V, Costantini, G., and Kern, K., 2005, "Engineering atomic and molecular nanostructures at surfaces.," Nature, **437**(7059), pp. 671–9.

[41] Calhoun, M. F., Sanchez, J., Olaya, D., Gershenson, M. E., and Podzorov, V., 2008, "Electronic functionalization of the surface of organic semiconductors with self-assembled monolayers.," Nat. Mater., **7**(1), pp. 84–9.

[42] Nicosia, C., and Huskens, J., 2014, "Reactive self-assembled monolayers: from surface functionalization to gradient formation," Mater. Horizons, **1**(1), p. 32.

[43] Love, J. C., Estroff, L. a, Kriebel, J. K., Nuzzo, R. G., and Whitesides, G. M., 2005, "Self-assembled monolayers of thiolates on metals as a form of nanotechnology.," Chem. Rev., **105**(4), pp. 1103–69.

[44] Akkerman, H. B., Blom, P. W. M., de Leeuw, D. M., and de Boer, B., 2006, "Towards molecular electronics with large-area molecular junctions.," Nature, **441**(7089), pp. 69–72.

[45] Gundlach, D. J., and Jackson, T. N., 2001, "Pentacene TFT with improved linear region characteristics using chemically modified source and drain electrodes," IEEE Electron Device Lett., **22**(12), pp. 571–573.

[46] Collet, J., and Vuillaume, D., 1998, "Nano-field effect transistor with an organic self-assembled monolayer as gate insulator," Appl. Phys. Lett., **73**(18), p. 2681.

[47] Rabe, J. P., and Buchholz, S., 1991, "Commensurability and mobility in two-

dimensional molecular patterns on graphite.," Science, **253**(5018), pp. 424–7.

[48] Ilan, B., Florio, G. M., Hybertsen, M. S., Berne, B. J., and Flynn, G. W., 2008, "Scanning tunneling microscopy images of alkane derivatives on graphite: role of electronic effects.," Nano Lett., **8**(10), pp. 3160–5.

[49] Yang, T., Berber, S., Liu, J.-F., Miller, G. P., and Tománek, D., 2008, "Self-assembly of long chain alkanes and their derivatives on graphite.," J. Chem. Phys., **128**(12), p. 124709.

[50] Claypool, C. L., Faglioni, F., Goddard, W. A., Gray, H. B., Lewis, N. S., and Marcus, R. A., 1997, "Source of Image Contrast in STM Images of Functionalized Alkanes on Graphite: A Systematic Functional Group Approach," J. Phys. Chem. B, **101**(31), pp. 5978–5995.

[51] Florio, G. M., Werblowsky, T. L., Ilan, B., Müller, T., Berne, B. J., and Flynn, G. W., 2008, "Chain-length effects on the self-assembly of short 1-bromoalkane and n-alkane monolayers on graphite," J. Phys. Chem. C, **112**(46), pp. 18067–18075.

[52] 2006, Experimentalphysik 2, Springer Berlin Heidelberg, Berlin, Heidelberg.

[53] Büttiker, M., Imry, Y., Landauer, R., and Pinhas, S., 1985, "Generalized many-channel conductance formula with application to small rings," Phys. Rev. B, **31**(10), pp. 6207–6215.

[54] Ashcroft, N. W., and Mermin, N. D., 1976, Solid State Physics, Thomson Learning.

[55] Rincón-García, L., Evangeli, C., Rubio-Bollinger, G., and Agraït, N., 2016, "Thermopower measurements in molecular junctions," Chem. Soc. Rev., **45**(15), pp. 4285–4306.

[56] Evangeli, C., Matt, M., Rincón-García, L., Pauly, F., Nielaba, P., Rubio-Bollinger, G., Cuevas, J. C., and Agraït, N., 2015, "Quantum Thermopower of Metallic Atomic-Size Contacts at Room Temperature," Nano Lett., **15**(2), pp. 1006–1011.

[57] Manrique, D. Z., Al-Galiby, Q., Hong, W., and Lambert, C. J., 2016, "A New Approach to Materials Discovery for Electronic and Thermoelectric Properties of Single-Molecule Junctions," Nano Lett., **16**(2), pp. 1308–1316.

[58] Rowe, D., ed., 1995, CRC Handbook of Thermoelectrics, CRC Press.

[59] Luque, A., and Hegedus, S., 2010, Handbook of Photovoltaic Science and Engineering, John Wiley & Sons, Ltd, Chichester, UK.

[60] Bardeen, J., 1961, "Tunnelling from a Many-Particle Point of View," Phys. Rev. Lett., **6**(2), pp. 57–59.

[61] Samorí, P., 2006, Scanning Probe Microscopies Beyond Imaging: Manipulation of Molecules and Nanostructures, Wiley-VCH.

[62] Batra, I. P., García, N., Rohrer, H., Salemink, H., Stoll, E., and Ciraci, S., 1987, "A study of graphite surface with stm and electronic structure calculations," Surf. Sci., **181**(1–2), pp. 126–138.

[63] Binnig, G., and Quate, C. F., 1986, "Atomic Force Microscope," Phys. Rev. Lett., **56**(9), pp. 930–933.

[64] Reddy, P., Jang, S.-Y. S.-Y., Segalman, R. A., and Majumdar, A., 2007, "Thermoelectricity in molecular junctions.," Science, **315**(5818), pp. 1568–1571.

[65] Tan, A., Sadat, S., and Reddy, P., 2010, "Measurement of thermopower and current-voltage characteristics of molecular junctions to identify orbital alignment," Appl. Phys. Lett., **96**(1), p. 13110.

[66] Ku, H. Y., and Scala, L. C., 1969, "Polymeric Electron Beam Resists," J. Electrochem. Soc., **116**(7), p. 980.

[67] Harris, R. A., 1973, "Polymethyl Methacrylate as an Electron Sensitive Resist," J. Electrochem. Soc., **120**(2), p. 270.

[68] Castellanos-Gomez, A., Buscema, M., Molenaar, R., Singh, V., Janssen, L., van der Zant, H. S. J., and Steele, G. A., 2014, "Deterministic transfer of two-dimensional materials by all-dry viscoelastic stamping," 2D Mater., **1**(2014), p. 11002.

[69] Zomer, P. J., Dash, S. P., Tombros, N., and van Wees, B. J., 2011, "A transfer technique for high mobility graphene devices on commercially available hexagonal boron nitride," Appl. Phys. Lett., **99**(23), p. 232104.

[70] Wehling, T. O., Novoselov, K. S., Morozov, S. V, Vdovin, E. E., Katsnelson, M. I., Geim, a K., and Lichtenstein, a I., 2008, "Molecular doping of graphene.," Nano Lett., **8**(1), pp. 173–7.

[71] Schedin, F., Geim, a K., Morozov, S. V, Hill, E. W., Blake, P., Katsnelson, M. I., and Novoselov, K. S., 2007, "Detection of individual gas molecules adsorbed on graphene.," Nat. Mater., **6**(9), pp. 652–5.

[72] Chen, W., Chen, S., Qi, D. C., Gao, X. Y., and Wee, A. T. S., 2007, "Surface transfer p-type doping of epitaxial graphene.," J. Am. Chem. Soc., **129**(34), pp. 10418–22.

[73] Wang, Q. H., and Hersam, M. C., 2009, "Room-temperature molecular-resolution characterization of self-assembled organic monolayers on epitaxial graphene.," Nat. Chem., **1**(3), pp. 206–211.

[74] Mao, J., Zhang, H., Jiang, Y., Pan, Y., Gao, M., Xiao, W., and Gao, H.-J., 2009, "Tunability of supramolecular Kagome lattices of magnetic phthalocyanines using graphene-based moire patterns as templates.," J. Am. Chem. Soc., **131**(40), pp. 14136–7.

[75] Pollard, A. J., Perkins, E. W., Smith, N. a, Saywell, A., Goretzki, G., Phillips, A. G., Argent, S. P., Sachdev, H., Müller, F., Hüfner, S., Gsell, S., Fischer, M., Schreck, M., Osterwalder, J., Greber, T., Berner, S., Champness, N. R., and Beton, P. H., 2010, "Supramolecular assemblies formed on an epitaxial graphene superstructure.," Angew. Chem. Int. Ed. Engl., **49**(10), pp. 1794–9.

[76] Sun, X., Zhang, J., Wang, X., Zhang, C., Hu, P., Mu, Y., Wan, X., Guo, Z., and Lei, S., 2013, "Oligothiophenes on CVD graphene grown on multi-crystalline copper foil: supramolecular assembly and impact of morphology.," Chem. Commun. (Camb)., **49**(87), pp. 10317–9.

[77] Järvinen, P., Hämäläinen, S. K., Banerjee, K., Häkkinen, P., Ijäs, M., Harju, A., and Liljeroth, P., 2013, "Molecular Self-Assembly on Graphene on SiO_2 and h-BN Substrates.," Nano Lett.

[78] Li, B., Tahara, K., Adisoejoso, J., Vanderlinden, W., Mali, K. S., De Gendt, S., Tobe, Y., and De Feyter, S., 2013, "Self-assembled air-stable supramolecular porous networks on graphene.," ACS Nano, **7**(12), pp. 10764–72.

[79] Meyer, J. C., Geim, a K., Katsnelson, M. I., Novoselov, K. S., Booth, T. J., and Roth, S., 2007, "The structure of suspended graphene sheets.," Nature, **446**(7131), pp. 60–3.

[80] Lui, C. H., Liu, L., Mak, K. F., Flynn, G. W., and Heinz, T. F., 2009, "Ultraflat graphene.," Nature, **462**(7271), pp. 339–41.

[81] Taniguchi, T., and Watanabe, K., 2007, "Synthesis of high-purity boron nitride single crystals under high pressure by using Ba–BN solvent," J. Cryst. Growth, **303**(2), pp. 525–529.

[82] Watanabe, K., Taniguchi, T., and Kanda, H., 2004, "Direct-bandgap properties and evidence for ultraviolet lasing of hexagonal boron nitride single crystal.," Nat. Mater., **3**(6), pp. 404–9.

[83] Mattevi, C., Kim, H., and Chhowalla, M., 2011, "A review of chemical vapour deposition of graphene on copper," J. Mater. Chem., **21**(10), p. 3324.

[84] Yankowitz, M., Xue, J., Cormode, D., Sanchez-Yamagishi, J. D., Watanabe, K., Taniguchi, T., Jarillo-Herrero, P., Jacquod, P., and LeRoy, B. J., 2012, "Emergence of superlattice Dirac points in graphene on hexagonal boron nitride," Nat. Phys., **8**(5), pp. 382–386.

[85] Xue, J., Sanchez-Yamagishi, J., Bulmash, D., Jacquod, P., Deshpande, A.,

Watanabe, K., Taniguchi, T., Jarillo-Herrero, P., and LeRoy, B. J., 2011, "Scanning tunnelling microscopy and spectroscopy of ultra-flat graphene on hexagonal boron nitride.," Nat. Mater., **10**(4), pp. 282–5.

[86] Decker, R., Wang, Y., Brar, V. W., Regan, W., Tsai, H., Wu, Q., Gannett, W., Zettl, A., and Crommie, M. F., 2011, "Local electronic properties of graphene on a BN substrate via scanning tunneling microscopy.," Nano Lett., **11**(6), pp. 2291–5.

[87] McGonigal, G. C., Bernhardt, R. H., and Thomson, D. J., 1990, "Imaging alkane layers at the liquid/graphite interface with the scanning tunneling microscope," Appl. Phys. Lett., **57**(1), p. 28.

[88] Cyr, D. M., Venkataraman, B., and Flynn, G. W., 1996, "Reviews STM Investigations of Organic Molecules Physisorbed at the Liquid - Solid Interface," Chem. Mater., **4756**(96), pp. 1600–1615.

[89] Xu, K., Cao, P., and Heath, J. R., 2010, "Graphene visualizes the first water adlayers on mica at ambient conditions.," Science, **329**(5996), pp. 1188–91.

[90] He, K. T., Wood, J. D., Doidge, G. P., Pop, E., and Lyding, J. W., 2012, "Scanning tunneling microscopy study and nanomanipulation of graphene-coated water on mica.," Nano Lett., **12**(6), pp. 2665–72.

[91] Shim, J., Lui, C. H., Ko, T. Y., Yu, Y.-J., Kim, P., Heinz, T. F., and Ryu, S., 2012, "Water-gated charge doping of graphene induced by mica substrates.," Nano Lett., **12**(2), pp. 648–54.

[92] Kim, J.-S., Choi, J. S., Lee, M. J., Park, B. H., Bukhvalov, D., Son, Y.-W., Yoon, D., Cheong, H., Yun, J.-N., Jung, Y., Park, J. Y., and Salmeron, M., 2013, "Between scylla and charybdis: hydrophobic graphene-guided water diffusion on hydrophilic substrates.," Sci. Rep., **3**, p. 2309.

[93] Severin, N., Lange, P., Sokolov, I. M., and Rabe, J. P., 2012, "Reversible dewetting of a molecularly thin fluid water film in a soft graphene-mica slit pore.," Nano Lett., **12**(2), pp. 774–9.

[94] Svatek, S. A., Scott, O. R., Rivett, J. P. H., Wright, K., Baldoni, M., Bichoutskaia, E., Taniguchi, T., Watanabe, K., Marsden, A. J., Wilson, N. R., and Beton, P. H., 2015, "Adsorbate-Induced Curvature and Stiffening of Graphene," Nano Lett., **15**(1), pp. 159–164.

[95] Lu, Q., Arroyo, M., and Huang, R., 2009, "Elastic Bending Modulus of Monolayer Graphene," J. Phys. D. Appl. Phys., **42**(10), p. 5.

[96] Fasolino, A., Los, J. H., and Katsnelson, M. I., 2007, "Intrinsic ripples in graphene.," Nat. Mater., **6**(11), pp. 858–61.

[97] "NIST Database http://cccbdb.nist.gov/expgeom2.asp?casno=74986."

[98] Lindahl, N., Midtvedt, D., Svensson, J., Nerushev, O. a, Lindvall, N., Isacsson, A., and Campbell, E. E. B., 2012, "Determination of the bending rigidity of graphene via electrostatic actuation of buckled membranes.," Nano Lett., **12**(7), pp. 3526–31.

[99] Habbe, L., and Nurnus, J., 2011, "Thin film thermoelectrics today and tomorrow," Electron. Cool., **17**(3), pp. 24–31.

[100] Bulman, G., Barletta, P., Lewis, J., Baldasaro, N., Manno, M., Bar-Cohen, A., and Yang, B., 2016, "Superlattice-based thin-film thermoelectric modules with high cooling fluxes," Nat. Commun., **7**, p. 10302.

[101] Dobusch, L., Furchi, M. M., Pospischil, A., Mueller, T., Bertagnolli, E., and Lugstein, A., 2014, "Electric field modulation of thermovoltage in single-layer MoS_2," Appl. Phys. Lett., **105**(25), p. 253103.

[102] Buscema, M., Barkelid, M., Zwiller, V., van der Zant, H. S. J., Steele, G. A., and Castellanos-Gomez, A., 2013, "Large and tunable photothermoelectric effect in single-layer MoS_2.," Nano Lett., **13**(2), pp. 358–63.

[103] Wu, J., Schmidt, H., Amara, K. K., Xu, X., Eda, G., and Özyilmaz, B., 2014, "Large thermoelectricity via variable range hopping in chemical vapor deposition grown single-layer MoS_2.," Nano Lett., **14**(5), pp. 2730–4.

[104] Choi, S. J., Kim, B.-K., Lee, T.-H., Kim, Y. H., Li, Z., Pop, E., Kim, J.-J., Song, J. H., and Bae, M.-H., 2016, "Electrical and Thermoelectric Transport by Variable Range Hopping in Thin Black Phosphorus Devices," Nano Lett., **16**(7), pp. 3969–3975.

[105] Yoshida, M., Iizuka, T., Saito, Y., Onga, M., Suzuki, R., Zhang, Y., Iwasa, Y., and Shimizu, S., 2016, "Gate-Optimized Thermoelectric Power Factor in Ultrathin WSe_2 Single Crystals," Nano Lett., **16**(3), pp. 2061–2065.

[106] Yang, H., Heo, J., Park, S., Song, H. J., Seo, D. H., Byun, K.-E. K.-E., Kim, P., Yoo, I., Chung, H.-J. H.-J., and Kim, K., 2012, "Graphene Barristor, a Triode Device with a Gate-Controlled Schottky Barrier," Science, **336**(6085), pp. 1140–1143.

[107] Jariwala, D., Sangwan, V. K., Wu, C.-C., Prabhumirashi, P. L., Geier, M. L., Marks, T. J., Lauhon, L. J., and Hersam, M. C., 2013, "Gate-tunable carbon nanotube-MoS_2 heterojunction p-n diode.," Proc. Natl. Acad. Sci. U. S. A., **110**(45), pp. 18076–80.

[108] Massicotte, M., Schmidt, P., Vialla, F., Schädler, K. G., Reserbat-Plantey, A., Watanabe, K., Taniguchi, T., Tielrooij, K. J., and Koppens, F. H. L., 2015, "Picosecond photoresponse in van der Waals heterostructures," Nat. Nanotechnol., **11**(1), pp. 42–46.

[109] Deng, Y., Luo, Z., Conrad, N. J., Liu, H., Gong, Y., Najmaei, S., Ajayan, P. M., Lou, J.,

Xu, X., and Ye, P. D., 2014, "Black Phosphorus-Monolayer MoS_2 van der Waals Heterojunction P-N Diode.," ACS Nano, **8**(8), pp. 8292–8299.

[110] Frisenda, R., Niu, Y., Gant, P., Molina-Mendoza, A. J., Schmidt, R., Bratschitsch, R., Liu, J., Fu, L., Dumcenco, D., Kis, A., De Lara, D. P., and Castellanos-Gomez, A., 2017, "Micro-reflectance and transmittance spectroscopy: a versatile and powerful tool to characterize 2D materials," J. Phys. D. Appl. Phys., **50**(7), p. 74002.

[111] Shearer, C. J., Slattery, A. D., Stapleton, A. J., Shapter, J. G., and Gibson, C. T., 2016, "Accurate thickness measurement of graphene," Nanotechnology, **27**(12), p. 125704.

[112] Sadat, S., Meyhofer, E., and Reddy, P., 2012, "High resolution resistive thermometry for micro/nanoscale measurements," Rev. Sci. Instrum., **83**(8), p. 84902.

[113] Lee, W., Song, B., and Reddy, P., 2013, "Measurement of thermoelectric and thermal transport properties of single-molecule junctions," Annu. Rev. Heat Transf., **16**(1), pp. 259–286.

[114] Chowdhury, I., Prasher, R., Lofgreen, K., Chrysler, G., Narasimhan, S., Mahajan, R., Koester, D., Alley, R., and Venkatasubramanian, R., 2009, "On-chip cooling by superlattice-based thin-film thermoelectrics," Nat. Nanotechnol., **4**(4), pp. 235–238.

[115] Kim, Y., Jeong, W., Kim, K., Lee, W., and Reddy, P., 2014, "Electrostatic control of thermoelectricity in molecular junctions," Nat. Nanotechnol., **9**(11), pp. 881–885.

[116] Tan, A., Balachandran, J., Dunietz, B. D., Jang, S.-Y., Gavini, V., and Reddy, P., 2012, "Length dependence of frontier orbital alignment in aromatic molecular junctions," Appl. Phys. Lett., **101**(24), p. 243107.

[117] Rincón-García, L., Ismael, A. K., Evangeli, C., Grace, I., Rubio-Bollinger, G., Porfyrakis, K., Agraït, N., and Lambert, C. J., 2015, "Molecular design and control of fullerene-based bi-thermoelectric materials," Nat. Mater., **15**(3), pp. 289–293.

[118] Chang, W. B., Mai, C.-K., Kotiuga, M., Neaton, J. B., Bazan, G. C., and Segalman, R. A., 2014, "Controlling the Thermoelectric Properties of Thiophene-Derived Single-Molecule Junctions," Chem. Mater., **26**(24), pp. 7229–7235.

[119] Evangeli, C., Gillemot, K., Leary, E., González, M. T., Rubio-Bollinger, G., Lambert, C. J., and Agraït, N., 2013, "Engineering the thermopower of C_{60} molecular junctions," Nano Lett., **13**(5), pp. 2141–2145.

[120] Koppens, F. H. L., Mueller, T., Avouris, P., Ferrari, A. C., Vitiello, M. S., and

Polini, M., 2014, “Photodetectors based on graphene, other two-dimensional materials and hybrid systems,” Nat. Nanotechnol., **9**(10), pp. 780–793.

[121] Britnell, L., Gorbachev, R. V, Jalil, R., Belle, B. D., Schedin, F., Mishchenko, A., Georgiou, T., Katsnelson, M. I., Eaves, L., Morozov, S. V, Peres, N. M. R., Leist, J., Geim, A. K., Novoselov, K. S., and Ponomarenko, L. A., 2012, “Field-Effect Tunneling Transistor Based on Vertical Graphene Heterostructures,” Science, **335**(6071), pp. 947–950.

[122] Fortin, E., and Sears, W. M., 1982, “Photovoltaic effect and optical absorption in MoS_2,” J. Phys. Chem. Solids, **43**(9), pp. 881–884.

[123] Splendiani, A., Sun, L., Zhang, Y., Li, T., Kim, J., Chim, C.-Y., Galli, G., and Wang, F., 2010, “Emerging Photoluminescence in Monolayer MoS 2,” Nano Lett., **10**(4), pp. 1271–1275.

[124] Furchi, M. M., Pospischil, A., Libisch, F., Burgdörfer, J., and Mueller, T., 2014, “Photovoltaic Effect in an Electrically Tunable van der Waals Heterojunction,” Nano Lett., **14**(8), pp. 4785–4791.

[125] Kang, J., Tongay, S., Zhou, J., Li, J., and Wu, J., 2013, “Band offsets and heterostructures of two-dimensional semiconductors,” Appl. Phys. Lett., **102**(1), p. 12111.

[126] Heo, H., Sung, J. H., Cha, S., Jang, B.-G., Kim, J.-Y., Jin, G., Lee, D., Ahn, J.-H., Lee, M.-J., Shim, J. H., Choi, H., and Jo, M.-H., 2015, “Interlayer orientation-dependent light absorption and emission in monolayer semiconductor stacks,” Nat. Commun., **6**, p. 7372.

[127] Gong, Y., Lin, J., Wang, X., Shi, G., Lei, S., Lin, Z., Zou, X., Ye, G., Vajtai, R., Yakobson, B. I., Terrones, H., Terrones, M., Tay, B. K., Lou, J., Pantelides, S. T., Liu, Z., Zhou, W., and Ajayan, P. M., 2014, “Vertical and in-plane heterostructures from WS_2/MoS_2 monolayers,” Nat. Mater., **13**(12), pp. 1135–1142.

[128] Fang, H., Battaglia, C., Carraro, C., Nemsak, S., Ozdol, B., Kang, J. S., Bechtel, H. A., Desai, S. B., Kronast, F., Unal, A. A., Conti, G., Conlon, C., Palsson, G. K., Martin, M. C., Minor, A. M., Fadley, C. S., Yablonovitch, E., Maboudian, R., and Javey, A., 2014, “Strong interlayer coupling in van der Waals heterostructures built from single-layer chalcogenides,” Proc. Natl. Acad. Sci., **111**(17), pp. 6198–6202.

[129] Wang, F., Wang, Z., Xu, K., Wang, F., Wang, Q., Huang, Y., Yin, L., and He, J., 2015, “Tunable GaTe-MoS_2 van der Waals p–n Junctions with Novel Optoelectronic Performance,” Nano Lett., **15**(11), pp. 7558–7566.

[130] Deng, Y., Luo, Z., Conrad, N. J., Liu, H., Gong, Y., Najmaei, S., Ajayan, P. M., Lou, J., Xu, X., and Ye, P. D., 2014, “Black Phosphorus–Monolayer MoS_2 van der Waals

Heterojunction p–n Diode," ACS Nano, **8**(8), pp. 8292–8299.

[131] Yu, W. J., Liu, Y., Zhou, H., Yin, A., Li, Z., Huang, Y., and Duan, X., 2013, "Highly efficient gate-tunable photocurrent generation in vertical heterostructures of layered materials," Nat. Nanotechnol., **8**(12), pp. 952–958.

[132] Li, H.-M., Lee, D., Qu, D., Liu, X., Ryu, J., Seabaugh, A., and Yoo, W. J., 2015, "Ultimate thin vertical p–n junction composed of two-dimensional layered molybdenum disulfide," Nat. Commun., **6**, p. 6564.

[133] Choi, M. S., Qu, D., Lee, D., Liu, X., Watanabe, K., Taniguchi, T., and Yoo, W. J., 2014, "Lateral MoS_2 p–n Junction Formed by Chemical Doping for Use in High-Performance Optoelectronics," ACS Nano, **8**(9), pp. 9332–9340.

[134] Ross, J. S., Klement, P., Jones, A. M., Ghimire, N. J., Yan, J., Mandrus, D. G., Taniguchi, T., Watanabe, K., Kitamura, K., Yao, W., Cobden, D. H., and Xu, X., 2014, "Electrically tunable excitonic light-emitting diodes based on monolayer WSe_2 p–n junctions," Nat. Nanotechnol., **9**(4), pp. 268–272.

[135] Baugher, B. W. H., Churchill, H. O. H., Yang, Y., and Jarillo-Herrero, P., 2014, "Optoelectronic devices based on electrically tunable p–n diodes in a monolayer dichalcogenide," Nat. Nanotechnol., **9**(4), pp. 262–267.

[136] Pospischil, A., Furchi, M. M., and Mueller, T., 2014, "Solar-energy conversion and light emission in an atomic monolayer p–n diode," Nat. Nanotechnol., **9**(4), pp. 257–261.

[137] Groenendijk, D. J., Buscema, M., Steele, G. A., Michaelis de Vasconcellos, S., Bratschitsch, R., van der Zant, H. S. J., and Castellanos-Gomez, A., 2014, "Photovoltaic and Photothermoelectric Effect in a Double-Gated WSe_2 Device," Nano Lett., **14**(10), pp. 5846–5852.

[138] Suh, J., Park, T., Lin, D.-Y., Fu, D., Park, J., Jung, H. J., Chen, Y., Ko, C., Jang, C., Sun, Y., Sinclair, R., Chang, J., Tongay, S., and Wu, J., 2014, "Doping against the Native Propensity of MoS_2 : Degenerate Hole Doping by Cation Substitution," Nano Lett., **14**(12), pp. 6976–6982.

[139] Wang, S. Y., Ko, T. S., Huang, C. C., Lin, D. Y., and Huang, Y. S., 2014, "Optical and electrical properties of MoS_2 and Fe-doped MoS_2," Jpn. J. Appl. Phys., **53**(4S), p. 04EH07.

[140] Bernardi, M., Palummo, M., and Grossman, J. C., 2013, "Extraordinary Sunlight Absorption and One Nanometer Thick Photovoltaics Using Two-Dimensional Monolayer Materials," Nano Lett., **13**(8), pp. 3664–3670.

[141] Furchi, M. M., Polyushkin, D. K., Pospischil, A., and Mueller, T., 2014, "Mechanisms of Photoconductivity in Atomically Thin MoS_2," Nano Lett., **14**(11), pp. 6165–6170.

[142] Sim, S., Park, J., Song, J., In, C., Lee, Y., Kim, H., and Choi, H., 2013, "Exciton dynamics in atomically thin MoS_2: Interexcitonic interaction and broadening kinetics," Phys. Rev. B, **88**(7), p. 75434.

[143] Lopez-Sanchez, O., Lembke, D., Kayci, M., Radenovic, A., and Kis, A., 2013, "Ultrasensitive photodetectors based on monolayer MoS_2," Nat. Nanotechnol., **8**(7), pp. 497–501.

[144] Kufer, D., and Konstantatos, G., 2015, "Highly Sensitive, Encapsulated MoS_2 Photodetector with Gate Controllable Gain and Speed," Nano Lett., **15**(11), pp. 7307–7313.

[145] Sze, S. M., 1981, Physics of Semiconductor Devices, John Wiley & Sons.

[146] Schenk, A., and Krumbein, U., 1995, "Coupled defect-level recombination: Theory and application to anomalous diode characteristics," J. Appl. Phys., **78**(5), p. 3185.

[147] Breitenstein, O., Bauer, J., Lotnyk, A., and Wagner, J.-M., 2009, "Defect induced non-ideal dark – characteristics of solar cells," Superlattices Microstruct., **45**(4–5), pp. 182–189.

[148] Hegedus, S., Desai, D., and Thompson, C., 2007, "Voltage dependent photocurrent collection in CdTe/CdS solar cells," Prog. Photovoltaics Res. Appl., **15**(7), pp. 587–602.

[149] Mueller, T., Xia, F., and Avouris, P., 2010, "Graphene photodetectors for high-speed optical communications," Nat. Photonics, **4**(5), pp. 297–301.

[150] Xia, F., Mueller, T., Lin, Y.-M., Valdes-Garcia, A., and Avouris, P., 2009, "Ultrafast graphene photodetector.," Nat. Nanotechnol., **4**(12), pp. 839–43.

[151] Castellanos-Gomez, A., 2015, "Black Phosphorus: Narrow Gap, Wide Applications.," J. Phys. Chem. Lett., **6**(21), pp. 4280–91.

[152] Jin, W., Yeh, P. C., Zaki, N., Zhang, D., Sadowski, J. T., Al-Mahboob, A., Van Der Zande, A. M., Chenet, D. A., Dadap, J. I., Herman, I. P., Sutter, P., Hone, J., and Osgood, R. M., 2013, "Direct measurement of the thickness-dependent electronic band structure of MoS_2 using angle-resolved photoemission spectroscopy," Phys. Rev. Lett., **111**(10), p. 106801.

[153] Zólyomi, V., Drummond, N. D., and Fal'ko, V. I., 2014, "Electrons and phonons in single layers of hexagonal indium chalcogenides from ab initio calculations," Phys. Rev. B, **89**(20), p. 205416.

[154] Ruppert, C., Aslan, O. B., and Heinz, T. F., 2014, "Optical properties and band gap of single- and few-layer $MoTe_2$ crystals," Nano Lett., **14**(11), pp. 6231–6236.

[155] He, K., Poole, C., Mak, K. F., and Shan, J., 2013, "Experimental demonstration of continuous electronic structure tuning via strain in atomically thin MoS_2," Nano Lett., **13**(6), pp. 2931–6.

[156] Castellanos-Gomez, A., Roldán, R., Cappelluti, E., Buscema, M., Guinea, F., van der Zant, H. S. J., and Steele, G. A., 2013, "Local strain engineering in atomically thin MoS_2," Nano Lett., **13**(11), pp. 5361–6.

[157] Tamalampudi, S. R., Lu, Y., Kumar U, R., Sankar, R., Liao, C.-D., Moorthy B, K., Cheng, C., Chou, F. C., and Chen, Y., 2014, "High performance and bendable few-layered InSe photodetectors with broad spectral response.," Nano Lett., **14**(5), pp. 2800–6.

[158] Lei, S., Wen, F., Li, B., Wang, Q., Huang, Y., Gong, Y., He, Y., Dong, P., Bellah, J., George, A., Ge, L., Lou, J., Halas, N. J., Vajtai, R., and Ajayan, P. M., 2015, "Optoelectronic Memory Using Two-Dimensional Materials," Nano Lett., **15**(1), pp. 259–265.

[159] Balakrishnan, N., Kudrynskyi, Z. R., Fay, M. W., Mudd, G. W., Svatek, S. A., Makarovsky, O., Kovalyuk, Z. D., Eaves, L., Beton, P. H., and Patanè, A., 2014, "Room Temperature Electroluminescence from Mechanically Formed van der Waals III-VI Homojunctions and Heterojunctions," Adv. Opt. Mater.

[160] Tomaino, J. L., Jameson, A. D., Kevek, J., Paul, M. J., van der Zande, A. M., Barton, R. A., McEuen, P. L., Minot, E. D., and Lee, Y.-S., 2012, "Terahertz imaging and time-domain spectroscopy of large-area graphene on silicon," p. 82600Z.

[161] Hannes, W.-R., Jonson, M., and Titov, M., 2011, "Electron-hole asymmetry in two-terminal graphene devices," Phys. Rev. B, **84**(4), p. 45414.

[162] Mudd, G. W., Svatek, S. a., Hague, L., Makarovsky, O., Kudrynskyi, Z. R., Mellor, C. J., Beton, P. H., Eaves, L., Novoselov, K. S., Kovalyuk, Z. D., Vdovin, E. E., Marsden, A. J., Wilson, N. R., and Patanè, A., 2015, "High Broad-Band Photoresponsivity of Mechanically Formed InSe-Graphene van der Waals Heterostructures," Adv. Mater., **27**(25), pp. 3760–3766.

[163] Ferrari, A. C., Bonaccorso, F., Fal'ko, V., Novoselov, K. S., Roche, S., Bøggild, P., Borini, S., Koppens, F. H. L., Palermo, V., Pugno, N., Garrido, J. A., Sordan, R., Bianco, A., Ballerini, L., Prato, M., Lidorikis, E., Kivioja, J., Marinelli, C., Ryhänen, T., Morpurgo, A., Coleman, J. N., Nicolosi, V., Colombo, L., Fert, A., Garcia-Hernandez, M., Bachtold, A., Schneider, G. F., Guinea, F., Dekker, C., Barbone, M., Sun, Z., Galiotis, C., Grigorenko, A. N., Konstantatos, G., Kis, A., Katsnelson, M., Vandersypen, L., Loiseau, A., Morandi, V., Neumaier, D., Treossi, E., Pellegrini, V., Polini, M., Tredicucci, A., Williams, G. M., Hee Hong, B., Ahn, J.-H., Min Kim, J., Zirath, H., van Wees, B. J., van der Zant, H., Occhipinti, L., Di Matteo, A., Kinloch, I. A., Seyller, T., Quesnel, E., Feng, X., Teo, K., Rupesinghe, N.,

Hakonen, P., Neil, S. R. T., Tannock, Q., Löfwander, T., and Kinaret, J., 2015, "Science and technology roadmap for graphene, related two-dimensional crystals, and hybrid systems," Nanoscale, **7**(11), pp. 4598–4810.

[164] Millot, M., Broto, J.-M., George, S., González, J., and Segura, A., 2010, "Electronic structure of indium selenide probed by magnetoabsorption spectroscopy under high pressure," Phys. Rev. B, **81**(20), p. 205211.

[165] Camassel, J., Merle, P., Mathieu, H., and Chevy, A., 1978, "Excitonic absorption edge of indium selenide," Phys. Rev. B, **17**(12), pp. 4718–4725.

[166] Manjo, F. J., Mun, V., Segura, A., Bouvier, J., and Andre, M. V, 1997, "Strong optical nonlinearities in gallium and indium selenides related to inter-valence-band transitions induced by light pulses," **56**(7).

[167] Georgiou, T., Jalil, R., Belle, B. D., Britnell, L., Gorbachev, R. V, Morozov, S. V, Kim, Y.-J., Gholinia, A., Haigh, S. J., Makarovsky, O., Eaves, L., Ponomarenko, L. a, Geim, A. K., Novoselov, K. S., and Mishchenko, A., 2013, "Vertical field-effect transistor based on graphene-WS_2 heterostructures for flexible and transparent electronics.," Nat. Nanotechnol., **8**(2), pp. 100–3.

[168] Chen, Z., Biscaras, J., and Shukla, A., 2015, "A high performance graphene/few-layer InSe photo-detector.," Nanoscale, **7**(14), pp. 5981–6.

[169] Luo, W., Cao, Y., Hu, P., Cai, K., Feng, Q., Yan, F., Yan, T., Zhang, X., and Wang, K., 2015, "Gate Tuning of High-Performance InSe-Based Photodetectors Using Graphene Electrodes," Adv. Opt. Mater., **3**(10), pp. 1418–1423.

[170] Huang, W., Gan, L., Li, H., Ma, Y., and Zhai, T., 2016, "2D layered group IIIA metal chalcogenides: synthesis, properties and applications in electronics and optoelectronics," CrystEngComm.

[171] Zhang, W., Chuu, C.-P., Huang, J.-K., Chen, C.-H., Tsai, M.-L., Chang, Y.-H., Liang, C.-T., Chen, Y.-Z., Chueh, Y.-L., He, J.-H., Chou, M.-Y., and Li, L.-J., 2014, "Ultrahigh-gain photodetectors based on atomically thin graphene-MoS_2 heterostructures.," Sci. Rep., **4**, p. 3826.

[172] Lee, G.-H., Yu, Y.-J., Cui, X., Petrone, N., Lee, C.-H., Choi, M. S., Lee, D.-Y., Lee, C., Yoo, W. J., Watanabe, K., Taniguchi, T., Nuckolls, C., Kim, P., and Hone, J., 2013, "Flexible and transparent MoS_2 field-effect transistors on hexagonal boron nitride-graphene heterostructures.," ACS Nano, **7**(9), pp. 7931–6.

[173] Hu, P., Wang, L., Yoon, M., Zhang, J., Feng, W., Wang, X., Wen, Z., Idrobo, J. C., Miyamoto, Y., Geohegan, D. B., and Xiao, K., 2013, "Highly responsive ultrathin GaS nanosheet photodetectors on rigid and flexible substrates.," Nano Lett., **13**(4), pp. 1649–54.

[174] Hu, P., Wen, Z., Wang, L., Tan, P., and Xiao, K., 2012, "Synthesis of few-layer

GaSe nanosheets for high performance photodetectors.," ACS Nano, **6**(7), pp. 5988–94.

[175] Youngblood, N., Chen, C., Koester, S. J., and Li, M., 2015, "Waveguide-integrated black phosphorus photodetector with high responsivity and low dark current," Nat. Photonics, **9**, pp. 247–252.

[176] Zhang, W., Huang, J.-K., Chen, C.-H., Chang, Y.-H., Cheng, Y.-J., and Li, L.-J., 2013, "High-Gain Phototransistors Based on a CVD MoS_2 Monolayer," Adv. Mater., **25**(25), pp. 3456–3461.

[177] Island, J. O., Buscema, M., Barawi, M., Clamagirand, J. M., Ares, J. R., Sánchez, C., Ferrer, I. J., Steele, G. A., van der Zant, H. S. J., and Castellanos-Gomez, A., 2014, "Ultrahigh Photoresponse of Few-Layer TiS_3 Nanoribbon Transistors," Adv. Opt. Mater., **2**(7), pp. 641–645.

[178] Buscema, M., Island, J. O., Groenendijk, D. J., Blanter, S. I., Steele, G. A., van der Zant, H. S. J., and Castellanos-Gomez, A., 2015, "Photocurrent generation with two-dimensional van der Waals semiconductors.," Chem. Soc. Rev., **44**(11), pp. 3691–718.

[179] Konstantatos, G., Badioli, M., Gaudreau, L., Osmond, J., Bernechea, M., Arquer, F. P. G. De, Gatti, F., and Koppens, F. H. L., 2012, "Hybrid graphene – quantum dot phototransistors with ultrahigh gain," **7**(June).

[180] Dufferwiel, S., Fras, F., Trichet, A., Walker, P. M., Li, F., Giriunas, L., Makhonin, M. N., Wilson, L. R., Smith, J. M., Clarke, E., Skolnick, M. S., and Krizhanovskii, D. N., 2014, "Strong exciton-photon coupling in open semiconductor microcavities," Appl. Phys. Lett., **104**(19), p. 192107.

[181] Konstantatos, G., Badioli, M., Gaudreau, L., Osmond, J., Bernechea, M., Garcia de Arquer, F. P., Gatti, F., and Koppens, F. H. L., 2012, "Hybrid graphene-quantum dot phototransistors with ultrahigh gain.," Nat. Nanotechnol., **7**(6), pp. 363–8.

List of publications

Two Vernier-templated routes to a 24-porphyrin nanoring.

Dmitry V. Kondratuk, Luis M. A. Perdigao, Melanie C. O'Sullivan, **Simon A. Svatek**, Gareth Smith, James N. O'Shea, Peter H. Beton, Harry L. Anderson

Angewandte Chemie International Edition 51, 6696–9 (2012).

Mechanical stiffening of porphyrin nanorings through supramolecular columnar stacking.

Simon A. Svatek, Luis M. A. Perdigão, Andrew Stannard, Maria B. Wieland, Dmitry V. Kondratuk, Harry L. Anderson, James N. O'Shea, and Peter H. Beton

Nano Letters 13, 3391–5 (2013).

Tuning the Bandgap of Exfoliated InSe Nanosheets by Quantum Confinement.

Garry W. Mudd, **Simon A. Svatek**, Tianhang Ren, Amalia Patanè, Oleg Makarovsky, Laurence Eaves, Peter H. Beton, Zakhar D. Kovalyuk, George V. Lashkarev, Zakhar R. Kudrynskyi, Alexandr I. Dmitriev

Advanced Materials. 25, 5714–8 (2013).

Bimolecular porous supramolecular networks deposited from solution on layered materials: graphite, boron nitride and molybdenum disulphide.

Vladimir V. Korolkov, **Simon A. Svatek**, Stephanie Allen, Clive J. Roberts, Saul J. B. Tendler, Takashi Taniguchi, Kenji Watanabe, Neil R. Champness, Peter H. Beton

Chemical Communications. 50, 8882-8885 (2014).

Room temperature electroluminescence from mechanically-formed van der Waals III-VI homojunctions and heterojunctions.

Nilanthy Balakrishnan, Zakhar R. Kudrynskyi, Michael W. Fay, Garry W. Mudd, **Simon A. Svatek**, Oleg Makarovsky, Zakhar D. Kovalyuk, Laurence Eaves, Peter H. Beton, Amalia Patanè

Advanced Optical Materials. 2 (11), 1064-1069 (2014)

Adsorbate-induced curvature and stiffening of graphene.

Simon A Svatek, Oliver R Scott, Jasmine PH Rivett, Katherine Wright, Matteo Baldoni, Elena Bichoutskaia, Takashi Taniguchi, Kenji Watanabe, Alexander J Marsden, Neil R Wilson, Peter H Beton

Nano letters. 15 (1), 159-164 (2014)

Graphene-InSe-graphene van der Waals heterostructures

Simon A Svatek, Garry W Mudd, Zakhar R Kudrynskyi, Oleg Makarovsky, Zakhar D Kovalyuk, Christopher J Mellor, Laurence Eaves, Peter H Beton, Amalia Patanè

Journal of Physics: Conference Series 647 (1), 012001 (2015)

High Broad-Band Photoresponsivity of Mechanically Formed InSe–Graphene van der Waals Heterostructures

Garry W Mudd, **Simon A Svatek**, Lee Hague, Oleg Makarovsky, Zakhar R Kudrynskyi, Christopher J Mellor, Peter H Beton, Laurence Eaves, Kostya S Novoselov, Zakhar D Kovalyuk, Evgeny E Vdovin, Alex J Marsden, Neil R Wilson, Amalia Patanè

Advanced Materials. 27 (25), 3760-3766 (2015)

Ligand-Induced Control of Photoconductive Gain and Doping in a Hybrid Graphene–Quantum Dot Transistor

Lyudmila Turyanska, Oleg Makarovsky, **Simon A Svatek**, Peter H Beton, Christopher J Mellor, Amalia Patanè, Laurence Eaves, Neil R Thomas, Michael W Fay, Alexander J Marsden, Neil R Wilson

Advanced Electronic Materials. 1 (7) (2015)

van der Waals-Induced Chromatic Shifts in Hydrogen-Bonded Two-Dimensional Porphyrin Arrays on Boron Nitride

Vladimir V Korolkov, **Simon A Svatek**, Alex Summerfield, James Kerfoot, Lixu Yang, Takashi Taniguchi, Kenji Watanabe, Neil R Champness, Nicholas A Besley, Peter H Beton

ACS nano 9 (10), 10347-10355 (2015)

Highly responsive UV-photodetectors based on single electrospun TiO_2 nanofibres

Aday J Molina-Mendoza, Alicia Moya, Riccardo Frisenda, **Simon A Svatek**, Patricia Gant, Sergio Gonzalez-Abad, Elisa Antolin, Nicolás Agraït, Gabino Rubio-Bollinger, David Perez de Lara, Juan J Vilatela, Andres Castellanos-Gomez

Journal of Materials Chemistry C (4), 10707-10714 (2016)

Lithography-free electrical transport measurements on 2D materials by direct microprobing

Patricia Gant, Yue Niu, **Simon A Svatek**, Nicolas Agrait, Carmen Munuera, Mar García-Hernández, Riccardo Frisenda, David Perez de Lara, Andres Castellanos-Gomez

Journal of Materials Chemistry C, Advance Article (2017)

Gate tunable photovoltaic effect in MoS_2 vertical p–n homostructures

Simon A Svatek, Elisa Antolin, Der-Yuh Lin, Riccardo Frisenda, Christoph Reuter, Aday J Molina-Mendoza, Manuel Muñoz, Nicolás Agraït, Tsung-Shine Ko, David Perez de Lara, Andres Castellanos-Gomez

Journal of Materials Chemistry C (5), 854-861 (2017)

Photodiodes based in $La_{0.7}Sr_{0.3}MnO_3$/single layer MoS_2 hybrid vertical heterostructures

Yue Niu, Riccardo Frisenda, **Simon A. Svatek**, Gloria Orfila, Fernando Gallego, Patricia Gant, Nicolás Agraït, Carlos León, Alberto Rivera-Calzada, David Perez De Lara, Jacobo Santamaría, Andres Castellanos-Gomez

2D Mater., 4 (3), 34002 (2017)

Large quantum thermopower in MoS_2

Simon A Svatek, Hatef Sadeghi, Sara Sangtarash, Laura Rincón-García, Riccardo Frisenda, Patricia Gant, David Pérez de Lara, Gabino Rubio-Bollinger, Andres Castellanos-Gomez, Colin J Lambert, Nicolás Agraït

In peer-review (2017).

Enhanced thermoelectricity in graphene-fullerene composite materials

Simon A. Svatek, Valentina Sacchetti, Laura Rincón-García, Gabino Rubio-Bollinger, Colin J Lambert, Nazario Martín, Nicolás Agraït

In preparation.